MODULATION-ASSISTED MACHINING OF COMPACTED GRAPHITE IRON WITH COATED CARBIDE TOOLS

By

Juan Jose Sandoval Lavieri

A DISSERTATION

Submitted to
Michigan State University
in partial fulfillment of the requirements
for the degree of

Mechanical Engineering – Doctor of Philosophy

2022

ABSTRACT

Compact graphite iron (CGI) is a promising material that could replace conventional gray cast iron for making diesel engine blocks and heads to increase fuel economy and reduce emissions. However, the poor machinability of CGI evidenced by rapid tool wear leads to significantly increased manufacturing cost. To improve the machinability, a novel machining technique, modulation-assisted machining (MAM), is employed to provide low-frequency (tens or hundreds of Hz) modulation on the tool feed motion. This study intends to explore the feasibility and understand the effects of MAM in improving the machinability of CGI with coated carbide cutting tools.

First, tool wear performance was compared between conventional machining (CM) and MAM using a dry turning configuration for a range of cutting speeds (150, 250 and 350 m/min) while measuring cutting forces and tool temperature. The results show that MAM can significantly increase tool life up to several folds especially at higher cutting speeds (250 and 350 m/min) compared to CM. It was found the cutting force and tool temperature are strongly influenced by the tool wear and the extent of iron adhesion.

Next, tool wear was characterized in detail using high-resolution digital microscopy, SEM and EDS techniques for CM and MAM turning at 250 m/min in both dry and lubricated conditions. Significant wear reductions with MAM were achieved compared to CM in both dry and lubricated conditions. However, MAM dry turning resulted in significant reduction of tool wear compared to MAM lubricated turning. It was found that two wear phenomena account for the wear reduction in MAM: 1) the formation of SiO_2 deposition layer on tool flank and 2) the preservation of the coatings on the cutting edge. The mechanisms on how the wear progression is slowed down by the observed wear phenomena as well as how these phenomena are enabled by MAM are discussed.

Finally, the effects of modulation frequency on the tool wear and cutting temperature were investigated. Tool wear and cutting temperature were characterized for a range of modulation frequency and the ratio between modulation and rotation frequencies (1.5 – 9.5) in MAM turning at 350 m/min. It was found that higher modulation frequency leads to lower crater wear but higher nose wear. The main flank wear however seems to mainly depend on the formation of SiO_2 deposition layer. There is an optimal frequency ratio due to the conflicting impacts on the crater wear and nose wear, which is also supported by the result that the lowest tool temperature is achieved at an intermediate frequency ratio.

ACKNOWLEDGEMENTS

I would like to thank all the people that made this work possible in a structured way. My advisors, Dr Patrick Kwon (for your great ideas and your guidance, facilitating the engineering), Dr Yang Guo (for your persistence and always useful advice, facilitating the science). My other committee members: Dr Firas Khasawneh (for your very useful vibrations class, and help with the understanding of sensors), and Dr Thomas Bieler (for your mind opening physical metallurgy class and help with the understanding of metals). Other department professors for always being available for great discussions: Dr Katy Colbry, Dr Haseung Chung, Dr Himanshu Saharasbudhe, Dr Lik Chuan Lee, Dr Daniel Segalman, and Dr Brian Feeny. Instructors Mike Koschmider and Roy Bailiff (for going beyond duty to help us make science). Staff at the microscopy center: Dr Melinda Frame (for your great mastery and guidance with the confocal microscope), Dr Stanley Flegler, Amy Albin and Abby Vanderberg (for always going the extra mile to help with the SEM). Fellow lab members: Dinh Nguyen, Sirisak ToopTong, Ryan Khwarizmi, Jisheng Chen, Aaquib Ali, Hoa Nguyen, Bibek Poudel, Jack Song, Tyler Bauder, Swen Hawke, Beytullah Aydogan, Aaron Onneil Mellh Yesilli and Guillermo Huanes (for being smart, supportive, and good friends in times of need). My friends out of the lab: Angie Bustos, Felix Enciso, Paola Puggioni, Tatiana Garcia, Aimer Gutierrez, Andres Herrera, Leidy Vanegas, Jose Regal, Omar Pozos, Luis Rodriguez, Andres Galindo, Marcela Tabares, Francisco Dillon, Noelia Pastor, Zach Neithercut and many others that I cannot thank enough for your support and help. My family: my brother Juan Carlos, my father Juan Carlos, my grandfather Elio, and my grandmother Olga (for sacrificing so much being afar while I studied) and most importantly my beloved mother Janeth Lavieri, who left me before I could finish what she helped me start, but whose inspiration will never be forgotten.

TABLE OF CONTENTS

LIST OF TABLES

LIST OF FIGURES

INTRODUCTION

Cast irons are classified according to the graphite shape in their microstructure. The most common type of iron is Flake graphite iron or FGI in which the graphite takes a flake-like shape with sharp edges. Another type of iron denominated nodular graphite iron or NGI has graphite in nodular shape which makes it more resistant to fracture than FGI but extremely difficult to machine. Compacted graphite iron or CGI is a type of iron where the graphite takes a compact vermicular shape which gives it a good balance of mechanical properties between FGI and NGI. CGI has less brittleness than FGI, while having better machinability, damping capabilities and thermal conductivity than NGI. This makes CGI a very promising material for the making of diesel engine blocks, allowing them to operate at higher pressure and temperature while being lighter than FGI components for the same mechanical resistance, reducing fuel consumption.

However, the machinability of CGI is much poorer than FGI. Whereas in industry usually FGI is machined at speeds of 1000m/min, CGI is usually machined at speeds of 150 m/min. In continuous cutting operations like turning or boring, the tool life reduction when machining CGI vs FGI is even more severe than for interrupted cutting operations like milling.

The failure of cutting tools is controlled by the type of tool wear that is dominant for a certain condition. The main tool wear mechanisms are: abrasion, adhesion, solution, diffusion and surface damage. The dominant wear mode will depend on the cutting temperature and therefore the cutting speed. To machine iron at high speeds, cubic boron nitride tools (CBN) which are very hard and resistant to solution and diffusion wear are used. At these speeds, the machinability of FGI surpasses that of CGI substantially, which is why CBN is used to machine FGI at such high speeds. The reason for the poor machinability of CGI at high speed is believed to be the formation of a protective MnS layer on the tool when machining FGI which is absent in CGI. However, more recent studies have shown that it is the formation of a protective alumina layer that increases the machinability of FGI vs CGI. The reason for this is that alumina is the most resistant material to dissolution in iron, second only to zirconia.

When machining CGI at low speeds, coated carbides are usually used despite having lower wear resistance than cBNs because they are more cost-effective. At speeds below 200 m/min, the machinability of CGI is slightly worse than FGI. However, for speeds above 200 m/min, the solubility and adhesion on the tool become dominant and they are affected by the more severe plastic deformation of the chip in CGI. Therefore, coated tools are better than plain carbides for CGI machining, but CGI machinability is still very poor compared to FGI.

Some researchers have suggested pure alumina tools for iron machining due to their strong resistance to solution wear. However, in interrupted cutting such as milling, wear modes such as surface damage are more dominant. Therefore, ceramic alumina tools which are good for continuous cutting are not recommended due to their poor toughness. In this case, coated carbides or ceramic silicon nitride tools are used.

Certain experiments suggest that interrupted cutting in iron produces less wear than continuous cutting, given that the wear modes are different than continuous cutting. However, not all experiments have been capable of wear reduction due to an incapability to control the cutting interruptions. Given that temperature triggers the most severe wear modes, most methods for machinability improvement focus on reducing the cutting temperature. For example, lubricants intend to alleviate the severe tribological condition at the cutting interface, as well as taking away the heat from the cutting zone. Certain promising applications such as minimum quantity lubrication focus on reducing the loads on the cutting zone without the need for cooling the tool, whereas cryogenic cooling focuses only on reducing the cutting temperature. However, these applications have sometimes limited effects due to the inability to properly reach the cutting zone.

Other approaches intend to change the load that the chip imposes on the tool. Laser assisted machining for example, increases the temperature to decrease the yield strength of the material in order to reduce the cutting forces on the tool. However, the high laser power required is a limitation for cutting of certain materials. Another technique known as vibration-assisted machining applies vibrations in order to reduce the tribological condition on the tool-chip interface. When the used frequency is above the frequency of sound, the technique is known as ultrasonic vibration assisted machining. It is found that the interruption of the cutting process in this technique can improve the tool life for certain ferrous materials, allowing the formation of protective oxides in the contact zone due to the periodic disengagement. However, the cutting temperature is not reduced which limits the wear reduction capabilities in this technique, and a completely interrupted and controlled cutting process is the best option to reduce tool wear.

Finally, modulation-assisted machining or MAM applies a low-frequency and high amplitude vibration which can periodically disengage the tool from the cut in a controlled manner. The disengagement time is therefore more significant than for ultrasonic vibration-assisted machining, making the temperature reduction and lubricant action more significant. Different applications of MAM such as in drilling and turning have already been developed with success for difficult to cut materials. Several machining parameters such as chip evacuation wear and surface roughness have been substantially improved. In fact, other researchers have found that for CGI turning, the tool life can be increased in one order of magnitude as compared to conventional machining techniques. However, to date, there is no study that confirms if MAM is capable of improving the machinability of CGI with the more readily available coated carbide tools. Even more, there is no complete explanation of the mechanism that makes MAM improve CGI machinability in such a significant way or if this improvement can be controlled at all. Therefore, this study intends to answer the following questions:

1. Can Modulation-Assisted Machining improve the machinability of CGI with coated carbide tools in a significant way?
2. What is the mechanism that regulates the improvement of tool life when machining CGI with coated carbides using Modulation-Assisted Machining?
3. Which variables can be changed to optimize the tool life in Modulation-Assisted Machining of CGI?

The chapters in this dissertation are organized in the following structure in order to provide answer to the stated research questions in the context of the current state of the art. Chapter 1 presents a background review that shows the state of the art in CGI machining, including a general description of the machinability problem, which is affected by the CGI structure-properties-processing relationships and the current techniques for tool life improvement based on such relationships. The machinability is studied in two categories depending on cutting speed: high and low speed machinability of CGI. Developments addressing these wear conditions are also grouped in two categories: the development of new tool materials and the implementation of novel cutting techniques. The tool material development to machine CGI relies on the chemical composition of the tool to make it more resistant to chemical wear at high speeds, and mechanical and adhesion wear at low to moderate speeds. On the other hand, the novel cutting techniques rely on the reduction of the severe cutting conditions found in the tool-chip contact zone which are responsible for tool wear. The classification of MAM within these techniques is also described, and the main research questions of this dissertation are stated in terms of the work previously done by others.

In Chapter 2, the effect of MAM in the case of CGI dry turning with coated carbide tools at different cutting speeds is described. Tool wear, forces, and tool temperature are recorded and characterized for both conventional machining and MAM turning at three speeds: 150m/min, 250m/min and 350m/min. The results show wear reduction by MAM is not significant at low cutting speed (150m/min), but it is quite remarkable at higher cutting speeds (250m/min and 350m/min). the force and temperature results are well correlated with the wear results, with a strong interdependence of the forces and temperatures on the tool wear and adhesion. This study demonstrates how MAM can improve the machinability of CGI with coated carbides, and the results help to understand the wear mechanism when cutting CGI with coated carbide tools.

In Chapter 3, the focus is in understanding the mechanisms behind the machinability improvement of turning CGI under MAM with coated carbide tools. The evolution of the wear is thoroughly characterized in conventional machining and MAM in both the dry and lubricated conditions at 250m/min. It is shown that MAM can significantly reduce the wear as compared to CM machining in all cases. Surprisingly, MAM dry turning decreases tool wear even more than MAM lubricated. The reason for this behavior is the formation of SiO_2 deposition layer on the tool flank and a preservation of the coating in the cutting edge, with both mechanisms being present in MAM dry turning but only the coating preservation on lubricated MAM turning. The mechanism in which these phenomena reduce the wear, as well as how MAM originates these phenomena are discussed.

In Chapter 4, the effect of the ratio between the modulation frequency and the workpiece rotating frequency is described. Three different ratios are used: 3.5x (low), 6.5x (medium) and 9.5x (high). The frequency ratio significantly affects the crater wear, but not the flank wear. The flank wear is significantly improved with respect to conventional machining regardless of the ratio.

The crater wear decreases when the frequency ratio is increased, indicating a reduction of the rake temperature. The overall tool temperature is also influenced by the frequency ratio. However, a higher MAM frequency ratio increases the nose wear due to the constant rubbing effect against the workpiece during the cut. This leads to a non-uniform variation of the overall temperature, with the temperature for 3.5x and 9.5x being higher than for 6.5x. Even at extremely low frequency ratio of 1.5x, the flank wear improvement mechanisms described in previous chapters are present, signaling the independence of such mechanisms from the crater temperature and the frequency ratio. In conclusion, the frequency ratio can be adjusted to an optimal value which generates the lowest temperature and the best balance between crater and nose wear while always reducing flank wear in MAM.

CHAPTER 1: BACKGROUND

1.1 Structures, properties, and applications of cast irons

Cast irons can be classified in three categories according to the morphology of the graphite phase in the microstructure (Figure 1). Flake graphite iron (FGI) is the most commonly used type of iron. The FGI microstructure consists of thin graphite flakes with smooth surfaces and sharp edges. In another type of iron, Nodular Graphite Iron or NGI, the graphite agglomerations are spherical, which makes cracks very difficult to propagate, but this makes the material very ductile in a similar way to pure iron. As a mid-point between FGI and NGI is another type of iron known as Compacted Graphite Iron (CGI) which has a similar microstructure to that of FGI, but the graphite has a vermicular or worm-like shape with round edges and a bumpy rougher surface than that of FGI. Thus, the matrix and the inclusions have better integration making cracks more difficult to propagate than FGI.

The mechanical properties of the three types of iron are shown in table [1]. In FGI, the shape of the graphite inclusions gives superior damping capabilities and provides superior heat conductivity and stiffness. FGI is especially useful in components requiring high stiffness and damping while dissipating heat such as machine beds, bearings, gears and housings. However, the graphite flakes also interrupt the matrix extensively, promoting stress peaks in the graphite flake edges and making FGI brittle[2]. On the other hand, NGI components have less damping capabilities, have lower thermal conductivity and are more difficult to machine than FGI components. Many manufacturers step away from NGI because it is unsuitable for efficiently machining lightweight, strong components. CGI has a tensile strength and fatigue strength that is roughly twice that of FGI, the elastic modulus is 35% higher, and thermal conductivity is 25% lower than FGI. At the same time, CGI is not as ductile as NGI, making it more rigid than NGI and facilitating production of lightweight components[3–5]. The features mentioned above make CGI more suitable for the fabrication of diesel engine blocks, allowing them to operate at higher cylinder pressures and temperatures while requiring less weight than FGI components, resulting in better fuel economies and reduced emissions[6,7].

Table 1: Mechanical properties of FGI, CGI and NGI. Adapted from [1].

Property	FGI	CGI	NGI
Tensile strength (MPa)	250	450	750
Elastic Modulus (GPa)	105	145	160
Elongation (%)	0	1.5	5
Thermal conductivity (W/mK)	48	37	28
Relative damping capacity (FGI=1)	1	.35	.22

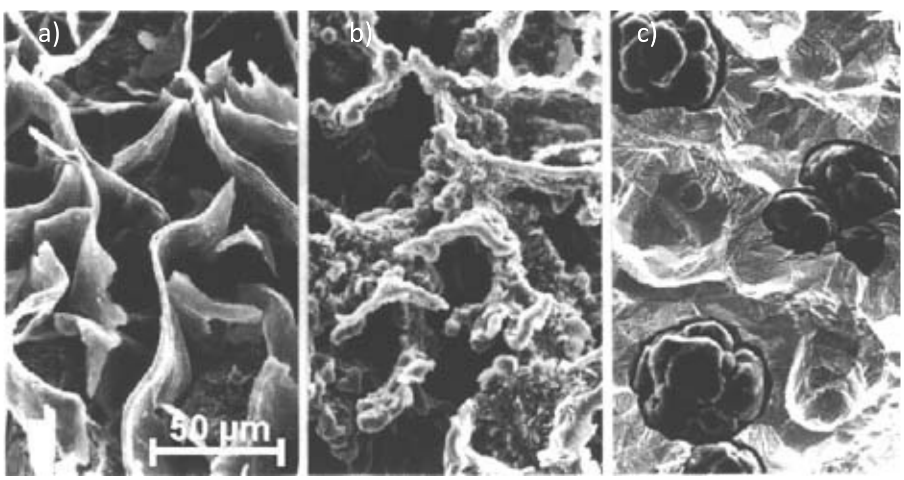

Figure 1: The microstructures of three types of Cast Iron: a) Flake Graphite Iron (FGI), b) Compacted Graphite Iron (CGI), and c) Nodular Graphite Iron (NGI). Adapted from [4].

1.2 Machinability of Cast Irons

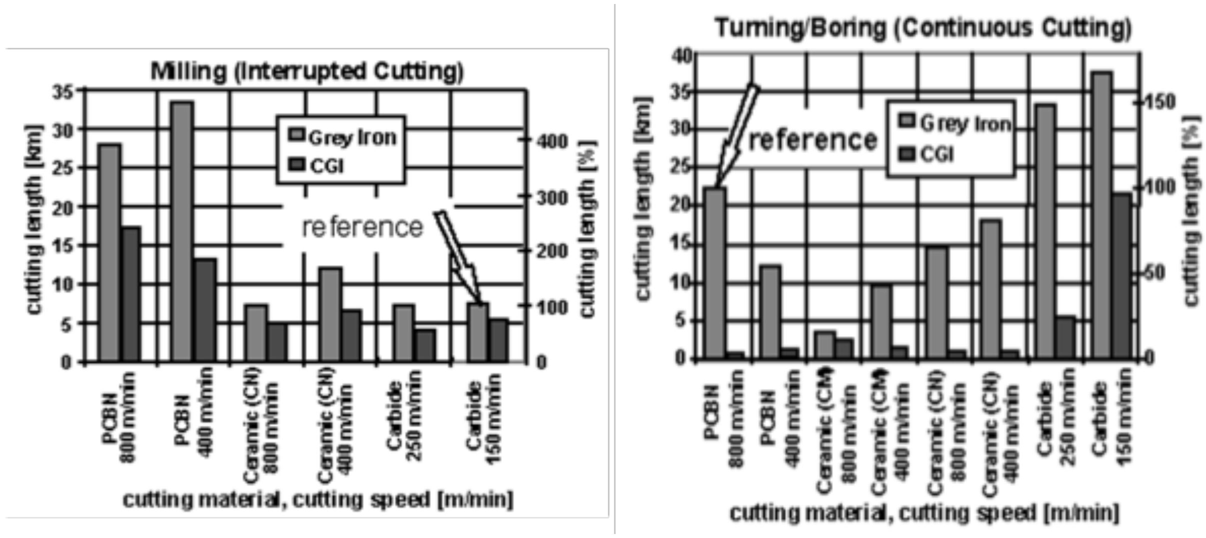

Figure 2: Comparative tool life for different tool materials in interrupted (milling) and continuous (turning/boring) cutting of 70-80% pearlitic CGI and Grey Iron (FGI). Adapted from [8].

One major problem in making CGI components is the machinability of CGI compared to FGI. FGI is usually machined at speeds much higher than CGI. In Figure 2, the tool life of several tool materials when machining FGI and CGI is compared. In general, the machinability of CGI is very low compared to FGI. In interrupted cutting, the life is reduced by 50% at high speeds and up to 50% at low speeds. In continuous cutting operations like turning and boring, tool life is more severely affected, with a reduction of roughly 90% at high speeds and up to 80% at low speeds[4,8].

In this study, we divide the machinability of CGI in two regimes, low speed as less than 400 m/min and high speed as more than 400 m/min (this classification is given by Dawson [9], which is based on the type of tool used for each range of speeds).

1.3 Tool wear mechanisms

To understand the wear of cast irons, it is necessary to review the major wear mechanisms and their sources. The main tool wear mechanisms are abrasion, adhesion, solution, diffusion, and surface damage. In general, which wear mechanisms is dominant will depend on the cutting temperature and therefore the cutting speed range that is being analyzed. Abrasion occurs when a hard particle of the work material penetrates the tool material and make tangential motion creating micro cuts and grooves in the tool material. Adhesion is when the work material bonds to the tool material and shears off constantly in a tangential direction during cutting. Adhesion can be caused by chemical interaction as well as mechanical interaction, and it is usually caused by high friction coefficients, low to moderate temperatures and severe plastic deformation of the chip [10–12].

Tribooxidation implies chemical reactions occurring in the tool-chip contact area. The products of reaction can stay on the tool surface or be removed by the chip and they can be both beneficial or detrimental to the tool life. Among these chemical reactions, the term “solution wear” is the dissolution reaction of the tool material in the presence of the work material at a sufficiently high temperature. Tool materials with low solubility in the work material are expected to exhibit less wear than those with high solubility[13]. Diffusion, which happens after dissolution is the motion of atoms of the tool into the chip or vice versa, and just like solution wear, it increases with temperature[14]. Finally, surface damage is caused by force oscillations on the tool, which lead to fatigue, cracking and delamination. Surface damage is then caused by materials which show large force oscillations due to factors such as chip segmentation and is also present in interrupted cutting. Surface damage tends to occur suddenly after a certain time of no apparent wear, whereas abrasion tends to occur in a more progressive way [2].

The wear mechanisms mentioned in previous paragraphs generate specific types of wear depending on the location of the cutting tool where they occur. In Figure 3, the different forms of wear by tool location are identified. The work material engagement with the tool is more significant in the main cutting edge while the chip flows on the rake side and the new workpiece surface is on the flank side. The main wear modes for continuous cutting are usually crater and flank wear. The high tool temperatures in the rake side are usually the cause of crater wear, whereas the abrasion of the new generated workpiece surface is responsible for flank wear [15].

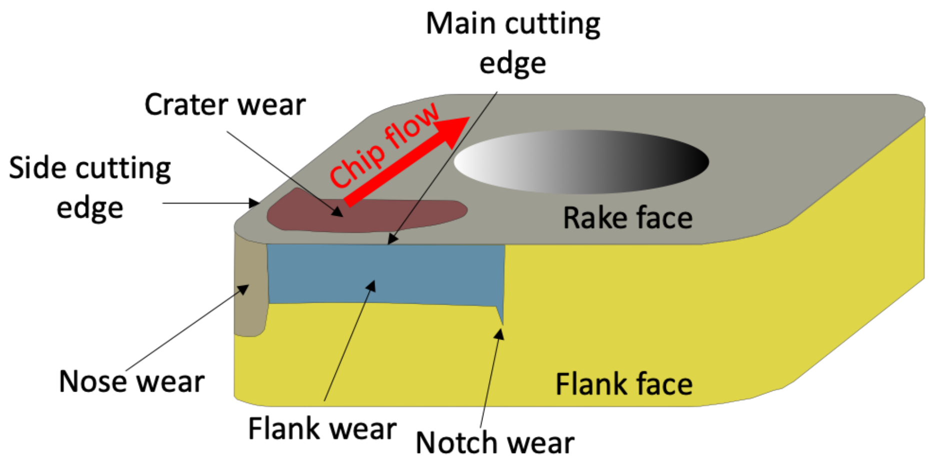

Figure 3: Wear modes and their location on cutting tool. The main modes are flank wear which is generated by abrasion and crater wear originated by high tool temperatures.

1.4 High speed cutting of cast iron with CBN tools

At high speeds the cutting temperatures and forces are extremely high and for that reason only cubic boron nitride (CBN) tools can used when machining any cast iron. The reason is that CBN is the hardest material known after diamond, but diamond tools have very high solution and diffusion wear in iron making them unsuitable for machining at high temperatures. In general, the machinability of FGI is very good at high speeds when compared to CGI and NGI [4] (Figure 4).

Therefore, FGI is machined with CBN tools at speeds even greater than 800 m/min. CGI on the other hand, exhibits a very poor machinability at high speeds when compared to FGI. Given that at high speeds the main wear mechanisms are solution, diffusion and adhesion wear, some researchers believe the main reason for the poor machinability of CGI compared to FGI at high speeds is the formation of a protective manganese sulfide (MnS) layer on the rake side of the tool when machining FGI which is not present when machining CGI[16]. The area of MnS seems to be important in improving the machinability of FGI[17].

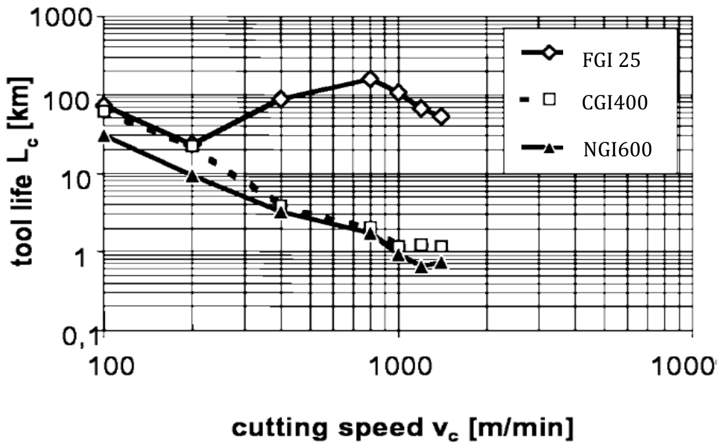

Figure 4: Differences in tool lives with CBN inserts. Tool life in CGI decreases substantially with speed unlike the widely adopted FGI. Adapted from [4].

However, a more recent study found that the formation of an alumina layer on the rake side which is controlled by the aluminum content of the CBN tools is the true reason for the good machinability of FGI. alumina is the second-best material in terms of low solution wear in iron (after zirconia) making it the most stable at high temperatures when machining ferrous alloys. In that study, it was found that when the CBN tool had very low aluminum content, the alumina layer did not form or was easily removed after etching the tool and the machinability of FGI was poor when compared to the tools with higher aluminum content. However, in the high aluminum content CBN tools the layer formed when cutting FGI and was present even after etching the tools for 60 hours but not on CGI as seen in Figure 5.

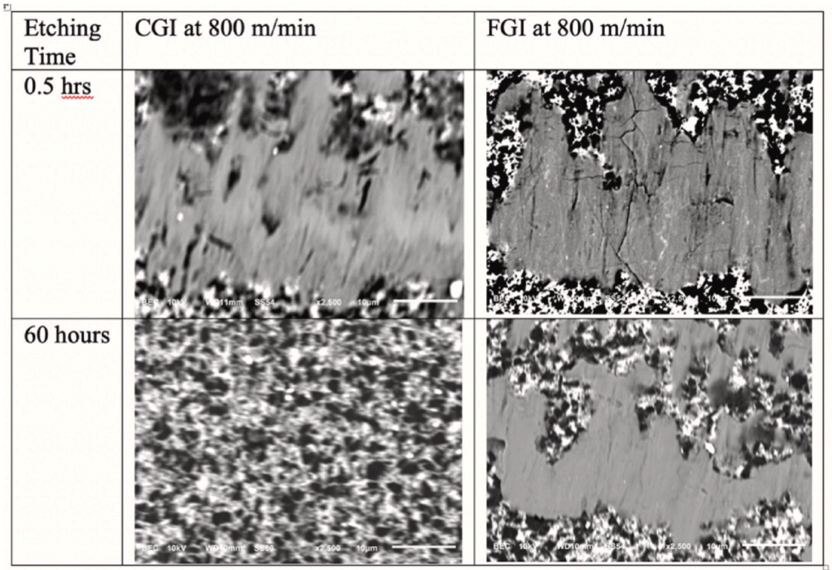

Figure 5: Back Scatter images on the rake faces of CBN tool with high aluminum content at the cutting speed of 800 m/min after cutting CGI and FGI for 350 m. The stability of protective layer after long etching on FGI explains its excellent machinability. Adapted from [8].

It is also believed that the low conductivity of the CBN tools with high aluminum content increased the temperature facilitating the sintering of the alumina protective layer on the tool rake side. Nevertheless, the layer did not form on CGI except for the highest aluminum content tool which also presented the least wear. In that case the layer was easily removed after etching which indicates low stability when compared to FGI[18]. The reason for absence or incomplete formation of the alumina layer when cutting CGI is believed to be the low Mn content of CGI compared to FGI because MnO is the best aid for alumina sintering. Therefore, if the alumina layer could be formed, CGI machinability should improve[19]. This result also has been confirmed by other researchers in turning white cast iron (WCI) which exhibits the worst machinability of all cast iron materials. It was found that the formation of a thick alumina-silicon layer in the CBN tool rake side is strongly correlated to improvement in the wear at high-speed machining of WCI (machined at 160 m/min speed which is considered high speed for this very abrasive material). This wear improvement occurred only on tools with high aluminum content[20].

1.5 Low speed machinability of CGI with carbides

At low speeds the cutting temperature is lower and the abrasion and adhesion effects in FGI, CGI and NGI machining become more important than for high speeds. Because forces and temperatures are usually lower at low speeds, coated carbides are used because despite having lower chemical and mechanical wear resistance, they are easier to produce and therefore more cost effective than CBNs. Carbide inserts consist of carbides of transition metals embedded in a soft cobalt or nickel metal binder phase. Different properties can be obtained altering the proportion of carbides and binder. They have excellent thermal conductivity like metals but high hardness like ceramics[21,22], which provides excellent wear resistance. The most used cemented carbide in machining FGI is tungsten carbide cobalt or WC-Co. However, in WC-Co tools used for iron machining, force oscillations usually generate mechanical wear such as surface damage (due to fatigue and cracking), the hard phases of the material such as pearlite generate abrasion wear, and finally moderately high temperatures generate adhesion and dissolution-diffusion wear. Therefore, coated WC-Co tools for iron machining are designed such that the tough substrate provides resistance to surface damage. Also, a coating layer of TiCN is used which has high hot hardness providing resistance to abrasion wear as well as support for more brittle but more chemically stable coatings above. And lastly, a coating layer of Al_2O_3 is used which has low solubility in iron which should provide resistance to dissolution-diffusion as well as adhesion wear[2].

The machinability of cast irons at low speeds depends on which type of iron is used as well as the cutting tool material and speed. Tooptong et al [23] studied the machinability of the three types of iron at the speeds of 150-350 m/min, with both uncoated WC-Co as well as carbides with a Al_2O_3+TiCN coating in the rake side and TiN+Al_2O_3+TiCN coating on the flank side. At 150 m/min, the machinability of FGI is significantly better in coated carbides. As seen in Figure 6, the flank wear reaches 150 μm at 2km in coated carbides. The same can be said of CGI machining with coated carbide, although the machinability is still poorer than for FGI for all speeds. In general, the machinability of CGI with coated carbides is between that of FGI and NGI. This is explained by the shape of the graphite which gives CGI a toughness (and then a cutting temperature) that is higher than FGI but lower than NGI. Unlike the case of CBN machining at high speeds, no evidence of MnS or Al_2O_3 protective layer is reported at this range of speeds. It has been found that the pearlite content can make machinability in continuous cutting worse at the low speed of 150 m/min, but not at 250 m/min and above [24]. However, the pearlite interlamellar spacing does not have significant effects on machinability [25]. It has been found that when speed is below 200m/min, it is the microstructure features such as the graphite shape (controlling mechanical properties) and the hard abrasive phases that dominates the wear rate of different irons, giving NGI and CGI more wear than FGI but the difference is not as significant as for high speeds [2]. Also, in Figure 6, we can see that when the three irons are machined with coated tools at speeds below 200 m/min, the wear rate is very similar for the three, with CGI being worse than NGI and FGI exhibiting the lowest wear rate. At speeds higher than 200m/min the temperature is higher, which means the dominant wear modes are solution and adhesion wear depending on the solubility of the tool on the work material as well as the tendency for severe plastic deformation of the chip. The result is that alumina coated tools perform better than uncoated carbides for all irons. However, even using Al_2O_3 multilayer coated tools some researchers have found the machinability of CGI to be even 10 times lower than for FGI [24], which is explained by the superior toughness of CGI causing more chip plastic deformation and adhesion on the tool[26].

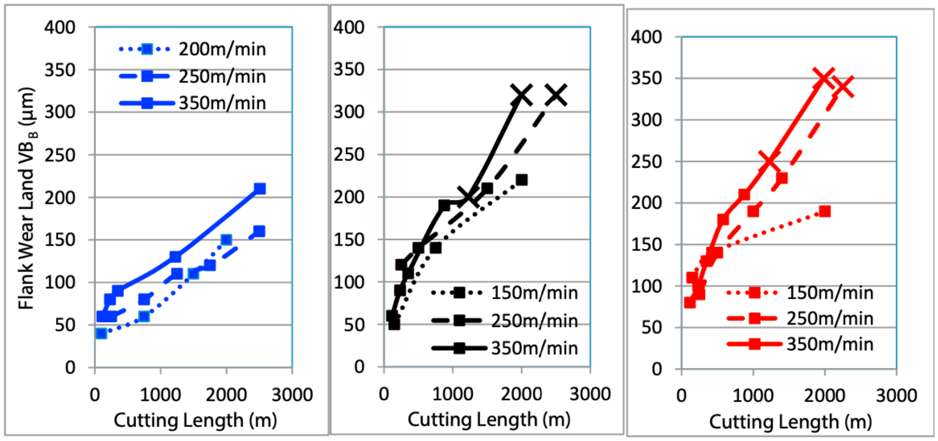

Figure 6: Comparison of coated carbide flank wear when machining cast irons. Tool failure is marked with an x (no fracture was observed for FGI). Adapted from [2].

Another type of tool used at low cutting speeds are aluminum oxide ceramic tools. While coated carbides are better for low cutting speeds, aluminum oxides are better for higher cutting speeds. Given that segmented chips formed when machining cast irons, particularly CGI, the force oscillations cause surface damage which is better managed by the high toughness and fatigue strength of the substrate in coated carbides. On the other hand, at higher temperatures where solution wear and diffusion are dominant, aluminum oxide tools are best, given their hot hardness and low solubility and diffusivity on iron. In this range, coated carbides are debilitated by the high temperatures which can cause more abrasive and solution wear if the substrate or the TiCN is exposed [27]. Researchers have found that alumina tools doped with magnesium can be fabricated, and for these tools the wear has been reduced to only abrasion at speeds of up to 500 m/min when machining CGI. [28]. Masuda et al [29] performed turning of austempered ductile iron (ADI) and found that Zirconia toughened alumina tools are capable of reducing the effect of speed on wear at speeds in the rage of 100-400 m/min when compared to cemented WC-Co with TiC. In Figure 7, alumina and alumina zirconia tools do not exhibit the expected tool life decrease with speed that is present in other tools. On the other hand, TiC toughened alumina tools have better wear resistance at speeds less than 100m/min, but poor life at higher speeds.

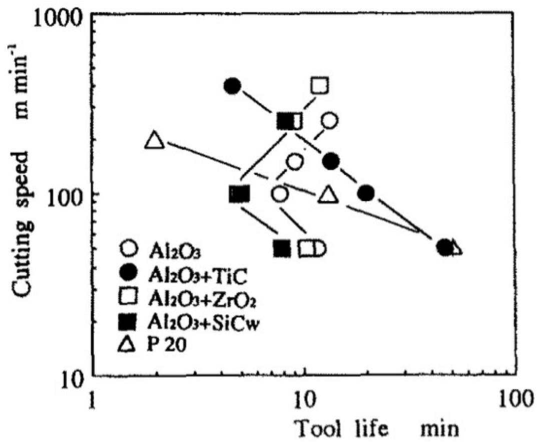

Figure 7: Tool life of various inserts when machining austempered ductile iron. Notice the expected tool life reduction with increasing speed does not always occur in Alumina based tools. Adapted from [29].

Alumina silica tools have shown similar behavior to alumina and alumina-zirconia but in general have more wear. These results agree with the fact that Zirconia is the material with the least solution wear when machining cast irons, making it an excellent additive to alumina in resisting solution wear.

1.6 Interrupted cutting of CGI

In the case of interrupted cutting operations such as milling of CGI, usually two kinds of tools are used: coated carbides and ceramic tools. Because milling is an interrupted cutting operation, the impacting loads are more important than in continuous machining, therefore ceramic alumina based tools due to their low toughness are not recommended [30,31]. However, milling is an interrupted operation, and the temperatures are expected to be lower than in continuous cutting. Therefore, some have suggested that ceramic tools such as SiN which have high solution-diffusion wear in iron but superior abrasion adhesion and surface damage resistance properties could be used [31]. Gabaldo et al [30] performed CGI milling with carbide at the speeds of 350-850 m/min and

SiN tools at 680 and 850 m/min. In general, flank wear is the dominant wear mode when milling CGI [30,32]. Surprisingly, coated carbides perform better than ceramic tools when used at the same speeds. An explanation for such surprising behavior is that despite milling being an interrupted cutting operation with an expected lower temperature than continuous cutting, the temperature is high enough to generate diffusion of iron into the SiN tools therefore weakening the tool during the process and generating more wear. For coated carbides the wear mechanism at low speeds (350-420 m/min) is mostly adhesion and abrasion whereas at higher cutting speeds (420-850m/min) the wear mechanism is adhesion, abrasion, chipping and thermal cracks [30,32].

When performing interrupted cutting experiments on a traditionally continuous operations such as turning, other researchers found that for materials such as NGI (which is similar but more aggressive in wear than CGI) interrupted cutting had less wear than continuous cutting, and a deposition of a Silicon-based material was also observed on the flank side in interrupted cutting, but not during continuous cutting [33,34]. This suggests an interesting interaction that could occur in interrupted cutting with the silicon deposition in FGI, CGI, and NGI that does not occur in continuous machining. In that sense, other experiments in semi-interrupted cutting such as rotary tools implemented on a CNC lathe have proven to increase the tool life when machining some difficult to cut materials such as Inconel 718 and titanium alloys [35]. However, it has been found that the wear when machining CGI with rotary tools is not significantly reduced as compared to conventional turning [36]. Therefore, a controlled and completely interrupted cutting seems to be necessary to improve the machinability in CGI.

1.7 Methods for Machinability Improvement

As mentioned before, the cutting temperature has been modeled as originating from the plastic deformation of the chip and the friction [37]. Models have been developed to describe the heat generated between continuous and interrupted cutting to understand how the chip can be cooled down by implementing different machining processes [38][39].

1.7.1 Cutting fluids for lubrication

In continuous cutting operations, the main problem is the intense heating caused by the severe tribological condition at the tool-chip interface. Therefore, several techniques have been applied to reduce the temperature, mostly with the use of coolants. The goal of these is often to take away the heat generated by the chip deformation as well as increase the lubricity of the chip-tool contact zone. Shaw et al [40] studied the influence of coolants in the machining parameters related to the shear angle and forces. They characterized the lubricants in terms of their potential to reduce the friction angle β and consequently the shear angle and chip thickness and found that sometimes coolants can help reduce the force and enhance chip continuity. Different coolants have been used, ranging from synthetic oils to liquid nitrogen[41].

1.7.2 MQL-and lubricant agents

When lubricants are applied to the cutting zone in large amounts this is denominated flood cooling. Despite the superior cooling effect of this method, this creates a hazard for the operator and increases the machining cost as well as raises some environmental concerns[42]. As an alternative to flood cooling, a technique denominated Minimum Quantity Lubrication or MQL has been developed. In MQL, a minimum amount of lubricant is used in the form of a spray and combined with an air stream in a nozzle (Figure 8) to reach the cutting zone.

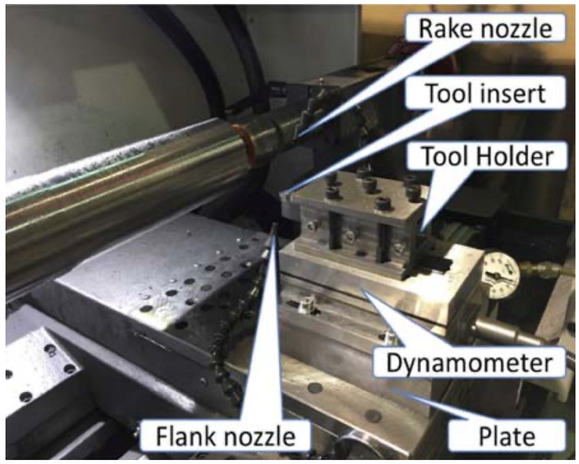

Figure 8: MQL application when turning Titanium alloy. Low volume lubricant reduces severe tool-chip contact which depends on nozzle orientation. Adapted from [43].

This ultimately improves the lubricity and alleviates the severe conditions in the tool-chip contact area. There are two types of MQL application (Figure 9), in one type the oil is atomized and mixed with the air stream before feeding it to the nozzle, and in another type the atomizer is within the nozzle close to the end, so the mixing can occur right before reaching the cutting zone[42]. As an example, turning of Ti64 has been found to improve tool life around 145% by applying MQL on a certain angle from the rake side, and the mixing of graphene platelets increased tool life up to even 200% [44] .However, not all MQL applications have been as successful. For example, Varghese et al. [45] conducted CGI drilling experiments in dry and Minimum Quantity Lubrication (MQL) conditions finding that tool life is not necessarily better for MQL than the dry case. In fact, they found that MQL can increase the cutting force and decrease the chip flow angle in flat coated carbide when turning CGIs, suggesting a negative influence of the oil. However, no changes in the chip composition were found suggesting the lubricant did not change the solution wear mechanism.

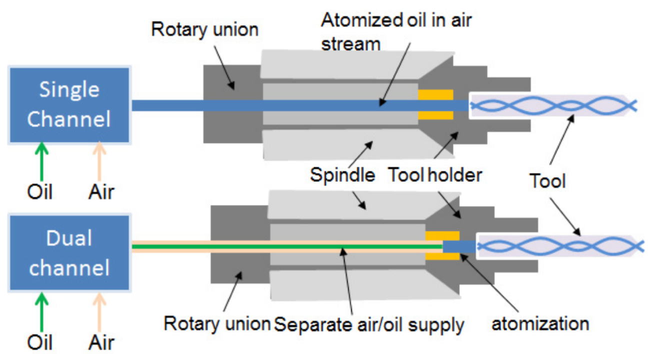

Figure 9: Schematics of MQL system. Adapted from [42].

Another study found that when applying lubricant in turning CGI the radial forces increase, and in some cases when the feed rate was low, the application of lubricant actually made friction worse [46]. This suggests that the tool wear mechanisms in machining in CGI can be very different than for other alloys such as Ti64.

1.7.3 Cryogenic cooling

In cryogenic machining, the goal is to reduce cutting temperature to reduce wear. This also helps in the effective application of MQL because excessively high temperatures can volatilize the lubricants droplets[47]. Two types of technologies are available, supercritical Co2-based oil (scCo2) and liquid nitrogen (LN). scCo2 makes use of a solvent that has been traditionally used for dissolving oils. Because of this property, it can be used to increase oil penetration in the machining process. The liquid Co2 at the supercritical phase and the lubricant are mixed in the reaction chamber. At the cutting tool tip the expansion of the gas generates cooling plus a lubrication effect[47–49]. In CGI drilling, the flank wear presents a reduction of half or less as compared to a regular dual channel MQL system. When turning Inconel, a reduction in wear is also present as compared to traditional lubrication conditions even at high material removal rates [49]. Nevertheless, this method presents great challenges in the cost of adjusting the spindle, as well as the high energy consumption in the Co2 compression and reliability [42]. On the other hand, cryogenic machining is more readily available in CNC machines in the market where liquid nitrogen is delivered at -196 C directly to the cutting zone. In the beginnings LN was sprayed in the cutting area for super cooling but modern machines use minimum quantity LN to refrigerate the tools removing the heat in a more moderate way. Longer life has been achieved in alloys such as titanium compared to conventional lubrication[42].

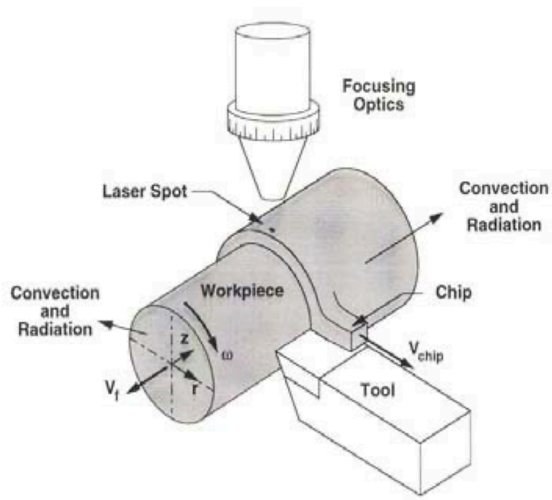

Figure 10: Schematic diagram of LAM. A high energy laser heats the cutting zone reducing cutting forces. Adapted from [43].

1.7.4 Laser-Assisted Machining

Another type of technique used has been Laser-Assisted Machining (LAM) depicted in Figure 10. In this technique, the temperature of the material is increased to decrease the yield strength and therefore the cutting force required. However, LAM requires adequate calibration of the speed and laser power, as a speed that is too low could lead to hardening or melting of the material making machining more difficult, whereas excessive speeds could also lead to poor machinability due to short heating times. Shin et al [43,50] performed LAM tests on CGI, determining that laser power and feed had the largest effect on the tool temperature, without affecting the material microstructure. With LAM, an increase of 60% tool life at feeds of .1mm/rev, better surface roughness and 20% cost savings (from increased material removal rate) for machining can be achieved. In general, it is believed that LAM limitations could be mitigated in the future if more powerful lasers with lower wavelengths can be implemented[51].

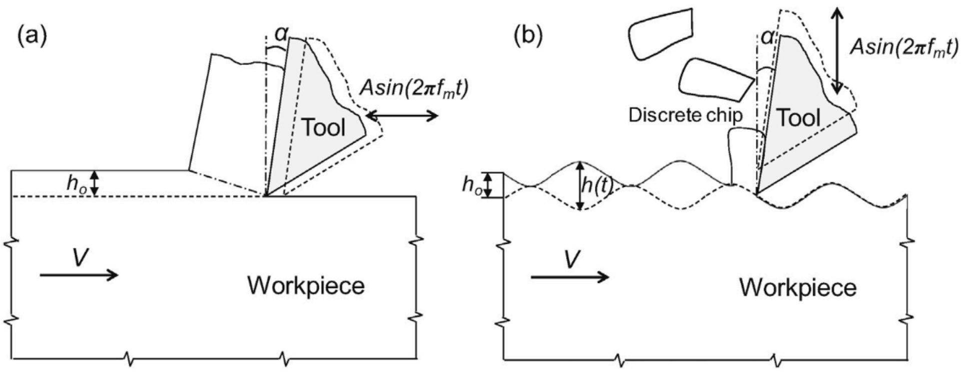

Figure 11: Schematic diagram of Vibration-Assisted Machining for a) velocity-modulation and b) feed-modulation. High frequency is required for velocity-direction whereas a proper frequency ratio is required for feed-direction modulation. Adapted from [52].

1.7.5 Vibration assisted Machining (VAM)

In continuous cutting there is a severe tribological condition in the tool-chip interface which is the main cause of wear. Even when lubricants are applied, there is very poor cutting fluid penetration because the tool is continuously engaged with the material. Therefore, methods in which the tool-chip contact is disrupted or changed are of high interest in order to reduce the wear [38,53]. Vibration Assisted machining (VAM) is one of these methods, in which a vibration is superimposed in the cutting tool motion in the velocity direction (Figure 11a) or the feed direction (Figure 11b) in order to disrupt the tool-chip contact[54]. There are essentially two types of VAM: ultrasonic vibration assisted machining (UVAM) and modulation assisted machining (MAM). In UVAM the frequency is high (> 1 kHz) and is imposed in the velocity direction whereas in MAM the frequency is low (<1 kHz) and it is imposed usually in the feed direction. If the frequency is imposed in the velocity direction, the frequency must be high enough so that the tool can disengage from the chip faster than the speed of the chip. This is given by the condition $2\pi fm >= V$[55,56].

In UVAM, the frequency is usually in the range of 20-40 kHz, about two to three orders of magnitude higher than the workpiece rotational frequency, and the vibration amplitude is usually much lower than the feed rate. There are also two types of UVAM based on the kinematics: 1d (Figure 12a) and 2d (Figure 12b). In 1d UVAM the vibration is only in the feed direction causing an intermittent separation of the tool and the chip when the vibration motion is contrary to the cutting speed [55,57]. In 2d or elliptical UVAM, the vibration also has a component normal to the cutting velocity direction, creating elliptical paths (Figure 12b). This makes the chip to be pushed downwards (inside) the workpiece before a critical point E (Figure 12b), and then the chip is pushed upwards after E until disengaging at point F. In both 1d and 2d UVAM, the vibration tends to create chips of variable thickness by reducing the tool-chip interactions, but the chips remain continuous and therefore the tool temperature is not significantly reduced [58,59]. A study found that in turning steel with diamond tools, a wear reduction is possible when applying both 1d and 2d UVAM. Nevertheless, despite the wear reduction in this process, it has been found that the temperature and cutting energy are not different in UVAM as compared to conventional machining, and the wear reduction is possibly originated by the disengagement allowing air to enter the tool-chip interface and forming a protective oxide layer in the chip surface. It has also been found that a greater gap as well as a lower disengagement frequency in the tool-chip interface decreases the wear even more. Therefore, completely interrupted controlled cutting is the best option in order to reduce the cutting temperature and tool wear[60,61].

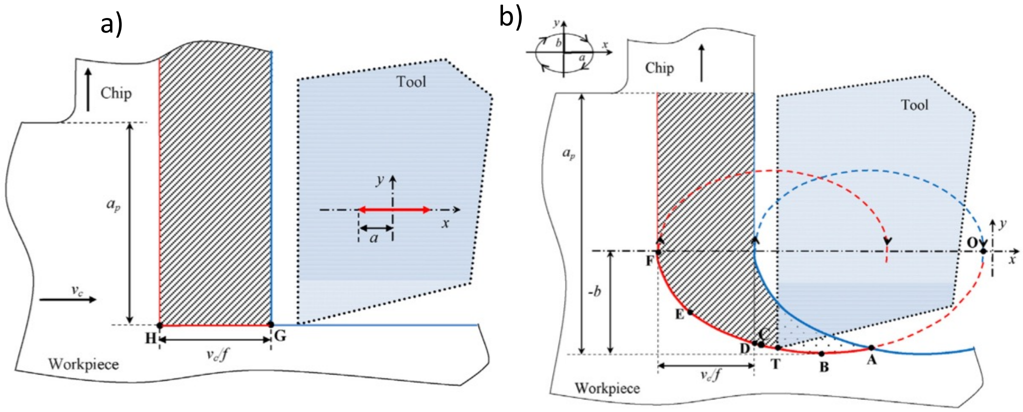

Figure 12: Schematic diagram of UVAM in a) 1d and b) 2d. Despite different disengagement in each case, the chip remains continuous preserving temperature. Adapted from [60].

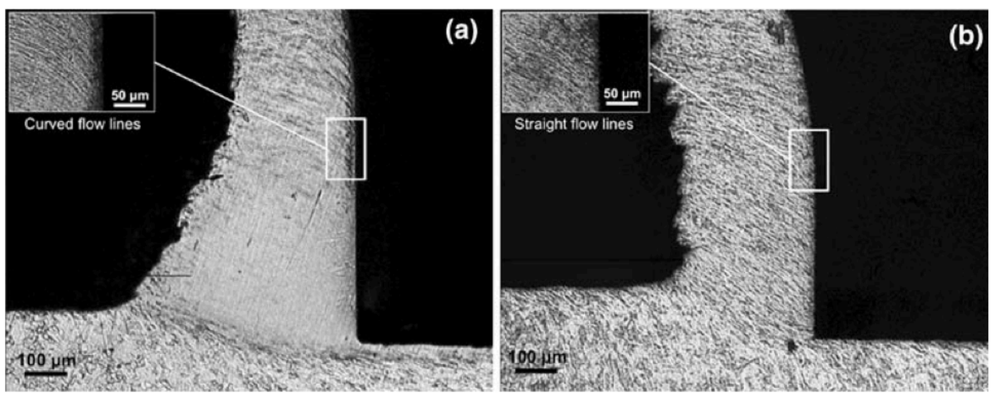

Figure 13: Copper chip formation in a) conventional machining vs b) MAM. Severe plastic deformation is reduced in MAM evidenced by straight flow lines. Adapted from [62].

1.7.6 Modulation-Assisted Machining (MAM)

As mentioned before, the main difference between UVAM and MAM is that MAM applies a lower frequency-high amplitude vibration which can completely disengage the tool periodically from the work material for a significant amount of time as compared to UVAM. UVAM has proven to be capable of reducing the friction coefficient in certain cases and also allow for cutting fluid to penetrate the tool-chip contact[55]. However, in UVAM the disengagement occurs at such a fast rate that does not allow for the tool to cool down and the chip continuous regime to change significantly. In MAM on the other hand, a longer disruption of the tool-chip contact allows for a significant temperature reduction, improved fluid action and reduced friction [55,57]. Also because the chip is severed periodically, the severe plastic deformation of the chip is reduced, which should reduce the cutting temperature (Figure 13) [62]. If the frequencies are controlled in a way that the successive tool paths are not in phase and the amplitude is above a certain threshold, the chips change from continuous to discrete. Given that MAM can change the chip regime from continuous to discrete, it can change chip length making them more manageable as well as increasing the cutting fluid penetration during the continuous machining processes[55,63]. Also because MAM can reduce the severe chip deformation in continuous machining, it is capable of reducing the wear caused by high temperature and forces on the tool[64].

The first application of MAM has been done in drilling (Figure 14). For alloys such as titanium-based Ti64AlV, the poor evacuation of continuous chips create instability in the drill sometimes leading to breakage and severe wear as well as poor surface finish in the part [65,66]. However, drilling of titanium has been successful with the application of MAM[67], where a low frequency vibration is superimposed in the feed direction of the drill by using a piezo-actuator[68–70]. If the vibration frequency and amplitude values are configured appropriately, the chip formed is discrete which results in greater stability of the drill and reduction of the force [71]. In Figure 15, a comparison of the thrust force gun-drilling with both conventional methods and MAM is shown where the instability caused by poor chip evacuation is suppressed by MAM [71]. There is also evidence of significant decrease in the surface roughness (from .8 to .2 μm roughness) when applying MAM in gun drilling[72].

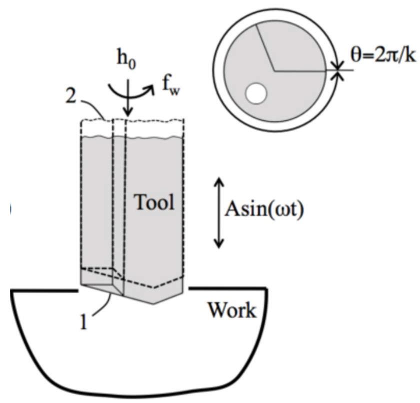

Figure 14: Schematic of Piezo actuated modulation-assisted gun-drilling system, where vibration is applied in the drill feed direction. Adapted from [72].

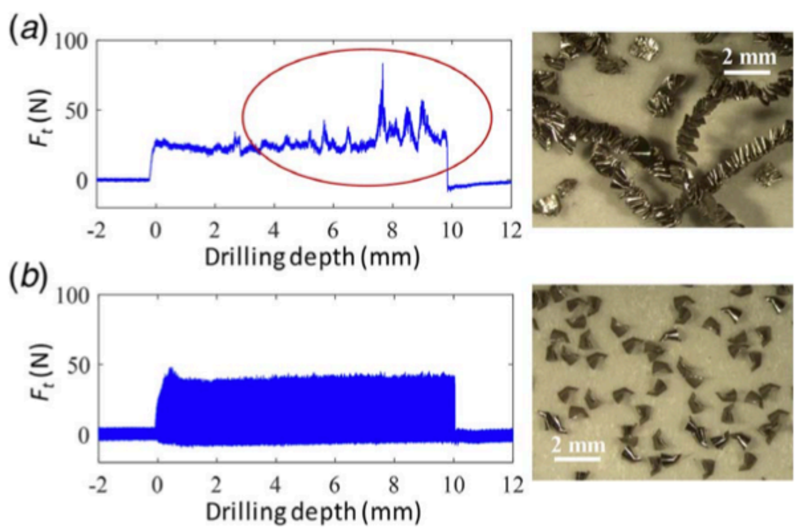

Figure 15: Thrust force and chip morphology in a) conventional drilling and b) modulation-assisted drilling of Ti64. Chatter suppression occurs as well as chip disruption. Adapted from [71].

MAM has been applied to increase the life on CBN tools used to cut CGI at high speeds by at least an order of magnitude when compared with conventional machining (Figure 16) [52,73]. It has also been shown that MAM can change the energy required to perform the cutting process[74]. However, to date, there is no complete description of the way in which MAM changes the cutting regime for CGI. Also, it is not known if different types of tool material such as coated carbides at different speeds can affect the way that MAM changes the cutting regime and the wear.

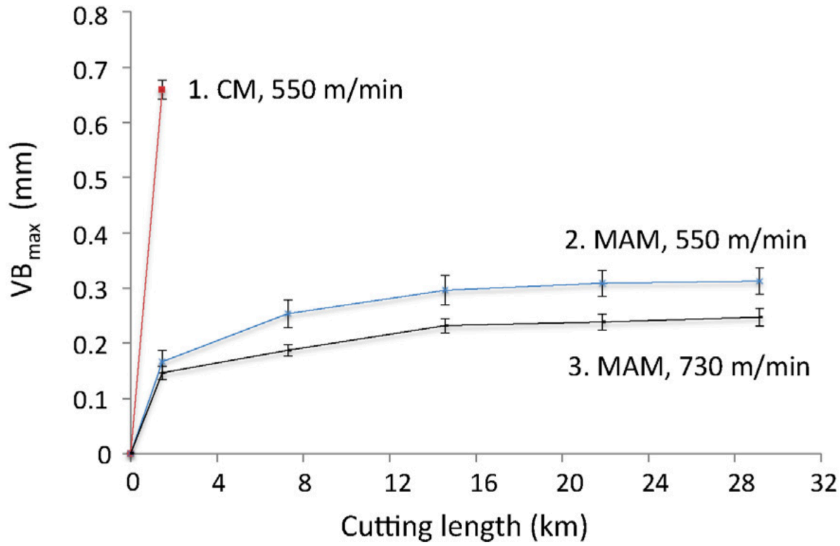

Figure 16: Reduction of flank wear with cutting length for cBN turning of CGI. MAM improves tool life by an order for magnitude in CGI. Adapted from [52].

1.7.7 MAM turning theory

A kinematic model for the conditions required for discrete cutting on MAM has already been derived [72,75]. To understand MAM, it is necessary to review the kinematics of conventional machining in turning (here labeled as CM). In CM, the constant feed rate generates a parallel helical tool path in the revolving workpiece surface (Figure 17a), so the tool path never intersects and the chip is continuous. In MAM, a low frequency vibration is imposed on the tool in the feed direction generating a sinusoidal tool path as shown in Figure 17b and Figure 17c. The difference is that the phase between successive path segments in Figure 17b is π, whereas the phase in Figure 17c is 2π. If the wave amplitude A and the frequency are selected such that they follow the following equation, the tool path will intersect and the cutting regime will be discrete instead of continuous[75]:

$$\frac{A}{h_0} \geq \frac{1}{2\sin\left(\frac{\varphi}{2}\right)} \quad (1)$$

Where A is the amplitude of the tool vibration, h_0 is the feed rate, and φ is the phase between successive path segments in each revolution. The phase and the vibration and rotation frequencies are related by:

$$\varphi = 2\pi\left(\frac{f_m}{f_r} - INT\left[\frac{f_m}{f_r}\right]\right) \quad (2)$$

Where f_m is the oscillation frequency; f_w is the workpiece rotational frequency (=RPM/60). If we plot the values of the amplitude-feed ratio vs the phase angle, the curve in Figure 18a is obtained. This curve gives the threshold for the transition from continuous cutting to discrete cutting. It is seen that the minimum amplitude required occurs when the phase angle between path segments is π, which is the case shown in Figure 17b.

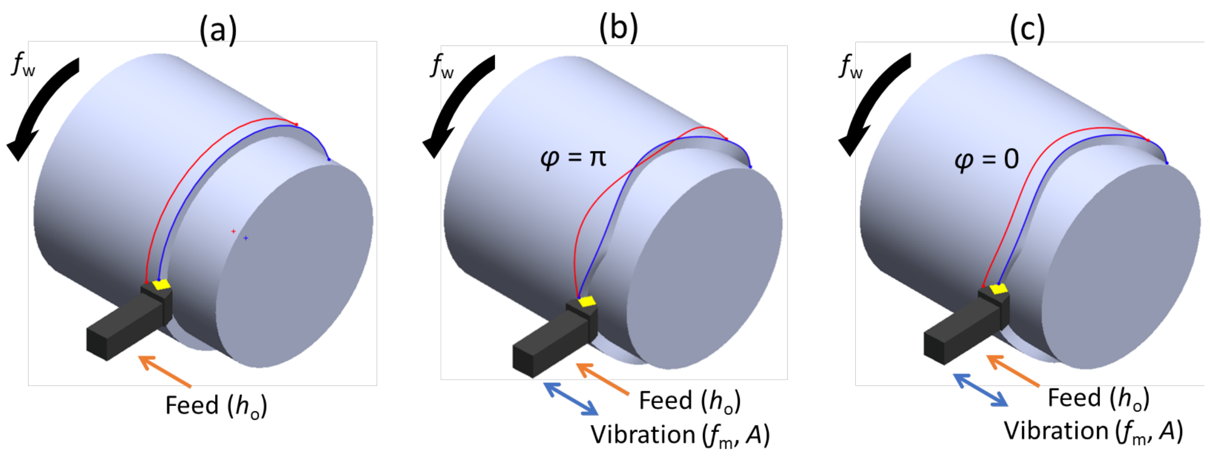

Figure 17: Schematic of (a) CM, (b) MAM out of phase turning, (c) MAM in phase turning. Interrupted cutting in MAM is possible by the tool path intersection.

As an extreme case, if the phase between path segments is 0 or 2π then the path will never intersect leading to continuous cutting like in CM (Figure 17c). If we plot Figure 18a in the frequency ratio space we obtain Figure 18b, where we see that the amplitude has a minimum at several frequency ratio values. Specifically, the amplitude required will be minimized if the frequency ratio takes half integer values, that is 0.5, 1.5, 2.5 etc.

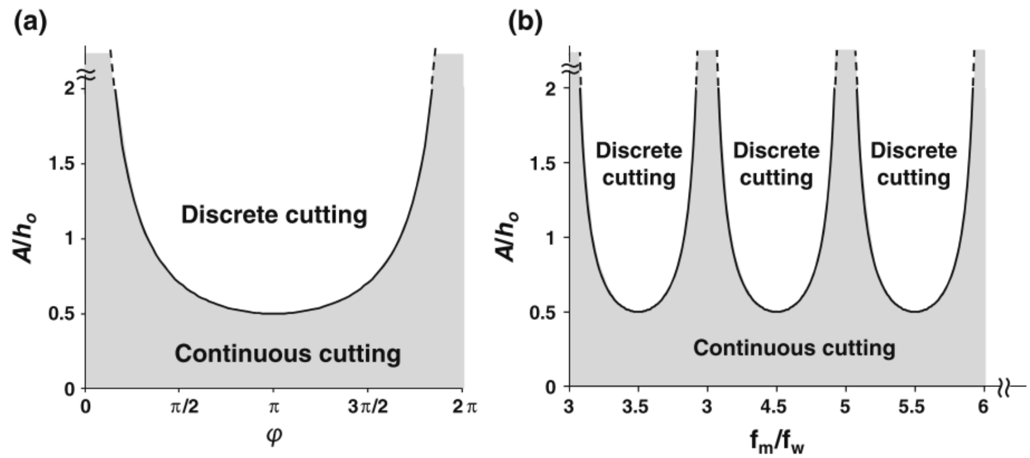

Figure 18: Cutting regimes of MAM in a) ϕ-A/ho space and b) fm/fw-A/ho space. The discrete cutting regime corresponds to disengagement of the tool. Adapted from [60].

1.8 Summary and research questions

This section intends to summarize what is known about the machinability problem of CGI and how current approaches have been developed to mitigate the problem. This serves as a base for the research questions that this dissertation will try to answer. In Table , the fundamental phenomena governing the machinability of CGI in different regimes are summarized. The open questions about the machinability problem are stated for each regime as well.

At high speeds (>400m/min), the dominant wear mode is crater wear which is controlled by the solubility of the tool material in CGI. One of the best materials is Alumina due to low solubility in CGI and because it can form protective tool layers reducing crater wear. However, other promising materials such as Zirconia, with the lowest solubility in CGI has not been studied yet.

At low and medium speeds (<400m/min), it has been found that crater wear as well as flank wear are prevalent, however, flank wear is dominant due to significant adhesion of CGI on the tool. CGI exhibits very poor machinability compared to FGI. However, several aspects such as effect of lubricants, interrupted machining, adhesion behavior and layer formation have not been studied for CGI at these speeds. Also, the main wear mechanism of coated carbides when cutting CGI is not fully understood.

All the techniques described intend to reduce the severe condition at the tool-chip interface by reducing the friction, the cutting force, or the temperature. MAM seems to be the most promising technique for the machinability improvement of CGI due to the capability to adjust the frequency and amplitude changing the cutting regime, and significant improvements on CGI machinability with cBN tools have already been published. However, it is not known if MAM can improve the machinability of CGI with other types of tools, such as the more readily available coated carbides which are used in industry for iron machining. Even further, the mechanism by which MAM changes the cutting regime and affects the machinability variables such as wear, temperature and force is not fully described or understood. The following problem statement explains how this dissertation can fill this gap in the knowledge of the machinability of CGI and MAM.

1.8.1 Problem statement

The main question this work intends to answer is what is the mechanism that causes MAM to improve the machinability of CGI in continuous cutting. To understand this mechanism, a MAM turning setup is developed and the machinability parameters such as wear, temperature, and force are characterized.

CHAPTER 2:DESIGN OF A MODULATION-ASSISTED MACHINING DEVICE FOR EXTERNAL CILYNDRICAL TURNING

2.1 Methodology of the design process

As mentioned in previous chapters, this dissertation will focus on the study of Modulation-Assisted Machining of Compacted graphite iron in the case of turning. For performing the experiments, a device is built that can implement this novel cutting process in the case of external cylindrical turning. The design stages followed in the development and a brief description of the findings during each stage are presented in the following sections.

2.2 Design goal statement

The goal is identified as to design a device that can perform Modulation-Assisted Turning of compacted graphite iron with coated carbide tools.

2.3 Performance specifications and constraints

In the design process, several performance specifications were identified as follows. First, because the device is intended to compare the case of conventional turning with MAM, it had to be implemented on an available CNC lathe that is used for conventional turning of CGI. Because coated carbide tools are to be used, the design must be able to accommodate for the means to hold these types of tools considering their material and geometry characteristics. Given that MAM depends on imposing a vibration in the feed direction, the design must allow a degree of freedom in this direction and impose vibration on the feed. The vibration on the feed direction has to be imposed in a very accurate and controllable manner in order to study different kinematic conditions in MAM. Also, the design must be sturdy enough to withstand the forces during the cutting process, while avoiding excessive deformation that could change the kinematic conditions required for MAM as described in the background chapter. The design should also avoid an excessive weight and size because this could change the conditions normally found in conventional turning, as well as increasing the danger for the operators before, during and after the test.

There are several mechanisms for the vibration of the tool in the feed direction as required in MAM. Given the fact that this study intends to control the frequency ratio to study the effect of MAM on the tool wear when machining CGI, a device that can generate a sufficient amplitude at different frequencies is required. Therefore, the device must be controlled by an electrical signal which could be adjusted easily to change the frequency of vibration for different cases. For this purpose, piezoelectric materials are ideal given that they can easily convert an electrical impulse into a mechanical response. The market for large amplitude and high frequency piezo actuators is currently limited to amplitudes of up to 200 μm, however this is adequate given that it is close to the feed rate used in industry for conventional machining of CGI [23].

Traditionally, lubricants are used to improve the machinability in turning, therefore the design must be able to allow for the application of these lubricants in the cutting process. Given that cutting force is an important parameter used in industry to monitor cutting tool life, the device must allow for the incorporation of a dynamometer during the test. Another important aspect is the measurement of the tool temperature during the cutting, which required the device to allow for the implementation of thermocouples during the cutting process. Therefore, the design requires the insert and assembly to be accessible to install and adjust the connections of dynamometer, thermocouple, and lubricant nozzle.

2.4 Detailed design

The design schematic and setup of the modulation-assisted machining device for turning is shown in Figure 19. The experimental setup of the piezo actuated modulation-assisted machining system, together with the power and data acquisition devices is shown in Figure 20. The setup is implemented on a Haas TL-1 toolroom lathe. The tool vibration device consists of a stationary frame, two linear guides, a moving stage, and a piezo stack actuator. The turning tool holder is fixed to the moving stage which is supported by the linear guides whose rails are fixed on the stationary frame. The linear guides allow only linear motion but restrict bending and rotation of the moving stage. The casing of the piezo stack actuator is fixed to the stationary frame while its actuator head is connected to the moving stage. The vibration of the turning tool is driven by the piezo stack actuator. The piezo stack actuator used in the study has a stroke of 0.1 mm and can generate a maximum driving force of 4000 N. The sensitivity is 1mv for 0.1 nm which allows for accurate control of the feed vibration.

During MAM turning, the traditional turning parameters including workpiece rotation speed (RPM), tool feed per revolution, and depth of cut are controlled by the lathe; the frequency and amplitude of the turning tool vibration are controlled by the sinusoidal driving voltage input to the piezo stack actuator.

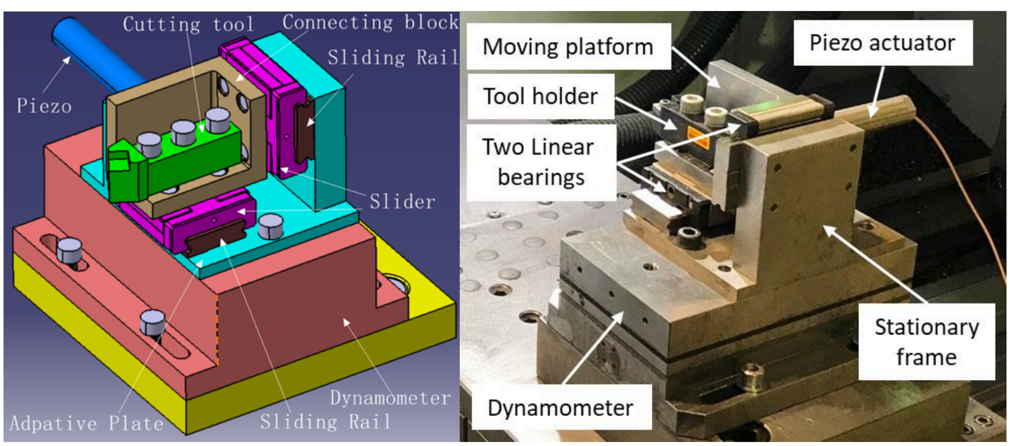

Figure 19: Design schematic and physical setup of modulation-assisted machining device. Adapted from [76].

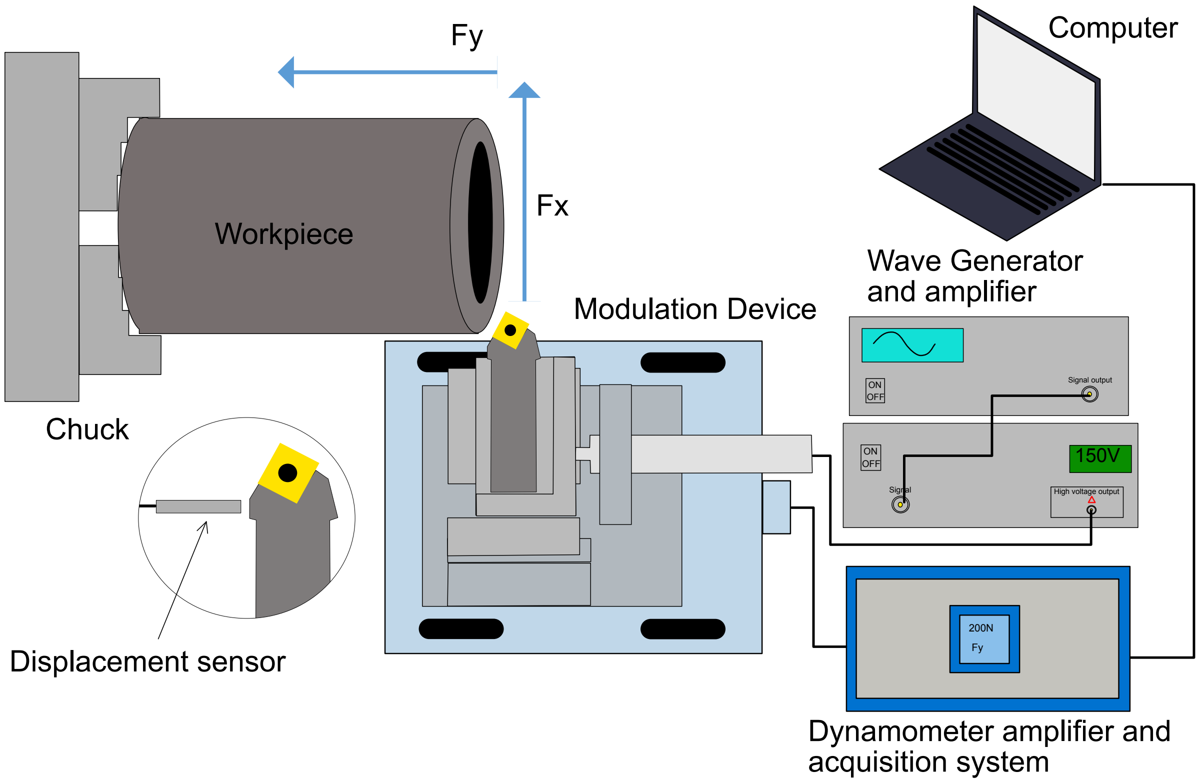

Figure 20: Experimental setup for piezo actuated modulation-assisted machining system.

The driving voltage is provided by a waveform generator (BK 4007B) and a power amplifier (MMech PX200). To enable cutting force measurement, the tool vibration device is mounted onto a Kistler dynamometer plate (9257B) which is fixed onto the carriage of the lathe. The force signal is recorded using a data acquisition system with a sampling rate of 5000/s and processed with a low-pass filter with a cutoff frequency at 500 Hz.

2.5 Design calibration and testing

To assure the correct functioning of the system during the cutting experiments, a dynamic characterization of the system was performed to determine which cutting conditions can be used in the turning experiments. The parameters determined are the natural frequencies, the effective moving mass, the effective stiffness, and the amplitude-frequency-voltage response.

2.5.1 Static deflection test

The effective stiffness of the assembly is calculated to avoid excessive compression which would reduce the amplitude values during the cutting process. The stiffness coefficient was estimated by slowly compressing the assembly from the cutting tool tip and reading the force (Fy) generated on the dynamometer and the displacement (u) on the capacitive probe as in Figure 21. The results are shown on Figure 22 and the stiffness value obtained was approximately 12.3 N/µm.

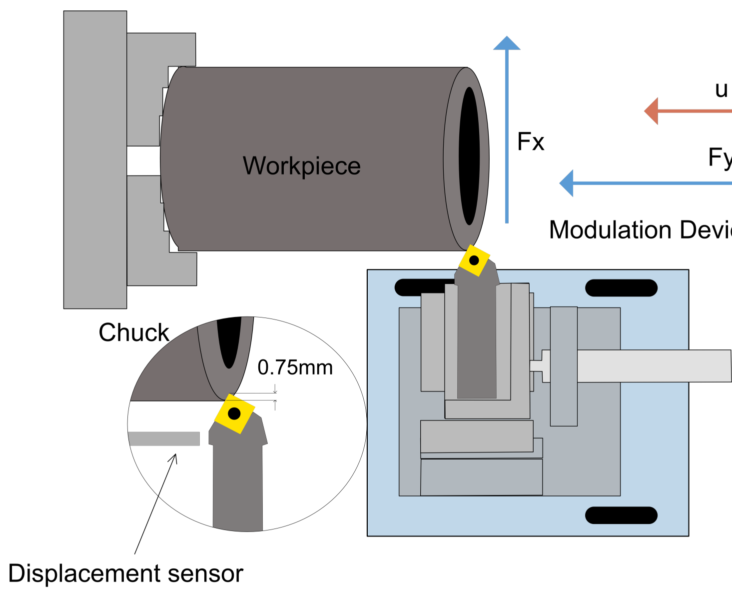

Figure 21: Static deflection test. Tool tip is compressed against workpiece recording displacement (u) and force (Fy).

Given that the stiffness according to the catalog for this piezo actuator is 20 N/µm, the stiffness differences can be attributed to the deflection of the tool holder insert which is not in the same axis as the piezo actuator.

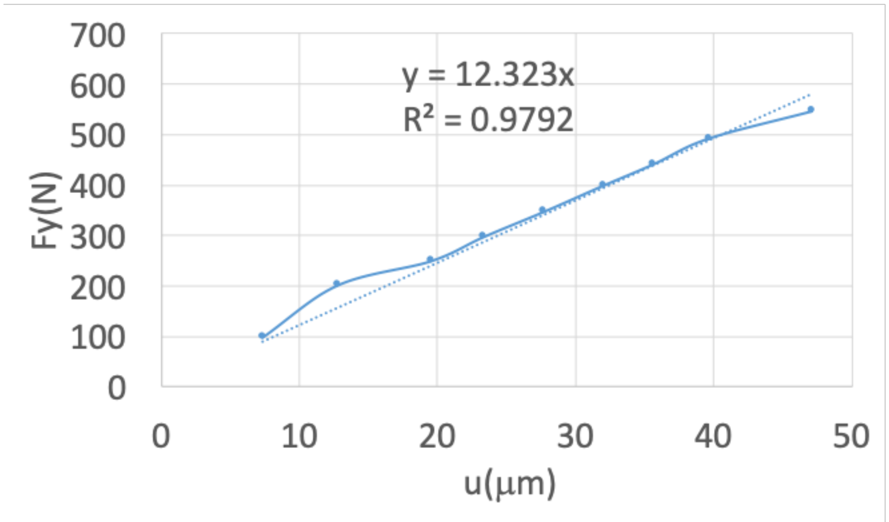

Figure 22: Force-displacement response and stiffness of the modulation-assisted machining device.

2.5.2 Impact hammer test

To determine the resonant frequencies of the assembly and determine a safe operational vibrational frequency range, modal analysis was performed with an impact hammer test. In this test, a PCB sensor (model: 356B11 SN 230172) was placed on the back side of the tool holder right behind the cutting tool show in Figure 23, and the assembly was then excited with an impact hammer hitting the cutting insert in the X(radial), Y(feed) and Z(cutting) directions.

The force read from the hammer as well as acceleration from the sensor on the toolholder were used to calculate the frequency response functions (FRF) in each direction using the Discrete Fourier Transform. An example of the calculated FRF is shown in Figure 24 and the resonant frequencies obtained for each direction are presented on Table 2.

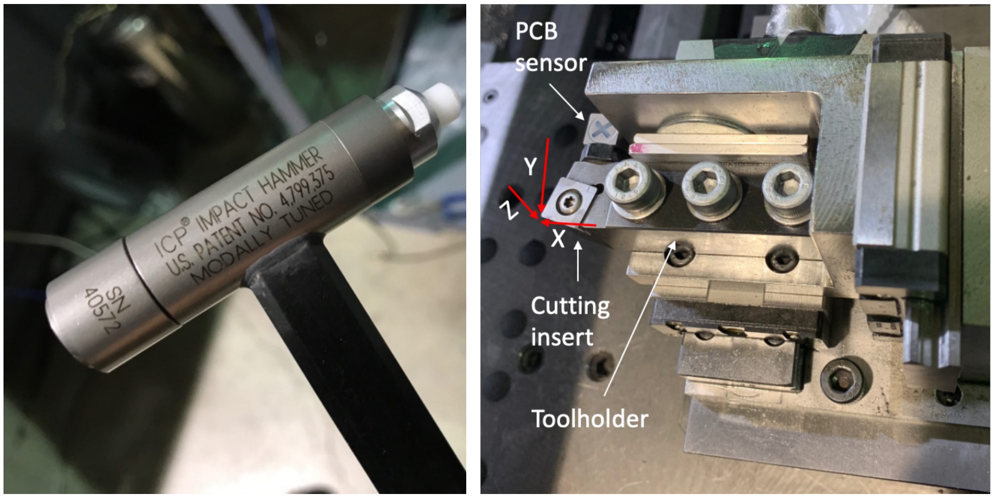

Figure 23: Impact hammer and PCB sensor location on setup with impacting directions.

Here the most important frequencies are those in the feed direction because that is the direction in which the vibration is imposed in MAM. Because the lowest resonant frequency in the feed direction is 375 Hz, the frequencies in the MAM experiment will be kept below this value to preserve the structural integrity of the design.

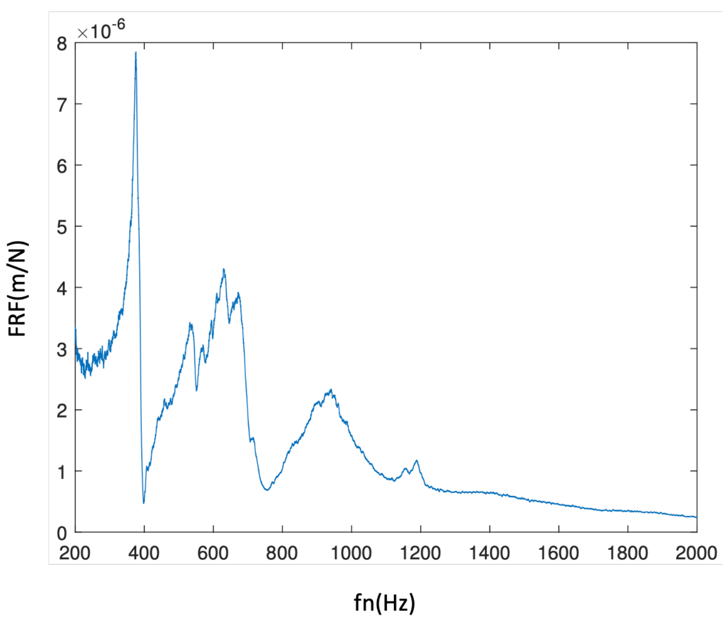

Figure 24: Calculated frequency response function for the impact hammer test in the Y(feed) direction.

Table 2: Resonant frequencies and damping ratios from hammer test in MAM device.

Direction	Resonant frequency (Hz)
Cutting direction (Z)	258
	327
	367
Feed direction (Y)	375
	638
	934
Radial direction (X)	662

2.5.3 Vibration frequency-amplitude test

This test ultimately determines the assembly moving mass as well as the displacement-frequency-voltage relationship. In this test, a sinusoidal voltage is applied to the piezo and the forces and displacement in the structure are recorded. The forces due to the moving mass inertia are recorded with the dynamometer. To measure the displacement, a capacitive displacement sensor (Capacitec HPC-40) is placed on the toolholder as close as possible to the cutting insert as in Figure 20.

The moving mass is determined to avoid inertial loads that are excessively large compared to the maximum axial load the piezo can take. With the following equation the moving mass was estimated:

$$|Fy| = m|a_y| = m\omega^2|Xy| \quad (3)$$

Where, Fy is the force amplitude in the feed direction (the vibration direction) in the no-cut condition, m is the assembly mass, ω is the vibration frequency and Xy is the displacement amplitude in the feed direction. The force is measured using the dynamometer and the displacement is measured with the capacitive sensor. The measurement was performed at different frequencies for a 50, 100 and 150 V voltage and frequencies of 20, 40, 60, 80 and 100 Hz, giving a total of 15 tests. The value obtained was 1.24 kg and the variation coefficient in the moving mass value obtained is less than 6%. The initial design estimation assuming all parts are made of 4340 steel is 1.3 kg, therefore the value obtained from this test is close to what was expected. Given that all frequencies were below 200 Hz, this value is used again in equation to estimate the maximum inertial load, giving a value of 100 N which is well below the piezo specification both for maximum tensile and compressive loads (400 N and 3000N respectively).

The amplitude-frequency-voltage response of the assembly is determined to confirm that there is not a significant variation of the amplitude with the frequency for a given voltage. As it was expected that the system would have different oscillating amplitudes depending on the voltage and frequency input to the piezo, different values were tested and the resulting amplitude was recorded and compared, as shown in Figure 25.

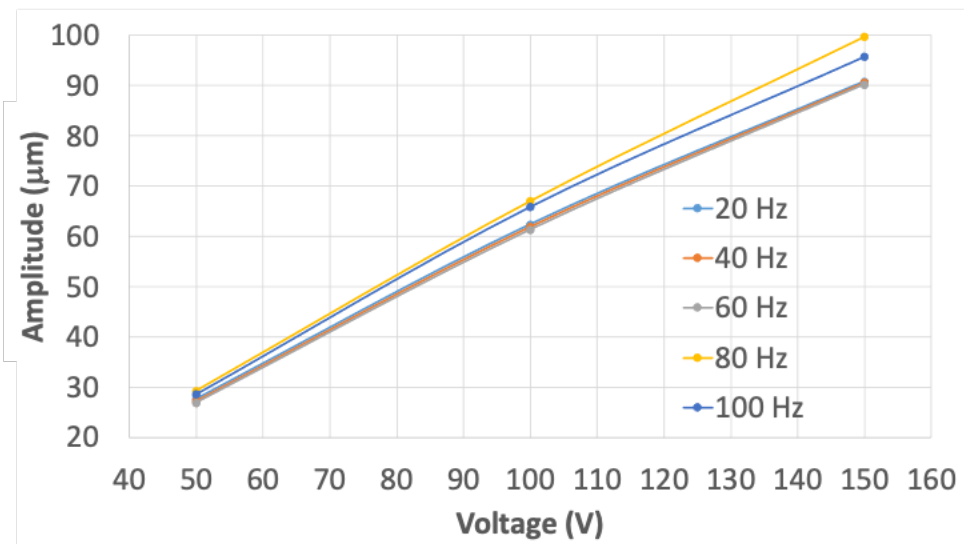

Figure 25: Amplitude vs Voltage for different signal frequencies in the MAM system.

It is interesting to note that at values higher than 100 V, the 80 and 100 Hz frequencies produce amplitudes slightly higher than the other frequencies. However, the amplitude variations are always less than 10 µm which is well within the specification of conventional machining processes.

For the experiments in this work, the maximum voltage of 150 V and frequencies in the range 40-150 Hz are used which should result in an peak-to-peak amplitude range of 90-110 μm. According to the equations in chapter 2, to have complete tool disengagement the lathe feed rate is set to .04mm/rev or 40mm/rev which is less than the peak-to-peak amplitude of vibration.

2.5.4 Cutting test

This test intends to confirm the change from a continuous cutting regime in CM to a discrete cutting regime in MAM. Also, it is used to determine the MAM vibration amplitude reduction due to the cutting force. As mentioned in the background chapter, the vibration amplitude reduction during the cutting is important because if the amplitude is smaller than the critical amplitude for disengagement, the cutting path will not intersect, and a discrete cutting regime will not occur.

For this test, the titanium alloy Ti64AlV is selected since it generates continuous long chips during conventional machining. This allows to easily confirm the discretization of the chip even during the machining process. Figure 26 shows the measured tool displacement, feed force, and resulting chip morphology for both conventional turning and MAM turning of Ti6Al4V at dry condition.

Both tests were conducted at the following baseline turning condition: the feed rate was 0.05 mm/rev; the depth of cut was 1mm; the cutting speed was 122 m/min. The initial workpiece diameter was 72.458 mm. The workpiece rotational frequency fw = 9.18 Hz. Therefore, the modulation frequency fm for MAM was 96.45 Hz. In conventional turning, the thrust force is steady at about 110 N. This force caused a negative displacement or deflection of the turning tool at about 10 μm in the tool feed direction. This indicates the stiffness of the modulation turning tool post in the actuation direction is about 11 N/μm, which is close to the value determined in the static no-cut test. It is seen the force value is far from zero signaling continuous cutting and the chip produced in conventional turning is continuous and often tangled. The continuous chip in conventional turning is problematic for the operator.

In MAM turning, the force oscillates signaling chip thickness variation and disengagement of the tool. The amplitude of tool oscillation is about 90 µm before the turning starts. This amplitude is reduced to about 70 µm during the turning process.

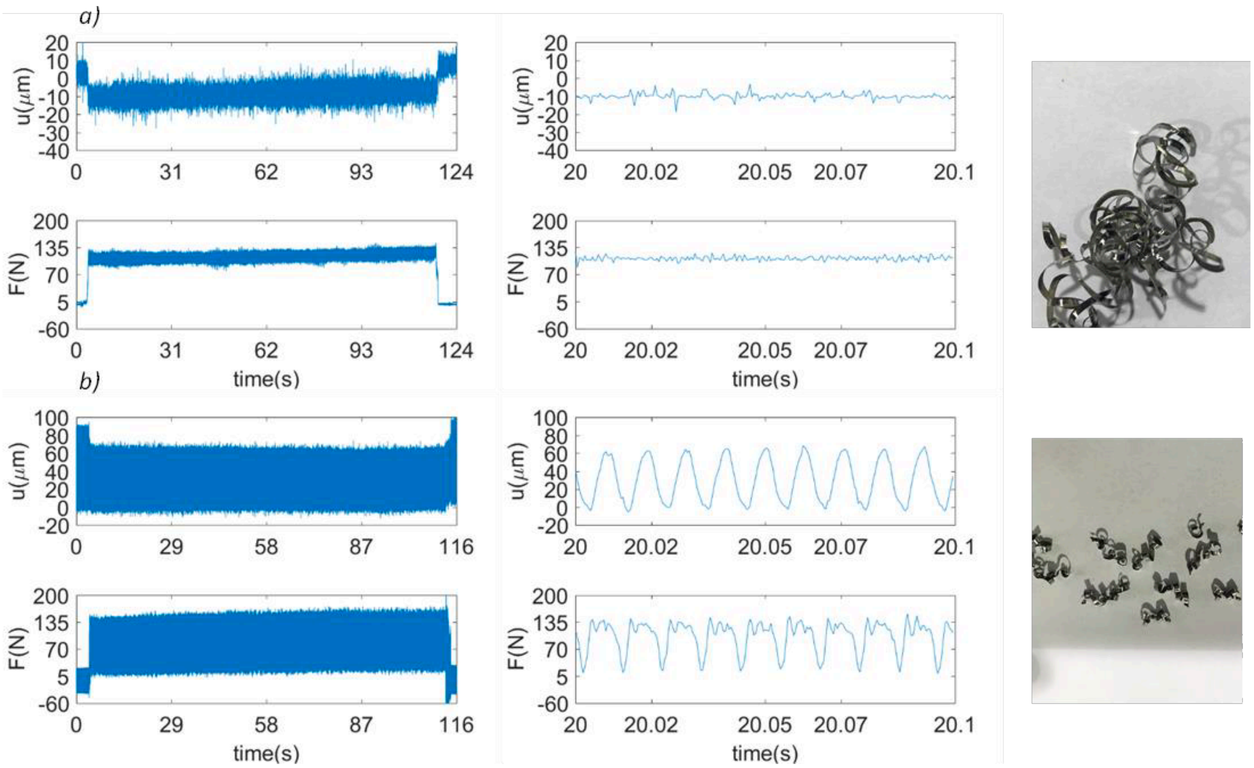

Figure 26: Measured displacement (u), thrust force (F) and chip morphology in (a) conventional and (b) MAM turning of Ti6Al4V. Adapted from [76].

Given that the peak-to-peak amplitude is larger than the feed rate, discrete cutting still occurs as evidenced by the cutting force dropping to almost zero each cycle (the force might not reach zero due to the rubbing of the tool nose with the workpiece). The reduction in oscillation amplitude is caused by the dynamic loading intrinsic to the MAM process. The amplitude of the feed force variation is about 130 N. Because the thrust force presents a more complicated shape than a constant or sinusoidal value, the stiffness should not be used to predict the reduction based on a single value of cutting force. However, the proportion between feed force amplitude and amplitude reduction in MAM can be used to roughly estimate the maximum deflection a different feed force value maximum could have. In this case, this value is estimated as 6.5 N/μm. As explained later in the coming chapters, feed forces of CGI oscillate around the order of 200N. Based on the proportion calculated, a reduced vibration amplitude of 60 μm is expected and a feed rate of 40 μm is used to guarantee discreet cutting.

2.6 Summary

From the tests performed it can be concluded that the device developed can perform Modulation-Assisted Machining in external cylindrical turning. The first test confirmed that the stiffness of the device is not significantly compromised which could significantly reduce the vibration amplitude leading to incomplete cutting interruption. The second test determined a safe range of operation which should be far from the resonant frequencies to preserve the structural stability. The third test determined that the vibration amplitude can be controlled independently of the vibration frequency. Finally, the fourth test determined that the device can ultimately change the cutting regime from continuous to discrete which is evidenced by the sinusoidal displacement, the force variation, and the chip morphology of the test material during MAM. Given that the design is such that it can be easily installed and removed in minutes, it should be suitable for industrial settings applications where the time for tooling changes is an important requirement for production efficiency.

CHAPTER 3: MODULATION-ASSISTED MACHINING OF COMPACTED GRAPHITE IRON WITH COATED CARBIDE TOOL IN THE DRY CONDITION

3.1 Summary

As mentioned in the previous chapter, CGI is a very promising material that could replace FGI for diesel engine block applications due to superior mechanical properties. However, CGI adoption is hindered by its poor machinability compared to the more widely used FGI grey iron. In fact, CGI is usually machined in industry with coated carbide tools at speeds below 200 m/min due to the fast wear tool wear rate at higher speeds. This study investigates the effect of modulation-assisted machining on tool wear in the case of dry turning of CGI with coated carbide tools. A new MAM turning setup was implemented for conducting the longitudinal turning experiments. Tool wear, cutting forces and tool temperature were recorded and characterized for both conventional machining turning and MAM turning at three cutting speeds: 150 m/min, 250 m/min and 350 m/min. The results show wear reduction by MAM is not significant at the low cutting speed (150 m/min), but it is quite significant at the higher cutting speeds (250 and 350 m/min). The cutting force and temperature results can be well correlated with the wear results, revealing the dependency of the forces and temperature on the tool wear and the severity of iron adhesion. This study demonstrates the potential of MAM in enhancing the productivity of machining CGI with the coated carbide tool. The results are also useful for better understanding the wear mechanism in cutting CGI with the coated carbide tool.

3.2 Materials and methods

Figure 27 shows the MAM turning setup developed for this study. The setup was implemented on a Haas TL-1 toolroom lathe. The tool vibration device consists of a stationary frame, two linear guides, a moving stage, and a piezo stack actuator. The turning tool holder is fixed to the moving stage which is supported by the linear guides whose rails are fixed on the stationary frame. The linear guides allow only linear motion but restrict bending and rotation of the moving stage. The casing of the piezo stack actuator is fixed to the stationary frame while its actuator head is connected to the moving stage. The vibration of the turning tool is driven by the piezo stack actuator. The piezo stack actuator used in this study has a stroke of 0.1 mm and can generate a maximum driving force of 4000 N. During MAM turning, the traditional turning parameters including workpiece rotation speed (RPM), tool feed per revolution, and depth of cut are controlled by the lathe; the frequency and amplitude of the turning tool vibration are controlled by the sinusoidal driving voltage applied to the piezo stack actuator. The driving voltage is produced by a waveform generator (BK 4007B) and a power amplifier (MMech PX200).

To enable cutting force measurements, the tool vibration device was mounted onto a Kistler dynamometer plate (9257B) which is fixed onto the carriage of the lathe. The force signal was recorded using a data acquisition system with a sampling rate of 5000/s and processed with a low-pass filter with a cutoff frequency at 500 Hz. Furthermore, tool temperature was measured using a 36 AWG K-type thermocouple secured on the tool rake face with a polyimide film tape (see inset of Figure 27). The thermocouple junction was positioned at the location that is 0.83 mm from the side (main) cutting edge and 2.5 mm from the end (minor) cutting edge. This location was chosen based on our trials: it is the location at which the thermocouple junction will not be disturbed by the chip flow but is as close to the tool- chip interface as possible to estimate the tool temperature. The temperature history was recorded at a sampling rate of 1/s using a digital thermometer (Fluke 54-II). Note the measured temperature is not exactly at the tool-chip interface, but it should be sufficient to use as a reference of tool temperature for comparison among different cutting conditions.

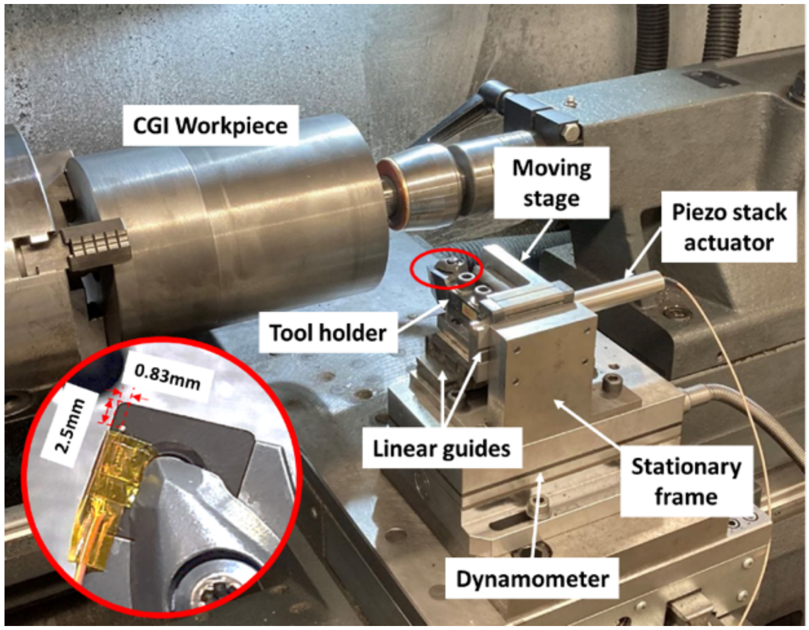

Figure 27: Experimental setup for dry MAM turning with coated carbides. Adapted from [77].

The CGI workpieces (from SinterCast AB) have hollow cylindrical shape with an outer diameter of 145 mm and an inner diameter of 98 mm, and a length of 204 mm. The grade is classified as GJV-450 by the standard ISO 16112:2017 with a tensile strength of 450 MPa. The microstructure contains graphite agglomerations of vermicular shape, and the matrix is fully pearlitic. The coated carbide insert used for turning is Sandvik Coromant SNMA 12 04 08-KR 3205, which has two- layer TiCN and Al_2O_3 coating on the rake face and three-layer TiCN, Al2O3 and TiN coating on the flank face [78]. The used toolholder is DSBNR 2020K which results in -6° rake angle and 15° side cutting edge angle.

Table 3 lists all the turning tests in this study. All tests were conducted in dry conditions. The feed rate (h0 = 0.04 mm/rev) and the depth of cut (d = 1.5 mm) were not varied while the cutting speed (Vc) is varied at three levels, i.e., 150, 250 and 350 m/min, for both CM and MAM turning. For MAM turning, the frequency ratio (fm/fw) was controlled to have a half integer value according to Eq. (1), so the phase of the wave tool path is always at $\varphi = \pi$. The frequency ratio is

9.5 for Vc = 150 and 250 m/min and is 6.5 for Vc = 350 m/min. With the two different frequency ratios, the vibration frequency for Vc = 250 and 350 m/min are roughly the same (both in the range ~90 – 110 Hz). The frequency varies within a range in each MAM turning test which is to accommodate the change of fw at different workpiece diameter. The vibration amplitude is controlled by the sinusoidal driving voltage amplitude. The peak-to-peak amplitude of the driving voltage was set to Vpp = 150 V for all MAM turning tests. This driving voltage corresponded to a peak-to-peak tool vibration amplitude (2A) of about 90 μm calibrated at the no-cutting condition.

Table 3: Turning test conditions. Adapted from [77].

Test name	Cutting Speed (m/min)	Feedrate (mm/rev)	Depth of cut (mm)	f_m/f_w	f_m (Hz)	V_{pp} (V)
CM-150	150	0.04	1.5	-	-	-
CM-250	250	0.04	1.5	-	-	-
CM-350	350	0.04	1.5	-	-	-
MAM-150	150	0.04	1.5	9.5	54-67	150
MAM-250	250	0.04	1.5	9.5	90-112	150
MAM-350	350	0.04	1.5	6.5	86-108	150

For each turning test, the cutting was temporarily stopped at every 1.2 km cutting distance for tool wear characterization. At the end of each interval, the tool was first cleaned with ethanol in an ultrasonic cleaner, and then tool wear was observed and measured using a Nikon Eclipse LV100ND microscope and Keyence VHX6000 digital microscope. After the measurement, the turning test was resumed with the same tool for the next interval. The turning test was not resumed (fully stopped) if the measured flank wear reached more than 300 μm or the total cutting distance reached 7.2 km. The latter criterion was implemented to save the workpiece material. At the final stop of each turning test, the tool was further characterized using an Olympus FluoView 1000 confocal laser scanning microscope (CLSM) to obtain the 3D profile of the wear land of the tool [79,80]. The tool was also characterized using a JEOL 6610LV scanning electron microscope (SEM) together with energy dispersive spectroscopy (EDS) to identify the exposed or deposited materials on the wear land of the tool. These characterizations were performed both before and after removing the iron adhesion on the tool by etching with HCL (19%) for 45 minutes.

3.3 Results and discussion

Figure 28 shows the progression of the flank wear (VBmax) with cutting distance for all the tests. To facilitate comparison, the solid line indicates CM turning while the dashed line indicates MAM turning. The line color is used to distinguish the cutting speed. It clearly shows that MAM turning resulted in significantly lower wear compared to CM turning results. At Vc = 150 m/min (blue), both CM and MAM turning resulted in the desired steady-state slow wear progression to the final cutting distance of 7.2km. The final VBmax was 235 μm and 178 μm for CM and MAM turning, respectively. For CM turning at Vc = 250 m/min (red solid line), the slow wear progression transitioned to rapid wear after cutting about 2.4 km. VBmax exceeds the flank wear threshold of 300 μm after cutting 3.2 km. At Vc = 350 m/min, the rapid flank wear occurs even earlier, resulting in a very steep wear curve. VBmax exceeds 300 μm after only cutting about 2 km. In contrast, the rapid flank wear progression was not activated in MAM turning at Vc = 250 and 350 m/min. The two corresponding wear curves still show the steady state slow wear progression to the cutting distance of 7.2 km. The final VBmax was 223 and 245 μm for Vc = 250 and 350 m/min, respectively. Although the flank wear increased with cutting speed in both CM and MAM turning, the speed effect on wear is far less significant in MAM turning.

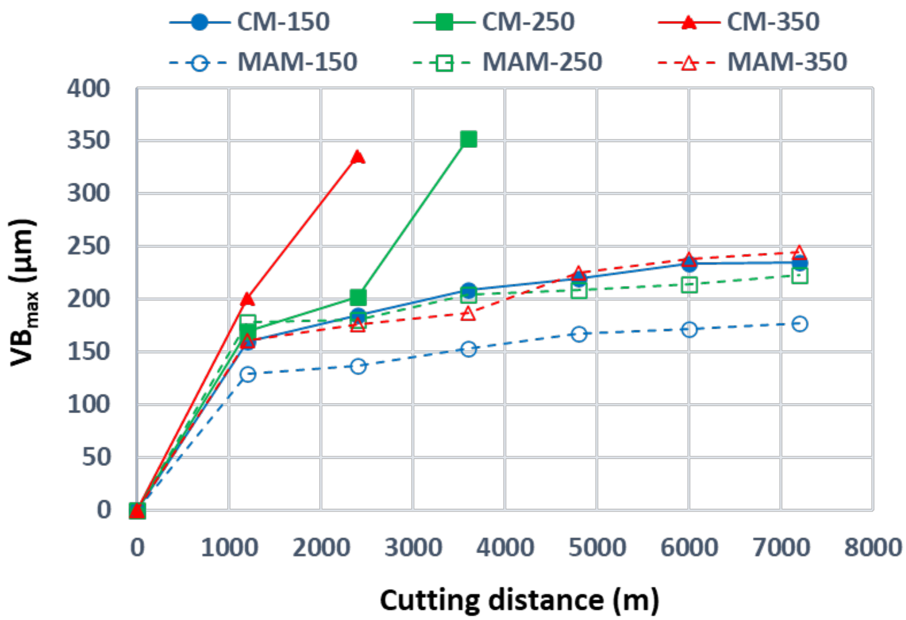

Figure 28: Progression of flank wear (VBmax) with the cutting length for all turning tests. MAM wear reduction is more remarkable at high speeds. Adapted from [77].

Figure 29 shows the selected Keyence microscope images of the tool edge after turning at 150 m/min. The coating materials in the worn area can be recognized based on the color: Al_2O_3 appears brown and TiCN appears black, which is confirmed by EDS analysis. In both CM and MAM turning after 1.2 km cutting, a uniform wear land is observed along the cutting edge on both the flank and rake faces. The worn surface on the rake face is larger in MAM than in CM turning. This is because the uncut chip thickness is up to 2 times larger in MAM (Figure 17b) resulting in larger tool chip contact on the rake face. However, the flank wear land is clearly smaller in MAM. As cutting distance increased to 7.2 km, the flank wear land grew uniformly along the cutting edge in CM turning but nonuniformly in MAM turning. In MAM, the flank wear land grew mainly on the tool nose and near the end of the side cutting edge. From the etched tool image, the coating was breached for the upper portion of the flank wear land in these regions. The material covering the breached area on the unetched tool is identified as iron. In contrast, the breach of tool coating is not observed in CM turning. However, the cutting edge remains very sharp in MAM turning while it appears to be dull in CM turning.

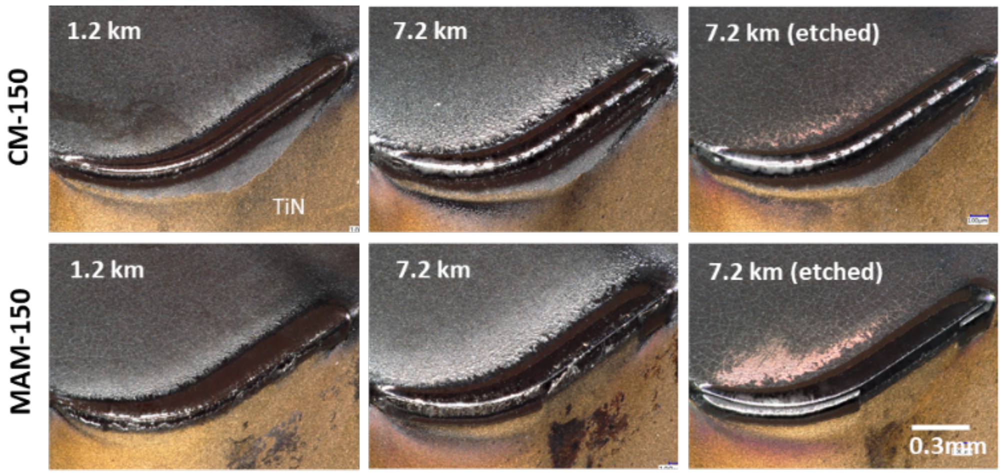

Figure 29: Keyence digital microscope images of tool edge after turning at Vc = 150 m/min. Wear reduction is not significant however MAM preserves edge sharpness. Adapted from [77].

Figure 30 shows the selected images of the tool edge after turning at Vc = 250 m/min. In CM turning, the wear did not breach the tool coating at the cutting distance of 2.4 km based on the fact that no iron adhesion is observed on the tool. However, when reaching the cutting distance of 3.6 km, substantial iron adhesion is observed in a large area of the main flank wear land. The etched tool image shows the actual tool wear in this area is quite deep into the substrate Tungsten Carbide (WC). At the same cutting distance (3.6 km) with MAM turning, no accumulation of iron on the tool is observed, and tool coating has not been breached. At the cutting distance of 7.2 km, mild iron adhesion can be observed on the flank wear land. The etched tool image shows that the tool coating is breached on the flank wear land mainly on the tool nose area and near the end of the side cutting edge, which is in contrast to the case in CM turning. Furthermore, the side cutting edge in MAM is still very sharp after cutting 7.2 km while it is destroyed in CM turning after cutting 3.6 km.

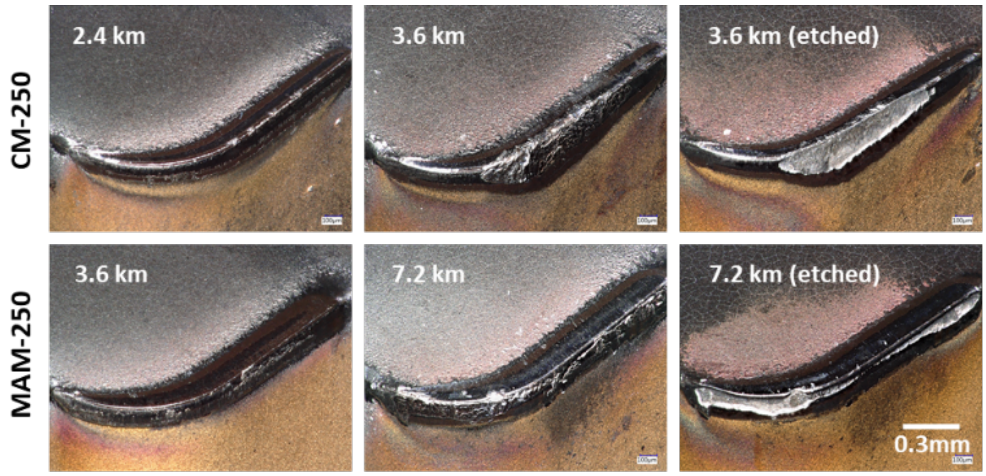

Figure 30: Keyence digital microscope images of tool edge after turning at Vc = 250 m/min. MAM significantly increases tool life while preserving edge. Adapted from [77].

Figure 31 shows the selected images of the tool edge after turning at Vc = 350 m/min. At this speed, substantial iron adhesion is observed after reaching the cutting distance of 2.4 km in CM turning. The iron adhesion is spread along the whole cutting edge on the flank wear land. From the etched tool image, the actual wear beneath the iron adhesion breached the tool coating, exposing the WC substrate. In contrast, after reaching the cutting distance of 2.4 km in MAM turning, neither significant iron adhesion nor coating breach is observed on the flank wear land. Significant iron adhesion is observed on the flank after reaching the cutting distance of 7.2 km. The corresponding wear land with the coating breached is more uniformly distributed along the cutting edge. The area of the coating-breached wear land is narrower in MAM turning at the cutting distance of 7.2 km than in CM turning at the cutting distance of 2.4 km. Furthermore, the cutting edge appears much sharper in MAM than in CM turning.

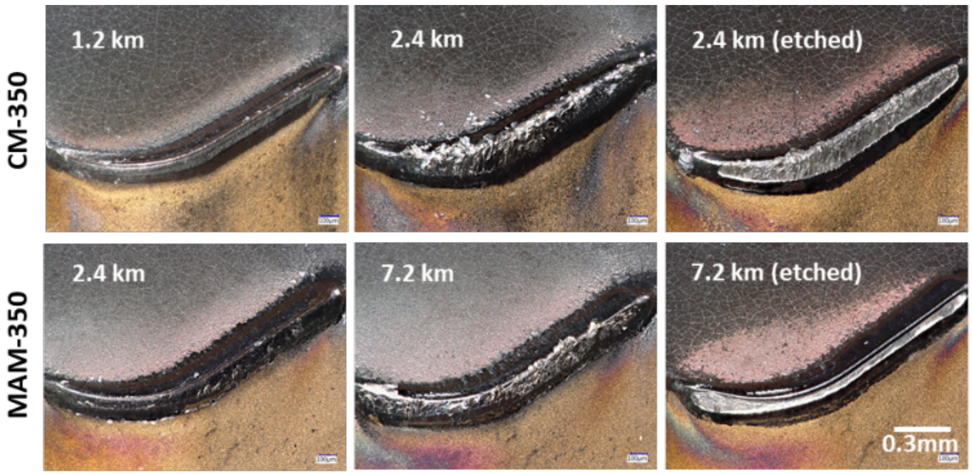

Figure 31: Keyence digital microscope images of tool edge after turning at Vc = 350 m/min. Adapted from [77].

Figure 32 shows the section profiles of the flank wear land of the final etched tools in Figure 31 and Figure 32. The profiles are measured by CLSM. At each section plane, three profiles are superimposed for comparison, including the new tool profile (gray), MAM profile (blue) and CM profile (orange). The four section planes (section 1, 2, 3 and 4) are normal to the side cutting edge and located at 0.66, 0.94, 1.22 and 1.5 mm, respectively, from the minor cutting edge. It is evident that the flank wear land resulting from MAM turning is significantly smaller not only in width (vertical direction) but also in depth (horizontal direction). This indicates that the wear reduction by MAM is more significant should the wear volume be compared. Figure 33 shows the calculated wear volume on the flank wear land based on the 3D profile measurements. At Vc = 150 m/min, the wear volume is generally low in both CM and MAM turning, despite the slightly higher value in MAM turning. At higher speeds, the wear volume increases substantially in CM turning but moderately in MAM turning. Therefore, the wear volume is significantly lower in MAM than in CM turning at the higher speeds. It should be noted that the tools in MAM after cutting 7.2 km are compared to the tools in CM turning after cutting a much short distance (3.6 or 2.4 km) at the higher speeds. Therefore, the wear reduction in MAM is quite remarkable at higher cutting speeds.

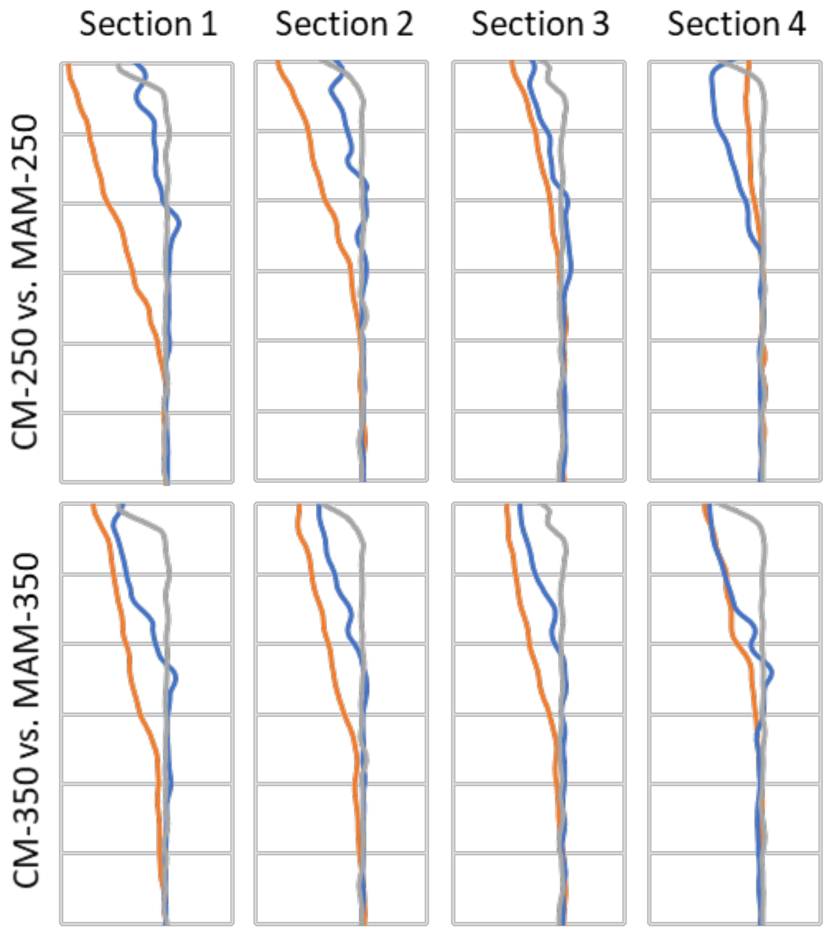

Figure 32: Section profiles of the main flank wear land of the final etched tool in CM and MAM turning at Vc = 250 and 350 m/min. Gray profile is for new tool, blue for MAM, and orange for CM. The four section planes from left to right are located at 0.66, 0.94, 1.22 and 1.5 mm from the minor cutting edge. MAM also reduces the depth of wear. Adapted from [77].

Figure 34 shows the cutting force history for the first three cutting intervals of the turning tests at the higher speeds. Note that each cutting interval has the cutting length of 1.2 km. Note also, the forces which appear as force bands in these plots are always oscillating due to the applied tool vibration in MAM turning. The observed force changes in these plots reflect the tool wear effects on cutting forces. For example, the force changes are observed in the initial period of the first cutting interval for all turning tests. This should be due to the initial wear development on a new tool while establishing the stable contact between tool and workpiece.

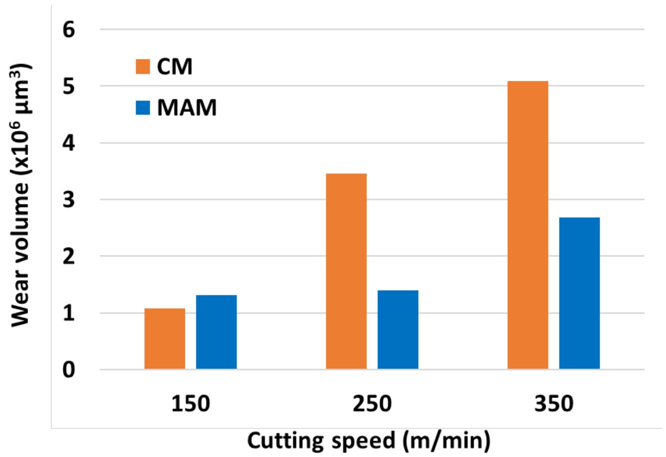

Figure 33: Wear volume for the main flank wear land of the etched tools. MAM reduces wear volume specially at high speeds. Adapted from [77].

In CM turning, the initial tool wear leads to the initial increase and the subsequent decrease in forces while in MAM turning the initial tool wear leads to the continuous increase in forces. These changes are more evident on the feed force (blue) than the primary cutting force (red). In the third interval of CM turning at Vc = 250 m/min and the second interval of CM turning at Vc = 350 m/min, the significant increase in forces, in particular the feed force, can be observed. This can be attributed to the rapid tool wear progression and severe tool adhesion occurring during those intervals (see Figures 28, 30 and 31). The other cutting intervals show approximately the constant or the steady state forces which correspond to the mild steady state wear progression in those cutting intervals.

To further compare the cutting forces in all the tests, the primary cutting force and the feed force are both averaged over each cutting interval (i.e., over 1.2 km cutting length). Figure 35 plots the averaged forces versus the intervals for all the tests. Note the resemblance of these force curves to the wear curves in Figure 28. These force curves again reflect the influence of tool wear on the cutting forces. It is evident that the tool wear has a much greater influence on the feed force than the primary cutting force because the major wear is the flank wear.

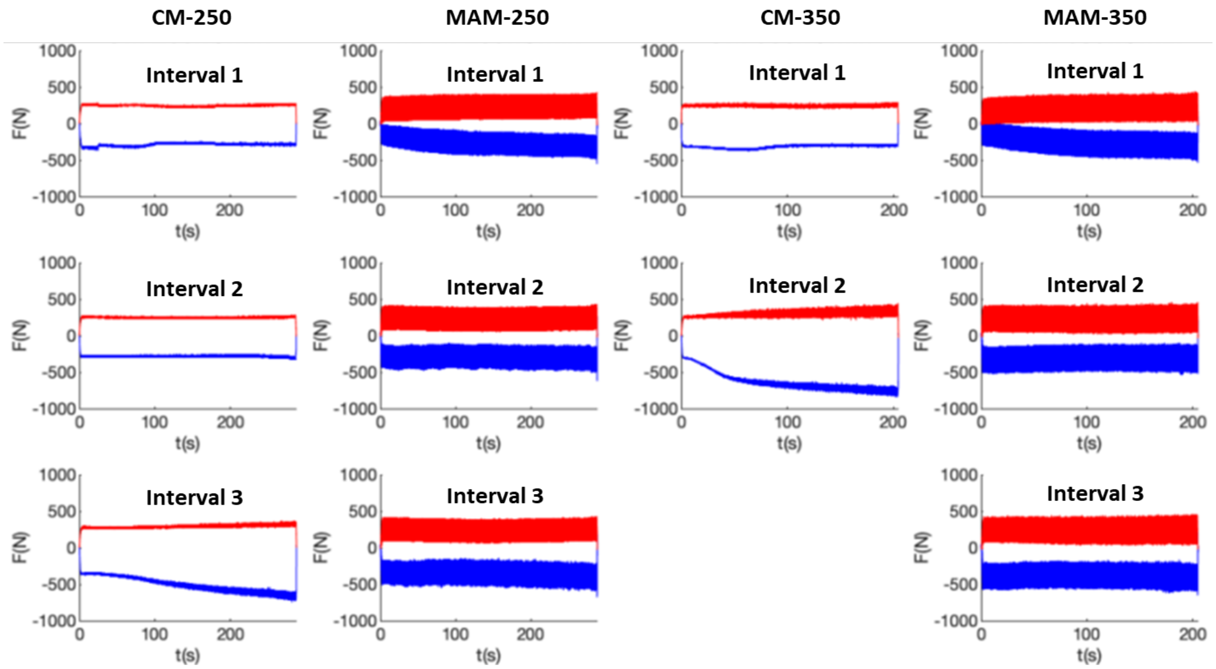

Figure 34: Primary cutting force (red) and feed force (blue) histories for the first three cutting passes of the turning tests at Vc = 250 and 350 m/min. Severe force increase correlates with tool failure in CM, while in MAM it indicates slow wear rate. Adapted from [77].

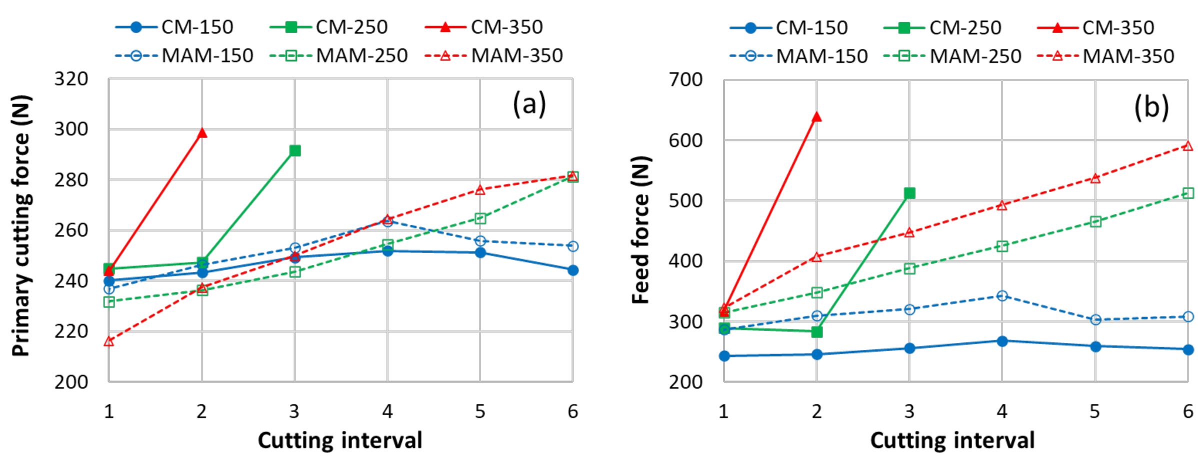

Figure 35: (a) Averaged primary cutting force and (b) feed force over each cutting pass. Cutting force is controlled by wear but also by adhesion for both MAM and CM. Adapted from [77].

The total area of the flank wear land is equivalent to the tool-work contact area and thus it directly affects the feed force. Also, the amount of adhesion should play an important role in affecting the forces. For example, the flank wear land area appears to be roughly the same for CM-

150, MAM-250, and MAM-350 (Figure 29-Figure 31), but the respective feed force shown in Figure 35b is quite different because the severity of tool adhesion in each case is quite different. No adhesion is observed at the cutting distance of 7.2 km in CM-150 (Figure 29) while adhesion is clearly observed at the same cutting distance in both MAM-250 (Figure 30) and MAM-350 (Figure 31). It is also evident the adhesion is more severe in MAM-350 than in MAM-250 based on both unetched and etched tool images. Note the coating breached area after etching is equivalent to the adhesion covered area before etching. From these observations, the ranking of the feed force matches the ranking of the severity of adhesion in the three tests.

Figure 36 shows the tool temperature history in the first cutting interval of each turning case. Note the tool temperature is measured at a fixed location on the rake face that is 0.83 mm from the side cutting edge and 2.5 mm from the end cutting edge (see the inset of Figure 27). In all cases, the tool temperature increases very rapidly during the first few seconds after the cutting starts. The rate at which the temperature increase gradually decreases; the rate appears to approach a nearly constant value at which the temperature increases slowly and steadily. Since the cutting length of each interval is the same, the higher cutting speed results in the shorter temperature history curve. By comparing these curves, it is evident the tool temperature increases with the cutting speed in both CM and MAM turning. At Vc = 150 m/min, the tool temperature is slightly higher in MAM than in CM turning. However, at higher speeds, the tool temperature is significantly lower in MAM than in CM turning. Therefore, the reduction in temperature by MAM turning is more effective at the higher cutting speeds.

Figure 37 shows the tool temperature history in all cutting intervals for CM and MAM turning at Vc = 350 m/min. In general, all these temperature curves show the same trend, i.e., an initial rapid increase in temperature smoothly transitioned to a steady state increase in temperature with a lower rate.

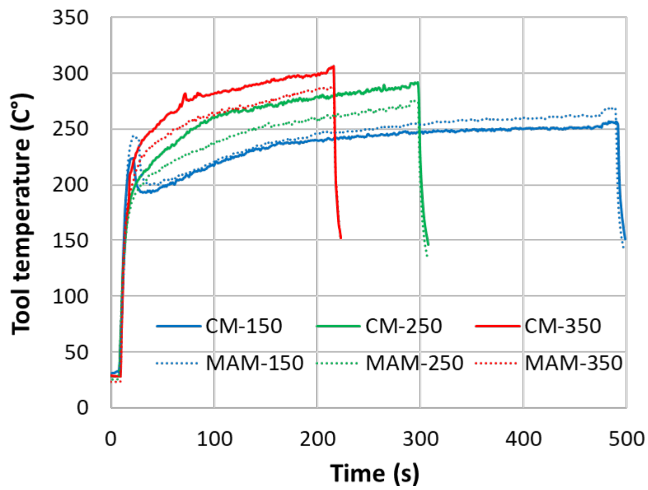

Figure 36: The tool temperature history during the first cutting interval of each test. See measurement setup in Figure 27.MAM reduces tool temperature only at high cutting speed. Adapted from [77].

The changes in the temperature from one interval to another should reflect the tool wear effect on the cutting temperature. In CM turning, the temperature curve for the second interval is significantly higher than the curve for the first interval, which is due to the rapid tool wear and severe adhesion occurring during the second interval. In MAM turning, the temperature curve is elevated in general from one interval to another. However, the temperature curve even for the sixth interval in MAM turning is still not higher than the temperature curve for the first interval in CM turning. This slow temperature elevation with cutting interval can be attributed to the mild wear progression in MAM turning. More careful observation reveals that the temperature elevation from one interval to another is not uniform in MAM turning. The temperature curve for the second interval has a significantly lower ramp in the steady state region which leads to the temperature reduction eventually compared to the first interval. The temperature curve for the third interval is elevated higher than the curve for the first interval. The temperature curve for the fourth interval is not significantly elevated from the third interval. The temperature curve for the fifth interval is elevated again while the temperature curve for the sixth is not significantly elevated from the fifth interval.

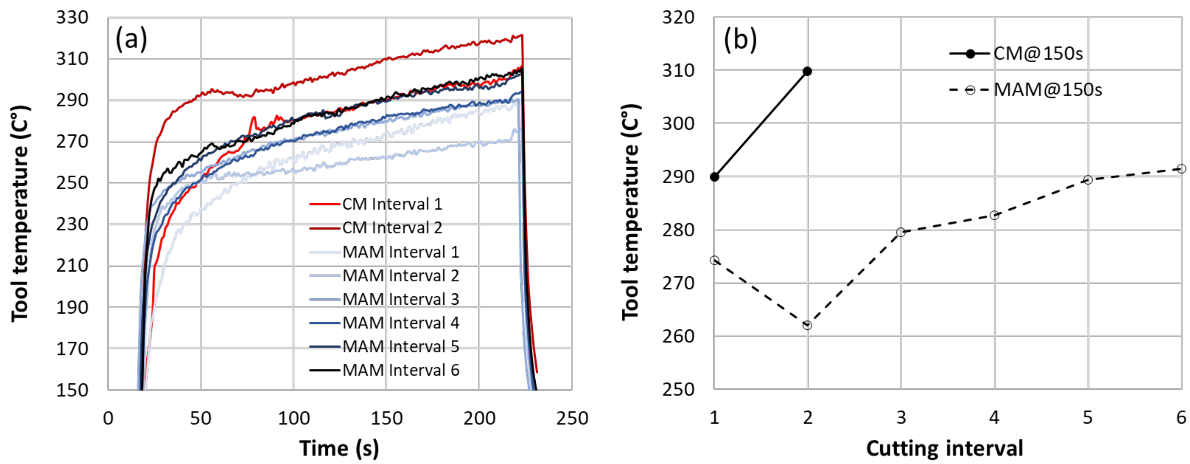

Figure 37: (a) Tool temperature history during each cutting interval in CM and MAM turning at Vc = 350 m/min. (b) The temperature value at t = 150 s in each temperature history curve in (a). The temperature in MAM is always below the temperature of CM. Adapted from [77].

Both curves from the fifth and the sixth intervals nearly overlap with the curve for the first interval in CM turning in the steady state region. The value of each temperature history curve at the cutting time of 150 s (which is in the steady state region) is used as a representative temperature for each corresponding cutting interval. Figure 37b plots the representative temperature versus the cutting interval. It is again evident that MAM turning results in lower tool temperature, and the increase in tool temperature with cutting interval is also more gradual in MAM than in CM turning.

3.4 Conclusions

In this study, a new MAM turning setup was implemented to conduct longitudinal turning experiments. Tool wear, cutting forces and temperature are experimentally characterized in CM and MAM turning at three cutting speeds (150, 250 and 350 m/min). The findings of this study can be summarized as follows.

The primary wear in cutting CGI with coated carbide tools is the flank wear in both CM and MAM turning. The flank wear is not reduced by MAM at the low cutting speed (150 m/min). However, at the higher cutting speeds (250 and 350 m/min), the flank wear is significantly lower in MAM than in CM turning, and the reduction in tool wear by MAM is even more significant when measured by wear volume.

Severe iron adhesion occurs when the tool coating is breached, which leads to the rapid wear in CM turning at the higher speeds (250 and 350 m/min). In CM turning, the breach of tool coating accompanied by severe iron adhesion tends to start in the middle region of the side cutting edge and rapidly spreads toward the nose region and the end region of side cutting edge.

The breach of coating with iron adhesion also occurs in MAM turning. However, it tends to start separately on the tool nose region and the end region of the side cutting edge, and then spread gradually toward the middle region of the side cutting edge. Increasing the cutting speed will accelerate this wear process, but the speed effect is far less significant in MAM than in CM turning. As a result, the reduction in wear by MAM is most effective at the higher cutting speeds.

The increase in the flank wear leads to the increase in both the primary cutting force and the feed force. However, the wear effect is much more significant on the feed force than the primary cutting force, which is consistent with the fact that the dominant wear is the flank wear. Besides the size of the flank wear land, the severity of the adhesion also contributes to the wear effect on the forces.

Tool temperature is significantly lower in MAM than in CM turning at the higher cutting speeds, but slightly higher at the low cutting speed, which agrees with the wear comparison in MAM and CM turning at the low and higher speeds. This indicates the close relationship between the wear and the temperature.

CHAPTER 4: WEAR MECHANISM WHEN MACHINING COMPACTED GRAPHITE IRON WITH COATED CARBIDE TOOLS

4.1 Summary

The previous chapter demonstrated that MAM has the potential of reducing the wear in dry longitudinal turning of CGI with coated carbide tools, specially at high cutting speeds. This chapter focuses on understanding the mechanisms behind the machinability improvement of turning CGI under MAM with coated carbide tools. Tool wear evolution is characterized in detail after turning CGI under conventional machining and MAM in the dry and lubricated conditions at the cutting speed of 250 m/min. There are significant wear reductions with MAM turning compared to CM turning. Moreover, MAM dry turning leads to less wear than MAM lubricated turning. Two wear phenomena account for the wear reduction in MAM: 1) the formation of SiO_2 deposition layer on tool flank and 2) the preservation of the coatings on the cutting edge. The mechanisms on how the wear progression is slowed down by the observed wear phenomena as well as how these phenomena are enabled by MAM are discussed. Although this study is limited to cutting CGI, the same mechanisms observed in MAM may be also effective for improving the machinability of other difficult-to-cut materials.

4.2 Materials and methods

Figure 2 shows the MAM turning setup used in this study. The setup was implemented on a Haas TL-1 toolroom lathe. The tool vibration device consists of a stationary frame (1), two linear guides (2), a moving stage (3), and a piezo stack actuator (4). The tool holder is fixed to the moving stage supported by two linear guides. The rails of the linear guides are fixed to the stationary frame. The linear guides constrain the tool motion to only in the tool feed direction. Tool vibration is generated by the piezo stack actuator. The casing of the actuator is fixed to the stationary frame and its actuating head is connected to the moving stage. The piezo stack actuator has a nominal stroke of 0.1 mm, which can generate a maximum driving force of 4000 N. The frequency and amplitude of the tool vibration are controlled by a sinusoidal voltage input to the actuator. The driving voltage is provided by a waveform generator (BK4007B) and a power amplifier (MMech PX200). To measure cutting forces, the tool vibration device is mounted onto a Kistler dynamometer plate (9257B) which is fixed onto the carriage of the lathe. The force signal is recorded using a data acquisition system with a sampling rate of 5000/s and processed with a low-pass filter with a cutoff frequency at 500 Hz.

The CGI workpieces (SinterCast AB) has a hollow cylinder shape with an outer diameter of 145 mm and inner diameter of 98 mm, and a length of 204 mm. The grade is GJV-450 by ISO standard 16112:2017 with a tensile strength of 450 MPa. The iron matrix is mainly pearlite (95%). The cutting inserts are multi-layer coated carbides (Sandvik Coromant SNMA 12 04 08- KR 3205), with a two-layer coating (TiCN / Al2O3) on the rake face and three-layer coating (TiCN / Al2O3 / TiN) on the flank face. The toolholder is Sandvik DSBNR 2020K. When used together, it results in a side cutting edge angle of 15° and a rake angle of -6°. For lubricated cutting, the applied cutting fluid is Coolube 2210 (UNIST) which consists of pure vegetable oil recommended for minimum quantity lubrication (MQL) machining ferrous materials. The fluid is delivered to the cutting zone as continuous stream at a flow rate of 1.7 ml/s through a nozzle placed above the tool rake face.

Table 1 lists all the turning tests reported in this study. Each test is performed with a new tool. The cutting speed (Vc = 250 m/min), feed rate (ho = 0.04 mm/rev) and the depth of cut (d = 1.5 mm) are kept the same for all tests. The main controlled variables are the tool modulation condition (CM vs. MAM) and the cutting fluid condition (dry vs. lubricated). For MAM turning, the frequency ratio is set to fm/fw = 9.5, so the wave tool path has a phase of $\varphi = \pi$ (see Fig. 1b) and the tool disengages from the workpiece 9.5 times per revolution.

Since the rotation frequency (fw) varies with the diameter of the workpiece to maintain a constant cutting speed, the vibration frequency (fm) will also be varied accordingly (within 90 – 112 Hz) to maintain the constant frequency ratio. The driving voltage peak-to-peak amplitude is set to Vpp = 150 V which results in a peak-to-peak tool vibration amplitude (2A) of ~90 μm measured at the no-cutting condition.

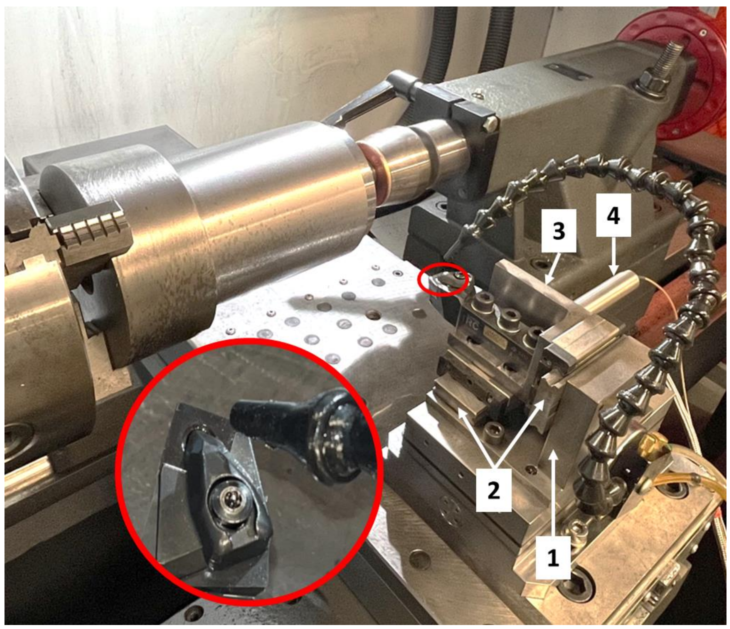

Figure 38: MAM turning setup. Adapted from [81].

To measure tool wear, each turning test consisted of several cutting intervals. For most cases, each cutting interval has 1.2 km cutting length. After each cutting interval, the tool was cleaned with ethanol in an ultrasonic cleaner. Tool wear was then observed and measured using a Nikon eclipse LV100ND microscope and / or a Keyence VHX6000 digital microscope. Then, the test was resumed with the same tool for the next cutting interval. At the final cutting distance, the tool was characterized more comprehensively before and after etching with HCL (19%) for 45 minutes to remove adhesion. The 3D topography and 2D section profiles of the wear land were measured using Keyence VHX6000 digital microscope at high resolutions. The compositions of the materials present at the wear land are measured using a JEOL 6610LV scanning electron microscope (SEM) equipped with energy dispersive spectroscopy (EDS).

Table 4: List of turning tests reported in this study. Adapted from [81].

Tool Number	Turning condition	Total cutting distance
1	CM-dry	3.6 km
2	CM-lubricated	4.8 km
3	MAM-dry	7.2 km
4	MAM-lubricated	7.2 km
5	CM-dry	2.4 km
6	CM-lubricated	2.4 km
7	MAM-dry	2.4 km
8	MAM-lubricated	2.4 km
9	MAM-dry	3.6 km
10	MAM-dry	5.0 km

4.3 Results and Discussion

4.3.1 General observation on tool wear and forces

Figure 39 shows the optical images of the tool main flank face after every cutting interval (1.2 km) for each turning condition. The progression of the flank wear (VBmax) with the cutting distance measured based on these images is shown in Figure 40. It is evident that the progression of flank wear is significantly slower in MAM than CM regardless of the lubrication condition. In CM turning, the flank wear started to progress rapidly after cutting only a short distance which is evidenced by the sharp upturn of the wear curve at 2.4 km cutting distance for the CM-dry case and 3.6 km cutting distance for the CM-lubricated case (Figure 40). The rapid wear progression is accompanied by the occurrence of severe adhesion on the tool for both CM cases (see arrows 1 and 2 in Fig. 3).

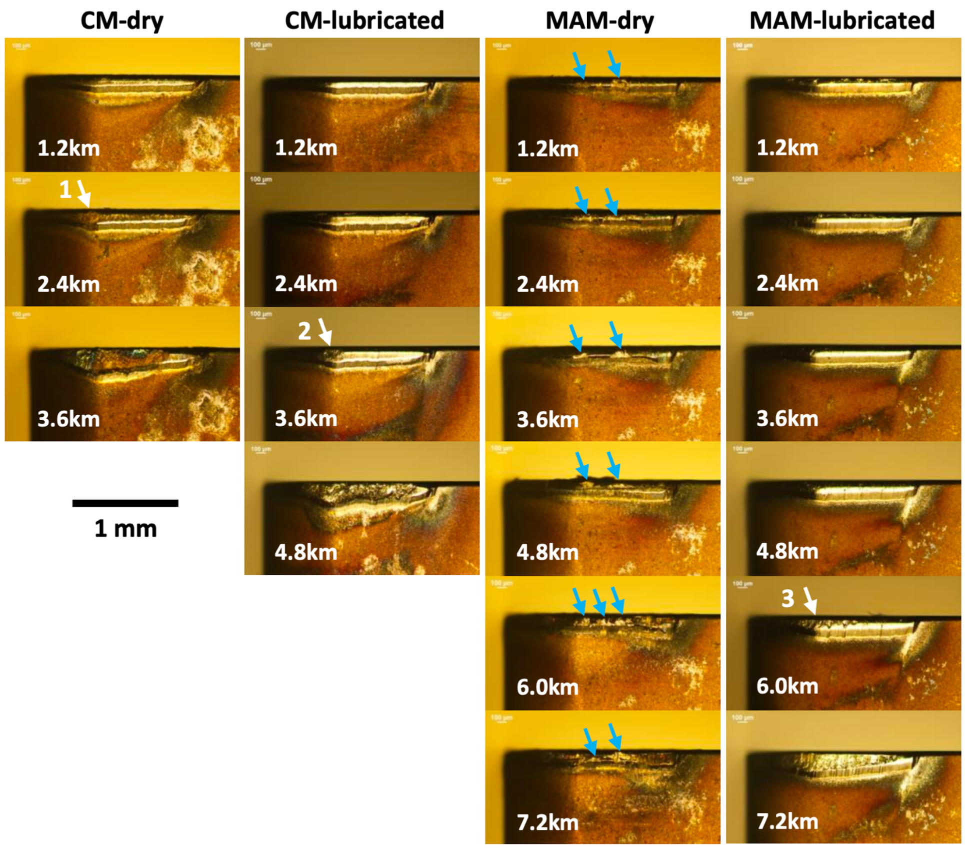

Figure 39: Optical images of tool flank wear after every cutting interval (1.2 km) for each turning condition. Tool number: 1, 2, 3 and 4. Adapted from [81].

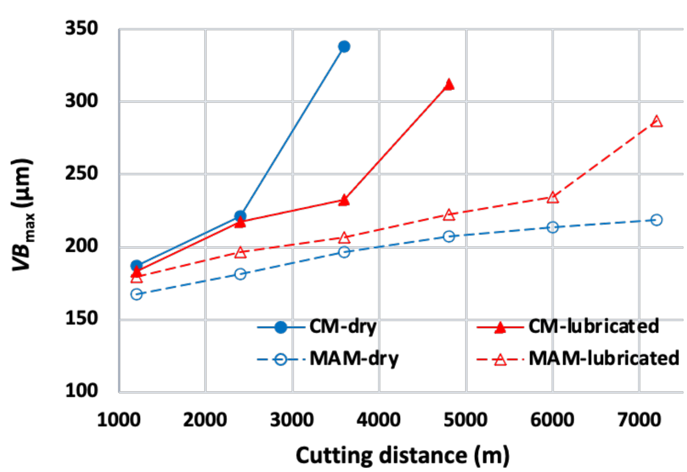

Figure 40: The progression of VBmax with cutting distance for different turning conditions. Adapted from [81].

It appears that the application of cutting oil reduced tool wear in CM turning by delaying the start of the rapid wear progression associated with severe adhesion. However, the cutting oil appears to have no effect in mitigating the severe adhesion once it started, and hence had no effect in slowing the rapid wear progression. Once the rapid wear progression started, the flank wear quickly increased beyond 300 μm which is commonly used as the criterion for the end of tool life.

In contrast to CM turning, the progression of flank wear in MAM turning remains steady at a low wear rate up to a much longer cutting distance. For the MAM-lubricated case, a noticeable increase in the wear rate occurs after the cutting distance reached 6 km (Figure 40). This is again accompanied by the occurrence of severe adhesion (see arrow 3 in Figure 39). Surprisingly, the MAM-dry case resulted in the lowest wear. The wear curve for MAM-lubricated case is always above the curve for MAM-dry case which even has a slight decrease in wear rate toward the end of the curve. At 7.2 km cutting distance, the measured VBmax is 219 and 287 μm for MAM-dry and MAM-lubricated case, respectively. The wear in MAM-lubricated case is about 30% higher than the wear in MAM-dry case.

The adhesion occurred in MAM-dry case is unique (see Figure 39). For the other three cases, the initiation of severe tool adhesion can be clearly identified at a particular cutting distance (see arrows 1, 2 and 3 in Figure 39), and the wear progression can be divided into two distinctive stages: 1) the steady wear without adhesion and 2) the rapid wear accompanied by severe adhesion. For MAM- dry case, tool adhesion starts to occur right from the beginning and increases more gradually throughout the test (see blue arrows in Figure 39). The adhesion appears to be more loosely attached to the tool and its distribution on the tool is not as continuous as in the other three cases. More importantly, the adhesion in MAM-dry case is not associated with rapid wear progression.

Figure 41 shows the history of the cutting forces during each cutting interval (cutting distance of every 1.2 km) for the four turning cases. The corresponding average forces over each interval are plotted in Figure 42.

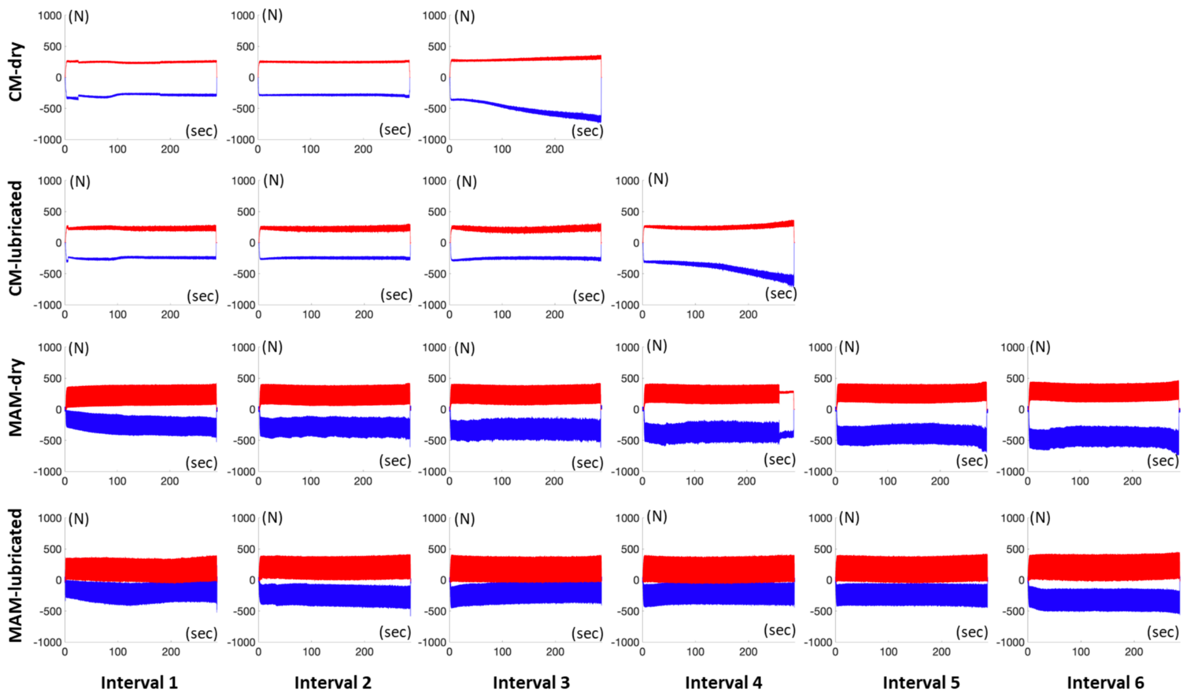

Figure 41: The time history of cutting force (red) and feed force (blue) during each cutting interval for the tools shown in Figure 39. Adapted from [81].

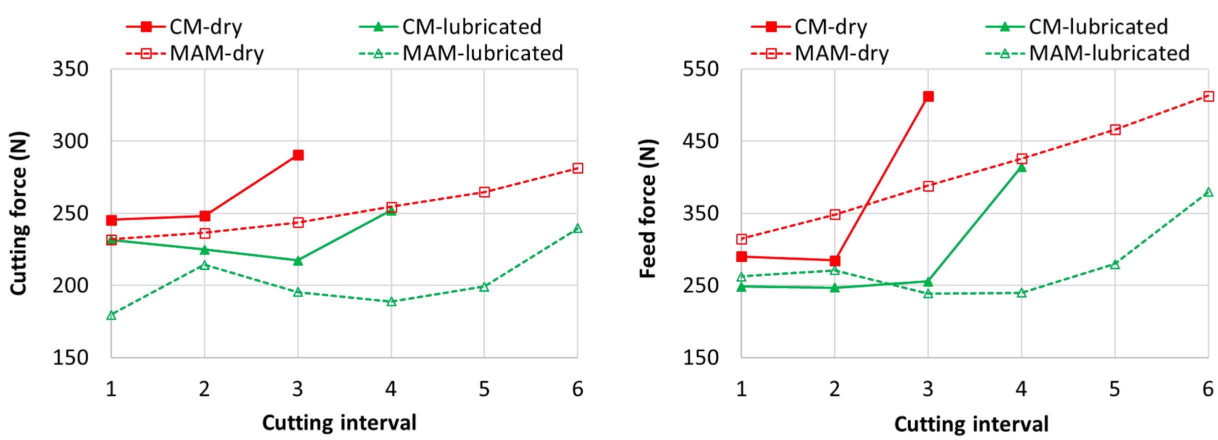

Figure 42: The averaged cutting force (a) and feed force (b) for each cutting interval corresponding to Figure 41. Adapted from [81].

The changes in forces with increasing cutting distance (or at each cutting interval) should reflect the tool wear or tool adhesion effect. For all cases, the feed force is more sensitive than the cutting force because the wear and adhesion mainly occur on the tool flank face. For both CM-dry and CM-lubricated cases, the rapid increase in forces in the last cutting interval corresponds to the rapid wear and severe adhesion occurring in that interval (see Figure 39). In MAM, the forces always oscillate due to the tool vibration, so the forces appear as the bands in the history plots (Figure 41). For MAM-dry case, the forces generally remain steady during each cutting interval, but there is a clear trend that the forces increase steadily from one interval to the next interval throughout the test. This corresponds to the occurrence of adhesion right from the beginning in MAM-dry case (see blue arrows Figure 39). For the MAM-lubricated case, the forces have similar trends as those in CM-dry and CM-lubricated cases. In other words, the forces do not change significantly before the occurrence of severe adhesion. The significant increase in forces in the last cutting interval corresponds to the rapid wear accompanied by severe adhesion. It is evident that the increase in the forces is mainly caused by tool adhesion in all three cases.

Figure 43 shows Keyence digital microscope images of the tools at the final cutting distance before and after etching for the four turning cases. Significant adhesion is clearly seen covering the tool flank in all cases. The adhesion is identified to be mainly iron (i.e., the work material) based on EDS analysis. The etched tool images reveal the actual tool wear in the adhesion region: the tool coating is completely breached, and the carbide substrate is exposed which is also confirmed by EDS analysis. Generally, the coating breached region matches well with the adhesion region. In both CM-dry and CM-lubricated cases, the breached region is primarily on the main flank and slightly extends to the nose flank. In MAM-lubricated case, the breached region is located continuously from the nose flank to the main flank. In MAM-dry case, the breached region is however separated on the nose flank and at the end of the main flank (i.e., away from the nose); the coating in the middle of the main flank is barely breached as shown in Figure 43.

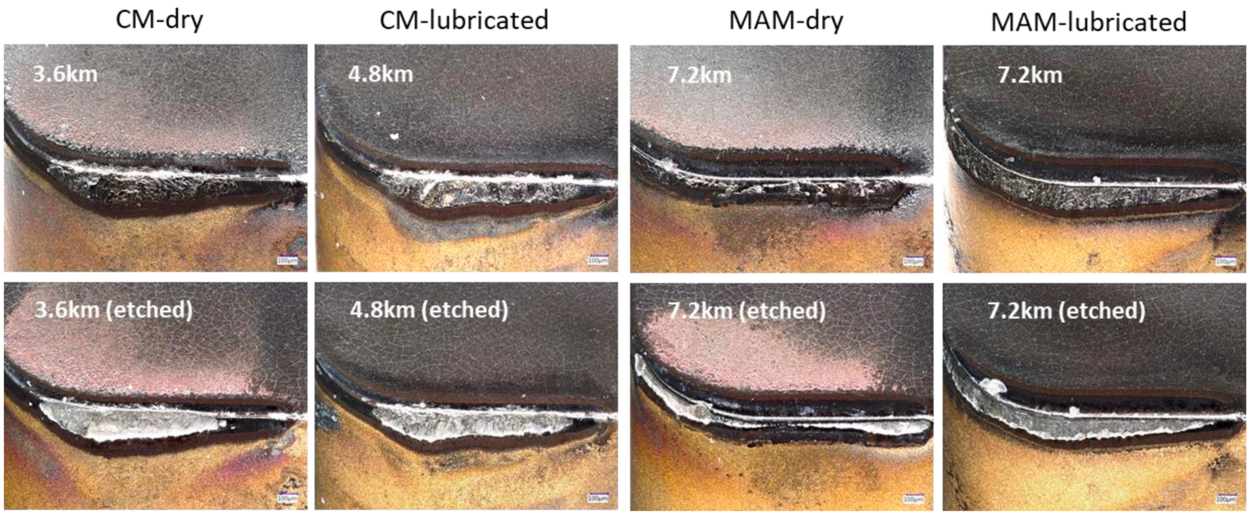

Figure 43: Unetched (top) and etched (bottom) tool images for each turning condition at the final cutting distance. Tool number: 1, 2, 3 and 4. Adapted from [81].

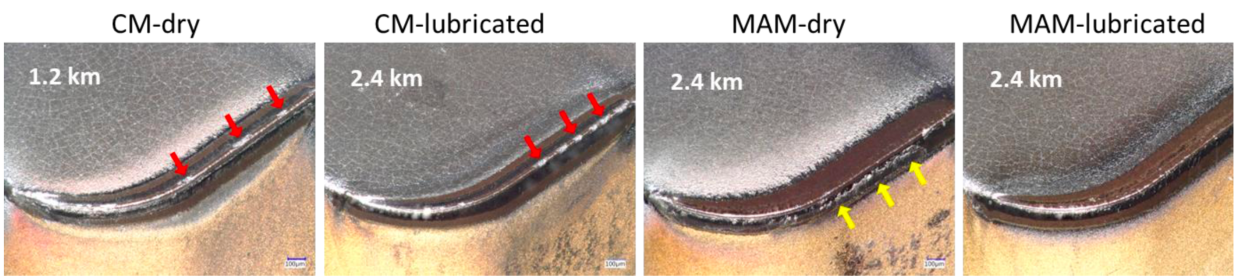

Figure 44: Unetched tool images for each turning condition before tool coating is breached. Tool number: 5, 6, 7 and 8. Adapted from [81].

The total breached area in MAM-dry case is the smallest among all cases. In addition, the breached region does not match with the adhesion region as clearly as in the other cases; the adhesion appears to also occur in the middle region of the main flank where coating has not been breached.

Figure 44 shows the tools after the first or second cutting intervals where coating has not been breached for the four cases. Some damage is observed on the cutting edge in both CM- dry and CM-lubricated cases (see red arrows). In contrast, no such damages occur on the cutting edge in MAM-dry and MAM-lubricated cases. A significant amount of adhesion is also observed on the tool flank in the MAM-dry case (see yellow arrows) while the tool flank appears much cleaner in the other cases. This is consistent with the observations in Figure 39.

From these observations, it is now clear that there are two types of adhesion occurring in MAM-dry case: the adhesion on the coating and the adhesion on the exposed carbide once the coating is breached. For the other cases, the adhesion only occurs on the exposed carbide after coating is breached. In other words, the initiation of adhesion does not occur until the coating on the tool is breached.

4.3.2 Wear characteristics in dry conditions

Figure 45 shows a detailed comparison of the tools after etching in CM-dry and MAM-dry cases. There are several notable distinctions. First, in the CM-dry case, the coating breach occurs very early (at the cutting distance of 2.4 km).

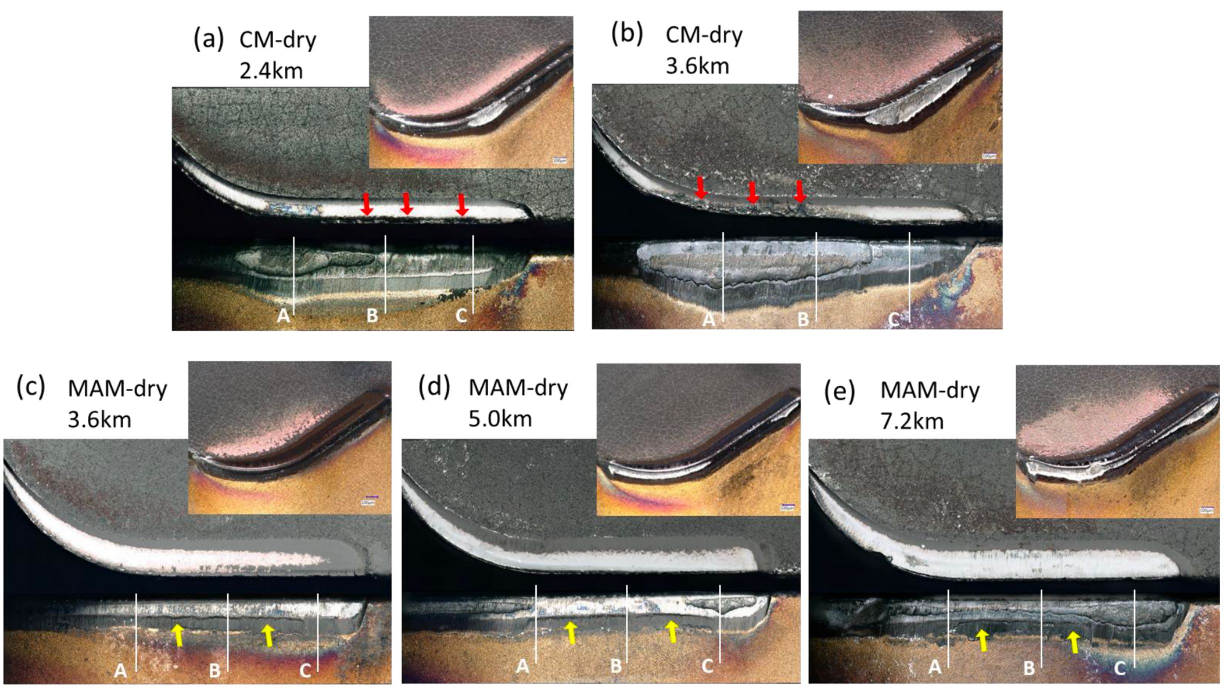

Figure 45: Digital microscope images of etched tools with different cutting distances in CM-dry (top row) and MAM-dry (bottom row) turning tests. Tool number: 5, 1, 9 and 10. Wear morphology is different in MAM as compared to CM. Adapted from [81].

The breach on the tool flank starts in the middle region along the cutting edge (Figure 45a) and grows rapidly on the main flank along the side cutting edge (edge from lines A-B in Figure 45b). In MAM-dry case, coating breach starts from two ends of the tool flank. i.e., the nose flank and the end of the main flank (Figure 45d). The expansion of the two breached zones into the middle region is quite slow. At the cutting distance of 7.2 km (Figure 45e), the breached zone in the middle region only appears as a barely connected slit running parallel to the cutting edge at the center of the wear land. Secondly, in CM-dry case, the breached zone extends over the cutting edge. The cutting edge outside the breached zone also shows much damage as micro-chipping (red arrows in Figure 45a). Furthermore, the rake face next to the breached cutting edge shows the burned colors indicating a higher temperature in this region. As the breached zone increases in size, the rake face coating near the breached edge also shows much damage leading to a very rough rake face (red arrows in Figure 45b). In MAM-dry case, coating breach is limited only on the flank face. The breach does not extend to the cutting edge. The cutting edge remains well preserved without any chipping damage both before and after the coating is breached on the flank face. The rake face coating is also preserved well. The rake face shows no burned colors and appears very smooth. Thirdly, in the MAM-dry case, a thick layer of material which forms a noticeable geometric step on the flank wear land can be observed at all cutting distances (see yellow arrows in Figure 45c-e). The same layer and step cannot be clearly observed on the tools in CM-dry case.

Figure 46 shows the section profiles of the flank wear lands of the etched tools shown in Figure 45. For each tool, the gray, orange, and blue profiles are corresponding to the section locations A, B, and C marked in Figure 45, respectively. These profiles further confirm the significantly different wear characteristics in CM-dry and MAM-dry cases. In the CM-dry case, both the height and depth of the flank wear (measured in directions parallel and perpendicular to the flank face respectively) increased rapidly and became substantially high after the coating was breached (Figure 46a and b).

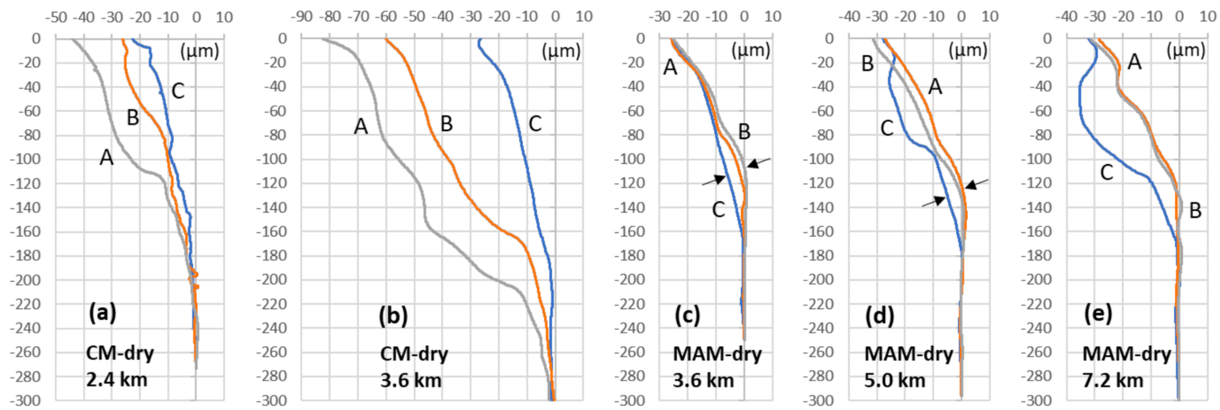

Figure 46: Section profiles of the flank wear lands of the etched tools shown in Figure 45. The three section planes (A, B and C) for each tool are marked in Figure 45. The gray, orange, and blue profiles correspond to sections A, B, and C, respectively. Adapted from [81].

The maximum flank wear depth is always seen at the cutting edge (the top side of the curve). In contrast, in the MAM-dry case, both the height and depth of the flank wear increased at a much lower rate. Note the drastic difference in the profiles between CM-dry and MAM-dry cases after cutting the same distance of 3.6 km (Figure 46b and c). In the MAM-dry case, the profiles at the coating breached zone show a concave shape or valley below the cutting edge (see blue profiles in Figure 46d and e). This again indicates the breach does not occur at the cutting edge. At the cutting distance of 7.2 km, the maximum flank wear depth is no longer at the cutting edge but at the valley of the breached zone (see blue profile in Figure 46e). The flank wear depth at the cutting edge increases very slowly in MAM-dry case, i.e., increasing only from ~ 25 μm to ~ 30 μm when cutting distance is increased from 3.6 km to 7.2 km (Figure 46c-e). In contrast, in the CM-dry case, this depth value increases from ~ 25 μm up to ~ 80 μm when cutting distance only increased from 2.4 km to 3.6 km (Figure 46a and b).

Furthermore, the distinctive layer and step observed on the flank wear land in MAM-dry case (yellow arrows in Figure 45c-e) are also noted on the corresponding profiles (Figure 46c-e). For example, in Figure 46c, the gray and orange profiles show a convex shape between -80 µm and -160 µm in y-axis where the blue profile remains straight. This is because the layer exists at section location A and B but not at location C (Figure 45c). Similar observations can be made on the profiles in Figure 46d and e approximately between -100 µm and -180 µm in y-axis, but not on profiles in Figure 46a and b which are for CM-dry case. In addition, by comparing the gray and orange profiles with the blue profile in Figure 46c and d (see the arrows), the layer thickness may be estimated at about 10 µm.

Figure 47 shows the EDS analysis on the flank wear land for the same tools in Figure 45. For the spectrum at each marked location, only elements with atomic percent higher than 5% are displayed.

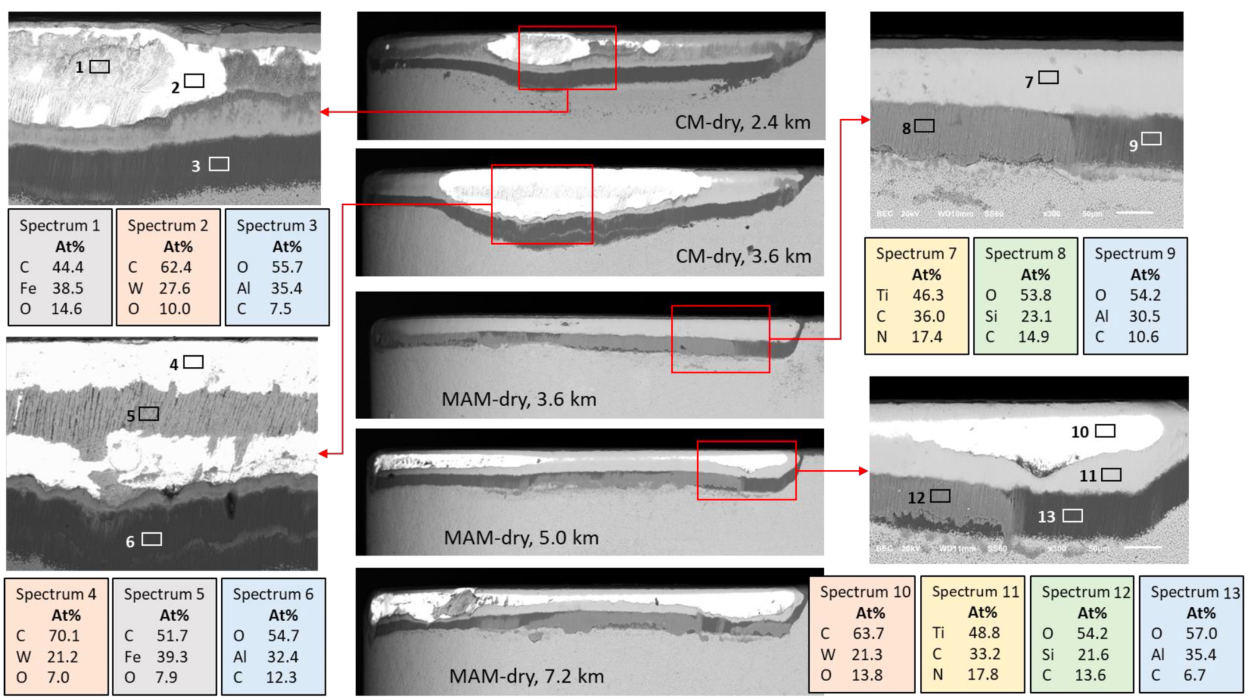

Figure 47: EDS analysis of the flank wear land of the etched tools in Figure 45. The SiO_2 layer is stable throughout the test in MAM but not in CM. Adapted from [81].

Spectra 1 and 5 (gray) indicate the iron adhesion that has not been completely removed by etching; spectra 2, 4 and 10 (orange) indicate the exposed carbide substrate; spectra 3, 6, 9 and 13 (blue) indicate the exposed Al_2O_3 coating; spectra 7 and 11 (yellow) indicate the exposed TiCN coating; spectra 8 and 12 (green) indicate the silicon oxide (SiO_2) deposition layer (based on the presence of Si and O) which cannot be etched by HCl acid. It is evident the SiO_2 layer is formed in the MAM-dry case but not in the CM-dry case. The SiO_2 layer seems to be mainly formed on the exposed Al_2O_3 coating layer. Before the coating breach occurred (3.6 km), the SiO_2 layer was present on both the nose flank and the main flank except at the end of the cutting edge. After the coating was breached (5.0 and 7.2 km), the SiO_2 layer was still present on the main flank. It is evident there was significantly less wear in the corresponding flank region where SiO_2 layer is present.

4.3.3 Wear reduction mechanisms

The effect of SiO_2 layer formation is illustrated in Figure 48. When there is no such layer formation in the CM-dry case (Figure 48a), the iron work material will not adhere to the flank wear land until the coating is breached. The coating on the flank is directly subjected to the intense rubbing by the newly generated work surface leading to higher rate of abrasive wear.

In contrast, in MAM-dry case (Figure 48b), a stable SiO_2 deposition layer is formed on the trailing edge of the flank wear land where Al_2O_3 coating is exposed. The SiO_2 layer is thick enough to create a geometrical step on the flank wear land. This will result in the accumulation of stagnated iron in front of the step covering the upper portion of the wear land where the TiCN coating is exposed (Figure 48b). The stagnated iron layer accumulated ahead of the SiO_2 deposition layer protects the flank coating from the intense rubbing by the newly generated work surface.

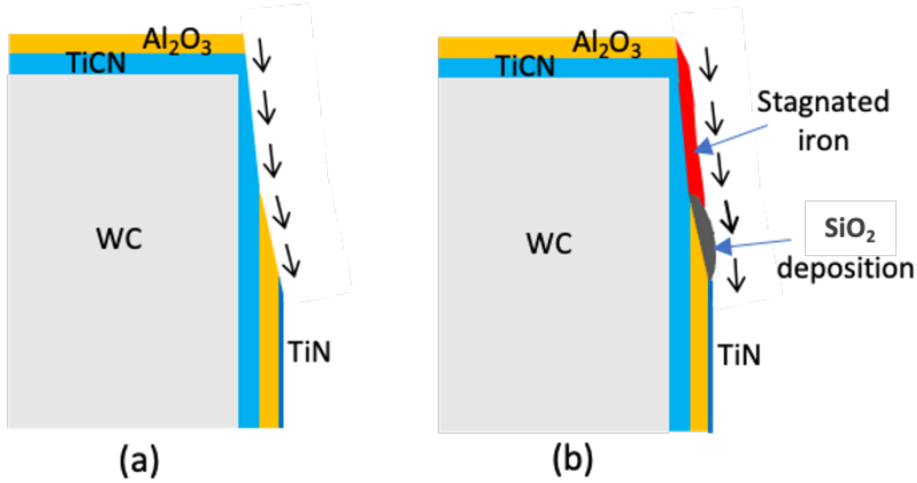

Figure 48: Schematic illustration of the tribological condition at the tool flank in (a) CM-dry and (b) MAM-dry case. The Silica layer does not form in CM but is formed in MAM protecting the coating from the material flow. Adapted from [81].

Therefore, the abrasive wear on the flank coating is significantly reduced. The unique adhesion previously observed on the tool coating in MAM-dry case (see Figures 39, 43 and 44) is in fact the stagnated iron which is formed purely due to the geometric effect created by the presence of the SiO_2 deposition layer. Like iron adhesion (on exposed carbide), the stagnated iron will increase the cutting forces (see Figures 41 and 42), but unlike iron adhesion, the stagnated iron will greatly reduce the flank wear (see Figure 40).

Besides the formation of SiO_2 layer and stagnated iron, the ability to preserve the coating on the cutting edge (rake side) is another important factor which leads to the wear reduction in MAM-dry case. In CM-dry case, the coating at the cutting edge is not well preserved. Damage on edge coating occurs even before the breach of the coating on the flank. After the coating is breached on the flank, coating damages on the cutting edge exacerbate the rapid wear on the flank which is illustrated in Figure 49a. When the coating AB is damaged and broken away, severe iron adhesion will occur on the exposed carbide around the edge BAA'. Considering the material flow direction

(Vc), the wear on the exposed carbide will progress rapidly changing the flank profile from AA' to BB' and the cutting edge moving from A to B.

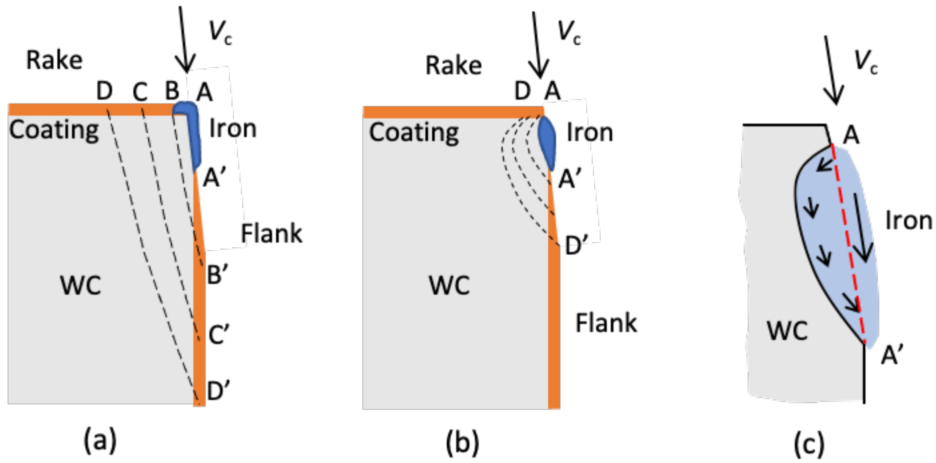

Figure 49: Schematic illustration of wear progression after coating breach in (a) CM-dry and (b, c) MAM-dry cases. The rake side coating is preserved in MAM unlike in CM, stagnating the material flow and slowing the wear. Adapted from [81].

Coating BC is again broken away which will allow flank wear to progress rapidly from BB' to CC'. Similarly, when coating CD is broken away, flank wear will progress rapidly from CC' to DD'. Note the breaking of edge coating at the rake side and the progression of flank wear on the exposed carbide at the flank side occur simultaneously in this process through the iron adhesion layer.

In MAM-dry case, the coating at the cutting edge is well preserved even after the coating is breached on the flank. This slows down the rapid wear on the exposed carbide on the flank side which is illustrated in Figure 49b and Figure 49c. Since the edge coating on the rake side is well preserved, severe adhesion can only occur on the flank side below the cutting edge where the carbide is exposed (AA'). In this case, the wear will create a concave shaped profile or a valley on the exposed carbide. Work material trapped inside the valley will flow at a lower velocity compared to the material outside the valley (Figure 49c). This will reduce the shear intensity at the carbide interface and hence slow down the wear on the carbide. The deeper the created valley, the slower the material flow along the carbide interface, and hence the lower the wear rate on the carbide. This means the wear on the exposed carbide will decelerate. Eventually, the abrasive wear on the edge coating from the flank side will control the overall flank wear progression in the depth direction. Therefore, the flank wear depth is significantly smaller in MAM-dry case than CM-dry case (see Figure 46).

4.3.4 Wear characteristics in lubricated condition

Figure 50 shows the spread of adhesion on tool flank in CM-lubricated and MAM- lubricated cases, which reflects the progression of coating breach. In CM-lubricated case, coating breach started at a spot on the main flank which is close to the nose (see arrow in Figure 48a). Then it quickly spread to the main flank along the side cutting edge but does not progress to the nose flank (Figure 48b).

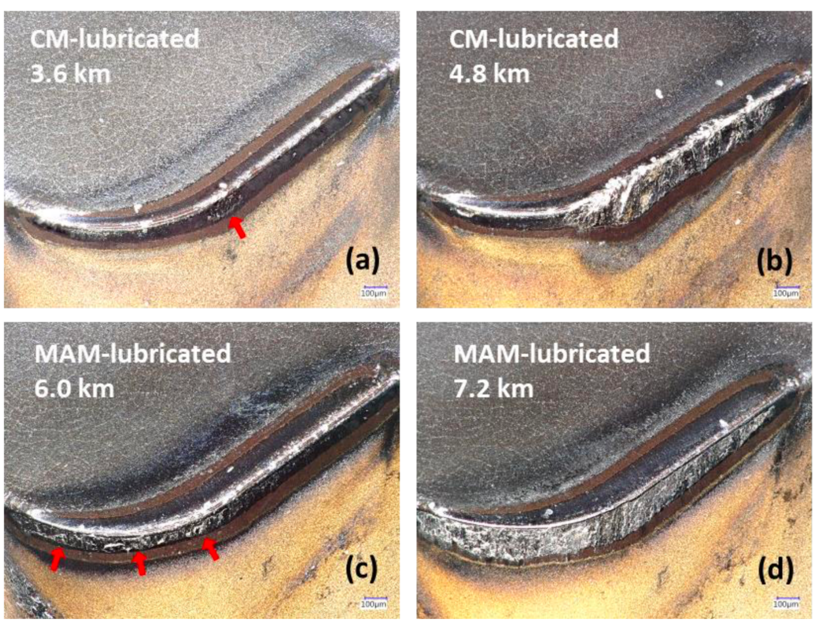

Figure 50: Digital microscope images of the tool edges at the last two cutting intervals in CM- lubricated (top row) and MAM-lubricated (bottom row) cases. Tool number: 2 and 4. Adapted from [81].

In MAM-lubricated case, the coating breach starts on the nose flank (see arrows in Figure 50d) and then spreads to the main flank along the side cutting edge (Figure 50e). The breaching process in CM-lubricated case is essentially the same as in CM-dry case. The breaching process in MAM-lubricated case is different from the MAM-dry case. There is no separate start of the breach at the end of the main flank, and the breached zone spreads from the nose flank to the main flank much faster than in CM-dry case.

Figure 51 shows the detailed comparison of the tools after etching in CM-lubricated and MAM-lubricated cases. Figure 52 shows the section profiles of the flank wear lands corresponding to the sections A, B and C marked in Figure 51. Figure 53 shows the EDS analysis of the marked tool flank region in Figure 51a and Figure 51c.

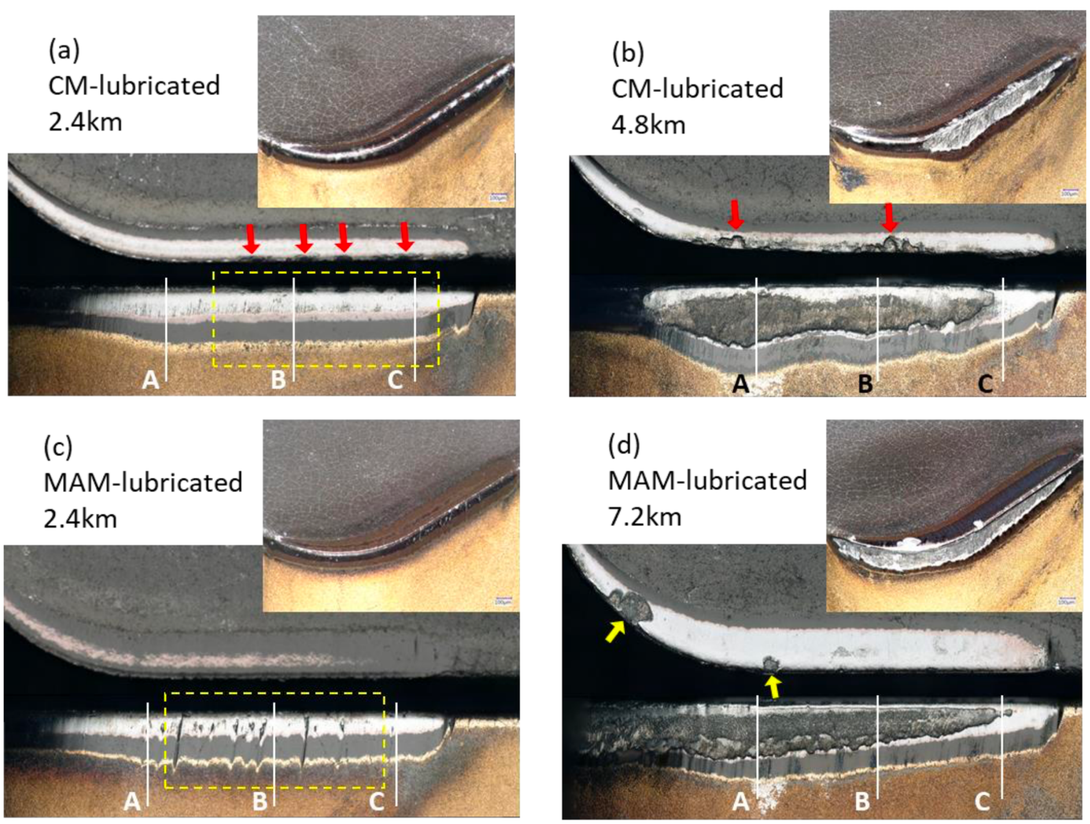

Figure 51: Digital microscope images of etched tools with different cutting distances in CM-lubricated (top row) and MAM-lubricated (bottom row) turning tests. Tool number: 6, 2, 8 and 4. Adapted from [81].

It is evident the application of cutting fluid does not fundamentally alter the wear characteristics in CM turning. In CM- lubricated case, cutting edge is not well preserved as in CM-dry case; edge damages can be observed before the coating is breached on tool flank (see red arrows in Figure 51a and Figure 53a).

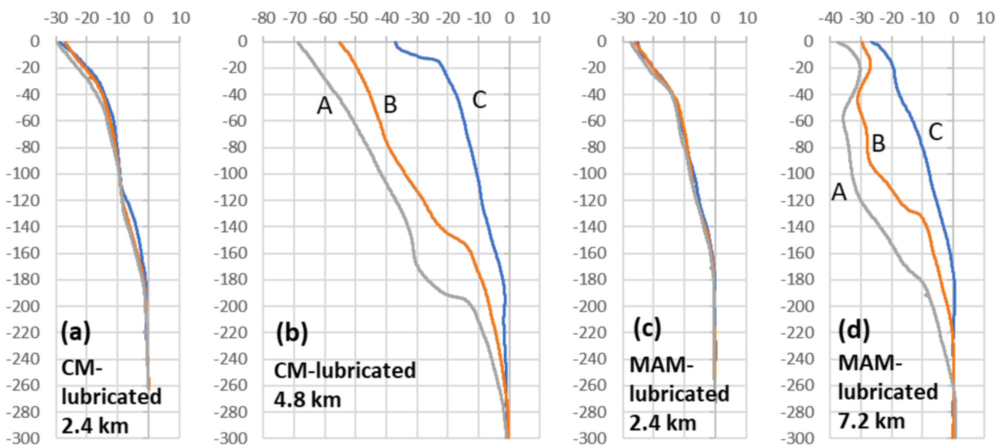

Figure 52: Section profiles of the flank wear lands of the etched tools shown in Figure 51. The gray, orange, and blue profiles correspond to sections A, B, and C marked in Figure 51, respectively. Adapted from [81].

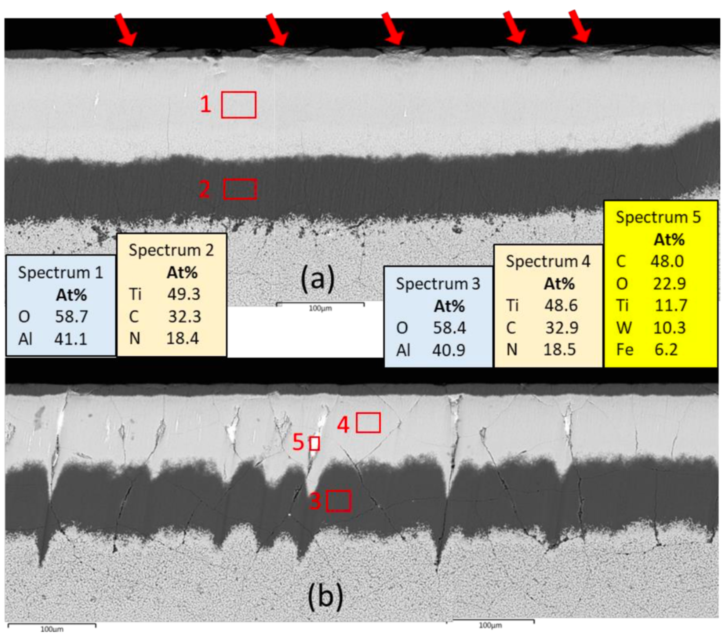

Figure 53: EDS analysis of the tool flank (after etching) at the cutting distance of 2.4 km in (a) CM- lubricated and (b) MAM-lubricated cases, corresponding to the marked region in Figure 51a and Figure 51c, respectively. Tool number: 6 and 8. Adapted from [81].

Once the coating breach starts on tool flank, the unpreserved cutting edge exacerbates the rapid wear on the exposed carbide in the same way as illustrated in Figure 49a. This is evidenced by the severe coating damages on the rake side of the cutting edge (see red arrows in Figure 51b), the substantially large height and depth of the flank wear (Figure 52b), and especially the occurrence of maximum flank wear depth at the cutting edge (Figure 52b). The cutting fluid does have some lubrication and cooling effects which can be inferred from the reduced forces (Figure 42) and less burned color present on the tool rake face (Figure 51b compared to Figure 45b). However, these effects are not dominant as they only result in slight improvement in tool life (Figs. Figure 39 and Figure 40).

The cutting fluid results in more fundamental changes on the wear characteristics in MAM turning. The SiO_2 layer, a geometric step on the flank, in MAM-dry case (Figs. Figure 45c-e and Figure 46c) could not be observed in MAM-lubricated case (Figure 51c,d and Figure 52c). The explanation for this is that the lubricant probably decreases the required friction to form this layer accumulation. The EDS analysis also confirms there is no detection of SiO_2 on the flank in MAM-lubricated case (Figure 53b). Apparently, the formation of the SiO_2 layer on the flank is precluded by the cutting fluid. Without the SiO_2 layer formation, there is no stagnated iron layer formation. Therefore, the wear reduction mechanism illustrated in Fig. 12b does not occur in MAM-lubricated case. However, the wear reduction (compared to CM) due to the preservation of tool edge coating (see Figure 49b and c) remains effective. This is evidenced by the smooth cutting edge and rake face in Figure 51d and the concave shaped flank profiles in Figure 52d. Note the two isolated coating damages on the rake face (yellow arrows in Figure 51d) could not be observed until the tool is etched (see Figure 50d). When comparing the flank wear between MAM-lubricated and MAM-dry cases, despite of the similar flank wear depth (~ 35 μm), the flank wear land is significantly lower in MAM-dry case (see Figure 40, Figure 46e and Figure 52d). This indicates that the preservation of tool edge coating is responsible for reducing flank wear depth and the SiO_2 layer formation is responsible for reducing the size of flank wear land.

The cutting fluid should have enhanced lubrication and cooling effects in MAM compared to CM turning, because the periodic disruptions at the tool-chip and tool-work interfaces allow the fluid to better access to the contact interfaces. However, the fluid also leads to larger temperature variation during MAM turning which tends to promote thermal cracking on the tool coating. These cracks can be clearly observed in Figure 53b. It is also evident when the coating cracks are large enough, they can trap the work material during cutting, which increases the local wear rate. Therefore, there are local variations in flank wear height and the wear land shows many pits and grooves (see Figure 51c and Figure 53b). However, the thermal cracks are not dominant on the overall wear progression as the effect remains local. It is the coating breach starting at the nose flank and quickly spreading to the main flank (see Figure 50c,d and Figure 51d) that is most influential on the final tool life in MAM-lubricated turning. In addition, thermal cracks are likely responsible for formation of the two coating damages while etching the tool as shown in Figure 51d.

4.3.5 Coating breach in MAM turning

In both MAM-dry and MAM-lubricated cases, it is observed that the coating breach starts at nose flank. This can be explained by the continuous contact and increased rubbing at the minor flank. In MAM turning, the cutting tool is vibrated in the tool feed direction, so the periodic disengagement between the tool and the work material only occurs at the main flank side of the cutting edge. The cutting edge on the tool nose will remain in continuous contact with the work material because the cutting edge and correspondingly the minor flank are parallel to the vibration direction. Moreover, the modulation will increase the rubbing at the tool nose. Therefore, a higher wear rate should be expected at the minor flank. In MAM-dry case, the spread of coating breach from the minor flank to the main flank occurs very gradually showing no apparent acceleration in wear progression. This should be attributed to the SiO_2 layer (and stagnated iron layer) protection. The coating breach emanated from the other end of the main flank is more likely due to the lack of SiO_2 layer protection (see Figure 47). In MAM-lubricated case, coating breach starts only at the minor flank. Once the breach starts, it spreads quickly to the main flank showing an acceleration of the wear progression. This indicates that the cutting fluid is not as effective as the formation of SiO_2 layer in suppressing the spread of the breach.

However, the cutting fluid is effective in reducing the abrasive wear on the coating. This is evidenced by the significant reduction in wear at the end of the main flank compared to MAM-dry case (Figure 51d vs. Figure 45e). Note there is no SiO_2 layer protection at the end of the main flank for both cases, so the wear reduction in this region can be attributed only to the cutting fluid effect.

4.3.6 Further discussion

The success of MAM-dry case comes from the formation of SiO_2 layer which should be dependent on temperature, material, and the tool-work contact condition. The cutting speed and modulation frequency will likely influence this layer formation as they will change cutting temperature and tool-work contact disruptions. The tool coating material should also play an important role in this layer formation. The stable SiO_2 layer is found to mainly form on the exposed Al_2O_3 coating. This might be due to the strong adhesion between the two materials at the high temperature during cutting. Whether the same SiO_2 layer formation will occur on other types of coated tools, especially those without Al_2O_3 coating layer, will need further investigation. The

SiO_2 layer formation apparently will depend on the work material. Besides CGI, the deposition layer may be formed in MAM-dry cutting of flake graphite iron (FGI), nodular graphite iron (NGI), and electrical steel which all have high silicon content. If so, significant tool wear reduction could also be achieved in cutting these materials by MAM. This is to be confirmed in future study.

The EDS analysis showed a fair amount of carbon present in the deposition layer (see Spectra 8 and 12 in Figure 47). Due to the uncertainty in detecting carbon content by EDS analysis, the deposition layer so far has been identified as silicon oxide SiO_2. However, it is also possible that the formed deposition layer is silicon oxycarbide (SiOC) which has enhanced mechanical and electrical properties compared to silicon oxide (SiO_2) [29]. It has been shown that Al_2O_3 is a good substrate material for fabricating SiOC-based thin films and coatings [30], which may explain the formation of the deposition layer preferably on the exposed Al_2O_3 coating.

The excellent preservation of the cutting tool edge (coating) during cutting is a common phenomenon in both MAM-dry and MAM-lubricated cases that contributes to the wear reduction compared to CM turning. Therefore, this phenomenon must be enabled by the unique cutting kinematics of MAM. The tool edge damage in CM turning are likely caused by the formation of build-up edge (BUE). Compared to FGI, the more ductile CGI and NGI have higher tendency to form BUE in a wider range of cutting speeds [13]. The repeated detaching and reforming of the BUE on the tool edge during cutting will likely cause the edge chipping and damage. It is possible that MAM can mitigate or suppress the formation of BUE due to the periodic disruptions at the tool-chip contact. Therefore, the tool edge is better preserved during MAM turning, which ultimately improves the machinability.

In the present study, the overall wear reduction in MAM-dry case (compared to CM) is more significant than that in MAM-lubricated case. Further study will be needed for more comprehensive evaluation in a wider range of cutting conditions (speed, federate, modulation frequency, fluid type, etc.). The key to the success of MAM-lubricated case is to control the wear at the nose flank due to the continuous contact and increased rubbing. The modulation frequency and amplitude and the tool nose radius will likely influence this wear. The cutting fluid used in the present study is simple vegetable oil which has more lubrication effect than the cooling effect. It is also worth testing water-based coolant in MAM. This will help determine the relative importance between the lubrication effect and cooling effect on the wear reduction. However, with water-based coolant, thermal cracking may become a potential issue, so a tradeoff between enhanced cooling and thermal cracking is likely needed.

4.4 Conclusions

In this study, the characteristics of tool wear evolution and cutting forces in conventional (CM) turning and modulated (MAM) turning of CGI with coated carbide tools are investigated at the cutting speed of 250 m/min. The following conclusions may be drawn from the study.

In CM turning, the coating breach on the main flank occurs very early triggering rapid wear on the exposed carbide accompanied by severe iron adhesion. The application of cutting fluid only slightly delays the breach of tool coating but cannot slow down the rapid wear and severe tool adhesion once coating is breached.

MAM can significantly reduce the tool wear compared to CM in both dry and lubricated cutting conditions. When comparing MAM-dry and MAM-lubricated cases, the cutting forces are lower in the MAM-lubricated case with increasing tool wear compared to MAM-dry case.

In the MAM-dry case, two mechanisms account for the wear reduction: (1) the formation of SiO_2 deposition (and stagnated iron) protective layer on the tool flank face; and (2) the preservation of coatings on the tool cutting edge. The first mechanism is responsible for greatly reducing the flank wear land size while the second mechanism is responsible for greatly reducing the flank wear depth after the coating is breached.

In the MAM-lubricated case, the cutting fluid precludes the formation of SiO_2 deposition layer. The wear reduction mechanisms (compared to CM) are changed to (1) the enhanced lubrication and cooling at periodically disrupted tool-chip and tool-work contacts and (2) the preservation of coatings on the tool cutting edge.

The start of a coating breach at the tool nose flank in MAM is due to the continuous contact and increase rubbing at the nose flank. The formation of SiO_2 deposition layer is more effective than the cutting fluid to suppress the spread of coating breach from the nose flank to the main flank.

CHAPTER 5: FREQUENCY DEPENDANCE OF WEAR IN MODULATION-ASSISTED MACHINING OF COMPACTED GRAPHITE IRON

5.1 Summary

As explained in the previous chapters, MAM is capable of reducing the wear in dry turning CGI with coated carbides, especially at high cutting speeds. The main two mechanisms for wear reduction are: 1) the formation of a Silicon Oxide (SiO_2) layer on the flank side and 2) the preservation of the coatings in the cutting edge. As the ratio between modulation frequency and workpiece rotation frequency increases, the number of cutting disruptions per turn increases because the MAM tool path will contain a larger number of cycles per workpiece revolution. The present study aims to identify the effect of the MAM frequency ratio on the tool wear in dry turning of CGI with coated carbides. Three different frequency ratios were used: 3.5x(low), 6.5x(medium) and 9.5x(high). The frequency ratio is found to significantly influence the crater wear, but not the flank wear. As expected, the smallest frequency ratio (3.5x) exhibits the most crater wear, whereas the highest ratio (9.5x) yields the least crater wear. This is due to a smaller ratio generating less interruptions and increasing the edge temperature. The frequency ratio can also influence the overall tool temperature which can be used to explain the evolution of wear. However, increasing the MAM frequency ratio also increases nose wear due to the tool nose being constantly engaged with the workpiece, leading to 3.5x and 9.5x both exhibiting a higher temperature than 6.5x. For even extremely low values of the frequency ratio (1.5x), it is found that the flank wear improvement mechanisms for MAM described in Chapter 3 still prevail and that they are decoupled from crater wear, which indicates that they are independent from the frequency ratio. Finally, it is found that the frequency ratio can be adjusted to an optimal frequency ratio, which

generates the lowest temperature and the provides the best balance between crater wear and nose wear while always reducing flank wear.

5.2 Materials and methods

In this study the same setup, cutting tool and CGI work material implemented in Chapter 2 for dry cutting was used (see Figure 27). The same AKG wire thermocouple setup of chapter 2 is implemented and the criteria to select the location of the thermocouple junction is the same which is the conventional thermocouple method as described by most researchers[82–87]. Specifically, the temperature is measured at a location away from the cutting edge which is more convenient for routine monitoring of the cutting process and does not require that the setup deviates significantly from the conditions typically found in industry[88–92]. Even though this method presents issues such as junction placement accuracy and temperature gradient effects, it is expected that these effects are negligible, and the measurement is only used to compare different cutting conditions and intervals and not to predict the edge temperature [93,94]. In order to change the modulation frequency for each test, the frequency is directly input into the waveform generator (BK4007B) and the value is calculated as a constant (the desired ratio) multiplied by the lathe rotational frequency during that cutting interval.

Table 5 provides a summary of the tests performed in this study. Each condition is tested with a new tool. The cutting speed is kept constant (Vc=350 m/min), feed rate (ho=.04mm/rev) and depth of cut (d=1.5mm) are constant for all tests. In the present study, only the speed of 350m/min is selected because it yields the greatest differences in wear rate between conventional machining (CM) and MAM in order to better see these differences sooner and to avoid wasting work material.

As explained in Chapter 2, the main difference between conventional turning and MAM turning is the cyclic number of disruptions per turn of the tool-chip contact in MAM. Such disruption is possible due to intersection of the cutting path when the frequency ratio fm/fw takes half integer values, where fm is the modulation frequency and fw is the rotation frequency. Additionally, as the frequency ratio becomes larger, the number of path intersections and interruptions increases because the modulation wave performs more cycles per revolution of the workpiece. For this reason, the only variable that is changed is the modulation frequency and therefore the frequency ratio for each condition. Three frequency ratios fm/fw were selected: 3.5x, 6.5x and 9.5x. The actual value of fm at every interval will vary depending on the diameter of the workpiece at that specific interval (see range in Table 5).These values were selected according to the study in Chapter 1 where the cutting speed was varied in the dry condition, but the modulation ratio is set as 6.5x at 350m/min keeping the piezo frequency around the order of 100 Hz in order to compare with MAM at other speeds such as 150 and 250 m/min. 3.5x is selected as a ratio with less expected cutting interruptions than 6.5x, and 9.5x as a ratio with more cutting interruptions. According to [38,95] we expect that the number of interruptions will influence the reduced peak cutting temperature and therefore the wear rate. This is why some researchers have found that wear is sometimes reduced when increasing cutting speeds in interrupted operations such as milling [96,97] which has not been observed at low cutting speeds[38,98]. To further investigate the formation of SiOC layers present in the flank wear land as described in Chapter 3, three additional tests at a single pass are performed and the ratio was reduced to an extreme value of 1.5x to evaluate if the formation of the Silicon oxide layer is still possible.

Each cutting interval is 1.2 km distance, after which the tool was removed to be characterized in an optical microscope (Nikon Eclipse LV100ND and Keyence VHX6000). Then the test is resumed with the same tool for another interval of 1.2km. the test is stopped if the flank wear reaches more than 300 μm or the cutting distance is 7.2km. Once the test is stopped, the tool is characterized with a JEOL 6610LV scanning electron microscope (SEM) and energy dispersive spectroscopy (EDS) to identify the deposited materials as well as the breach of the coatings. The characterization is done both before and after etching the tool for 45 min with HCL (19%) to remove any work material adhesion.

Table 5: List of turning tests reported in this study.

Tool number	Test name	Cutting Speed (m/min)	Lubrication condition	Feedrate (mm/rev)	Depth of cut (mm)	f_m/f_w	f_m (Hz)	V_{pp} (V)	Total cutting distance
1	CM-350	350	dry	0.04	1.5	-	-	-	2.4 km
2	MAM-350-3.5x	350	dry	0.04	1.5	3.5	46-58	150	7.2 km
3	MAM-350-6.5x	350	dry	0.04	1.5	6.5	86-108	150	7.2 km
4	MAM-350-9.5x	350	dry	0.04	1.5	9.5	126-158	150	7.2 km
5	CM-350	350	dry	0.04	1.5	-	126-158	150	1.2 km
6	MAM-350-1.5x	350	dry	0.04	1.5	1.5	20-25	150	1.2 km
7	MAM-350-6.5x	350	dry	0.04	1.5	6.5	86-108	150	1.2 km

5.3 Results and discussion

5.3.1 Flank wear behavior

Figure 54 shows the progression of flank wear for CM and for MAM at different frequency ratios with the cutting parameters as described in Table 5. It is evident that flank wear is significantly improved in MAM as compared to CM, with CM tool failure occurring as soon as in interval 2 (2.4km) whereas none of the MAM tools at any frequency ratio reached the failure criterion even after interval 6 (7.2km). Even though the MAM tool life improved drastically, there are slight differences between the MAM tests in terms of wear. Specifically, the wear at the end of the test (7.2km) of 6.5x is slightly lower than that of 3.5x and 9.5x is lower than both 3.5x and 6.5x. However, this behavior is not uniform. When comparing 3.5x and 6.5x, the wear of 3.5x is lower than 6.5x for the first interval, increases to be slightly higher for the second and third interval, becomes slightly lower again for the fourth interval and then finally becomes consistently higher for the fifth and sixth intervals. When considering 9.5x, we see that the wear is consistently below both 3.5x and 6.5x throughout the test, resulting in the least wear from all tests performed. Another interesting aspect is that the wear starts to increase slowly but consistently from the first interval in 3.5x, from the second interval in 6.5x and from the third interval in 9.5x. This indicates that the severity of the tool contact condition is further reduced for the flank side with an increase in the number of interruptions (and therefore frequency ratio) just as expected. However, these results indicate that the variation of the frequency ratio does not significantly influence the magnitude of the flank wear height.

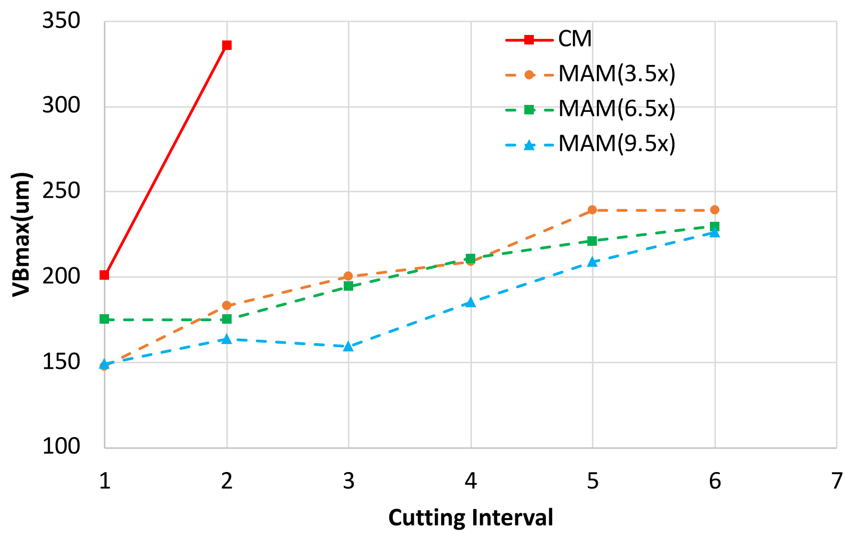

Figure 54: Flank wear progression for CM, MAM at 3.5x, MAM at 6.5x and MAM at 9.5x frequency ratio. MAM flank wear is reduced but not affected by frequency ratio.

Figure 55 shows the etched and unetched images of the tool at the final stages for each case. The wear in MAM is evidently smaller than for CM even after a much larger cutting distance (7.2 km in MAM vs 2.4 km in CM). The amount of iron adhesion is also significantly smaller for all MAM cases as compared to CM. After etching, the iron can be removed to visualize the edge wear shape for all cases. In CM, the failure occurs at a large average flank wear height and a very small crater wear (after failure, the fracture removed a large portion of the rake side). In MAM however, there is a more defined crater wear area and a much smaller average flank wear height which is similar for all three MAM cases.

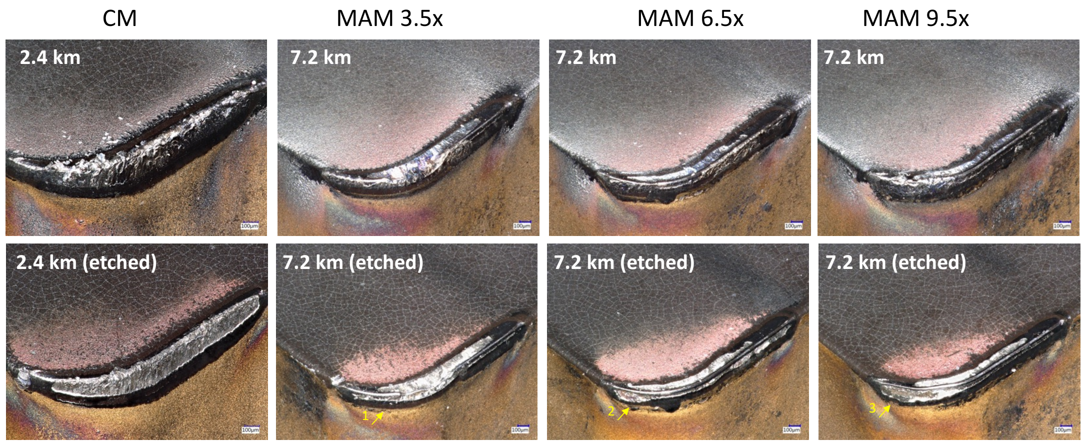

Figure 55: Tool images at the final cutting distance before etching (top row) and after etching (bottom row). Wear morphology is different depending on the ratio for MAM.

5.3.2 Nose wear and crater wear behavior

Figure 56 shows high resolution micrographs for the wear morphology details in CM and the three MAM cases of Figure 55. Again, the flank wear height is significantly smaller for all three MAM cases as compared to CM, and the flank wear morphology is different. In CM (Figure 56a), the flank wear height is larger at the center and smaller at the edges of the cutting edge., whereas for MAM (Figure 56b-d) the flank wear height is smaller at the center and higher at the ends of the cutting edge. As discussed in previous chapters, the interruptions and consequently lower tool temperatures at the cutting edge in MAM alleviate the severe condition in the tool-chip contact preserving the edge sharpness and reducing flank wear compared to CM. It is interesting to analyze the crater wear area in all three MAM cases. The orange dashed rectangles in Figure 56b-d represents the portion of the crater area that is within the main cutting edge (before the nose area starts). The crater area width is more uniform for 3.5x and 9.5x than for 6.5x. In 6.5x there is a wider uniform region close to the nose (Figure 56c arrow 3) and a narrower region far from the nose (Figure 56c arrow 4). In general, the crater area is larger for 3.5x than for 6.5x and larger for 6.5x than 9.5x. This behavior is expected because with a higher number of interruptions the heat transfer is expected to be farther from the steady state, ultimately reducing the peak temperature at the edge and therefore reducing crater wear. As 3.5x should have the least number of interruptions, it is expected to have the highest cutting temperature of the three MAM cases, which resulted in the crater wear being more severe and causing edge damage (Figure 56b arrows 1 and 2). On the other extreme, the nose wear is more prominent at a higher frequency ratio, so it is higher at 9.5x than 6.5x and higher at 6.5x than 3.5x (see Figure 55 arrows 1, 2, 3). In 9.5x the higher nose wear changes the nose profile of the rake side as can be seen in Figure 56d arrows 5 and 6.

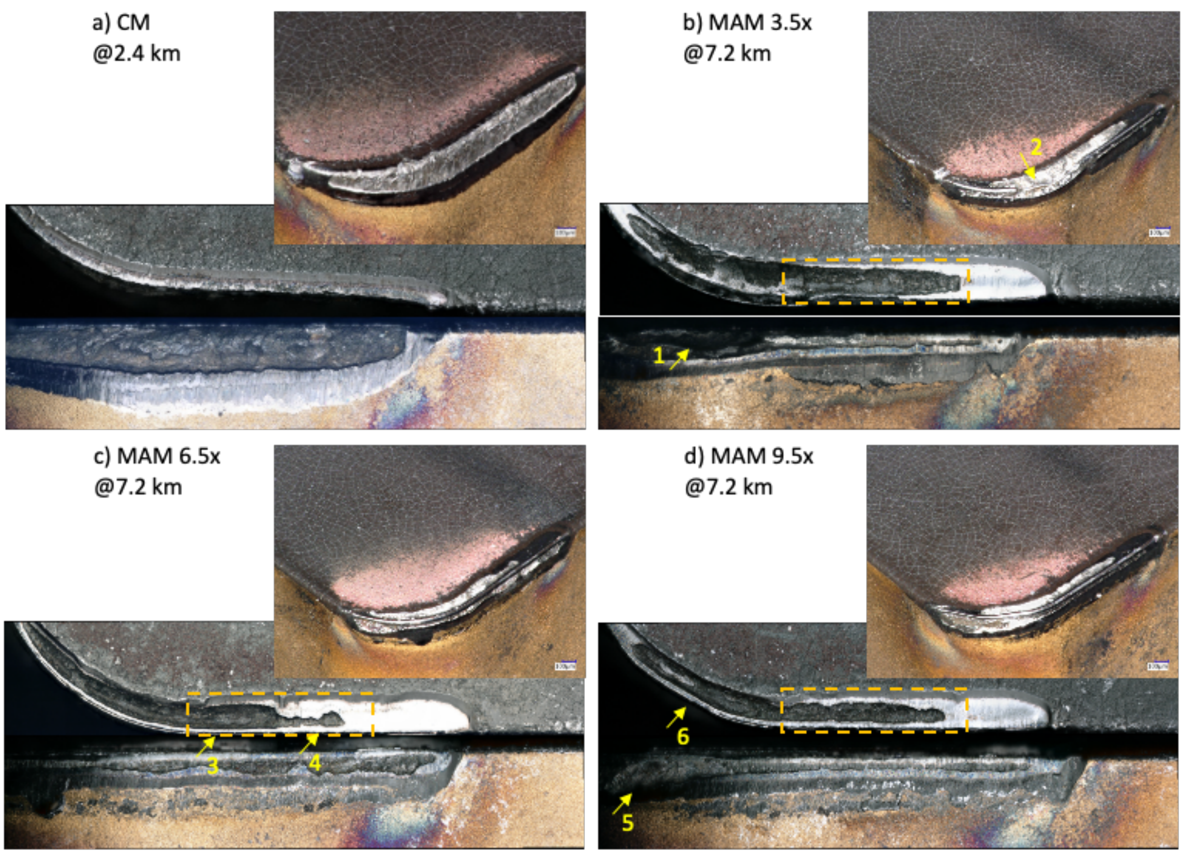

Figure 56: Digital microscope images of etched tools with different cutting distances MAM turning tests. Higher ratio reduces crater wear but increases nose wear.

This is expected due to the fact that in MAM the nose is always engaged with the work material even when the main cutting edge is disengaged, so a higher vibration frequency results in a more severe rubbing effect ultimately generating more nose wear.

In all three MAM cases, a silicon deposition is identified in the flank wear land as a grey layer in the alumina layer (Figure 56 b-d) which agrees with the results found on Chapter 3. SEM backscatter images for tools in Figure 56 are in Figure 57b-d, where the silicon deposition areas are shown in light gray color and identified with yellow arrows, whereas the alumina coating is the black band that extends in the flank wear land area and signaled with red arrows.

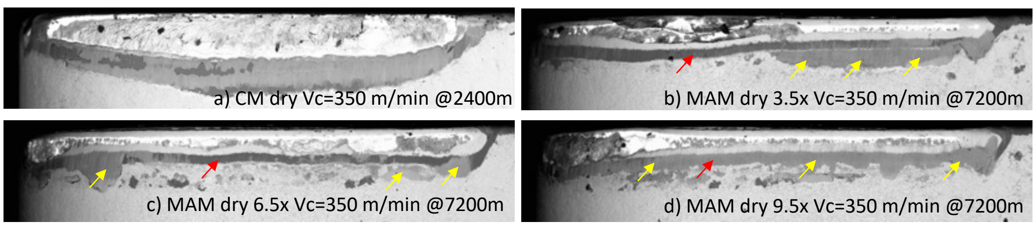

Figure 57: SEM Backscatter images for tools in Figure 56. SiO_2 layer is formed for all MAM frequency ratios but not on CM.

Given that the CM tool is already at failure with a severe breach of the coating, the Silicon deposition and flank wear morphology analysis makes sense only for the three MAM cases. The shape of the Silicon layer at this final stage is different for different frequencies. In MAM 3.5x the layer is denser far from the most damaged region of the cutting edge and it extends downwards from the alumina coating into the TiN coating (see yellow arrows in Figure 57b). In MAM 6.5x the layer seems to have been partially removed in the previous pass with more agglomerations around the left and right ends of the cutting edge (see yellow arrows in Figure 57c). In MAM 9.5x the layer is continuous on the alumina coating, and it extends to cover the entire cutting edge length (see arrows in Figure 57d). Examining the exposed alumina coating we also confirm that the flank wear land height is in average very similar (as in the final interval of Figure 54 for MAM) regardless of frequency ratio. Also, MAM 3.5x as well as MAM 9.5x the flank wear land area shape is slightly inclined towards the left end of the cutting edge (near the nose in 9.5x and crater failure area in 3.5x) whereas in MAM 6.5x the flank wear land area is mostly horizontal. Again, this mild influence in flank wear is expected due to 3.5x exhibiting more crater damage and 9.5x more nose damage (both to the left of the cutting edge), whereas 6.5x exhibits a better balance between crater and nose wear because they are both not excessively large as 3.5x and 9.5x.

5.3.3 Crater wear and Silicon layer formation

To investigate the formation of a silica layer during cutting, a single pass test with CM, the nominal value of 6.5x and the extreme low ratio of 1.5x was performed. The tool images before and after etching are displayed in Figure 58. It is evident that the benefit of MAM at 6.5x and even at the 1.5x ratio is still present, given that the flank wear height is significantly reduced. There is also no evidence of significant difference between nose wear for the ratios of 1.5x and 6.5x (Figure 58), indicating that these effects are cumulative and will only show up in large cutting distances that can only be achieved in MAM. Crater wear is more severe in CM, where an extensive breach of the coating (white area spanning from arrows 1 to 2) exposing the TiCN beneath the Alumna layer is seen. It is also evident that the crater wear is more significant in 1.5x than 6.5x since no coating breach is seen in 6.5x whereas the TiCN beneath the alumina coating already starts to be exposed in 1.5x (white area spanning from arrows 3 to 4). These results are similar to the ones of Figure 56b-d, indicating a higher rake side temperature for 1.5x than for 6.5x resulting from a less interrupted cutting regime. In Figure 59 SEM backscatter images for tools in Figure 58 are displayed. In terms of flank side, for CM the alumina coating does not show any deposition of Silicon material. However, for MAM the Silicon deposition covers the entire alumina coating area in a manner almost identical for both 6.5x and 1.5x. This proves that even at an extreme ratio of

1.5x, MAM is capable of forming this protective silicon layer that reduces flank wear as discussed in chapter 3.

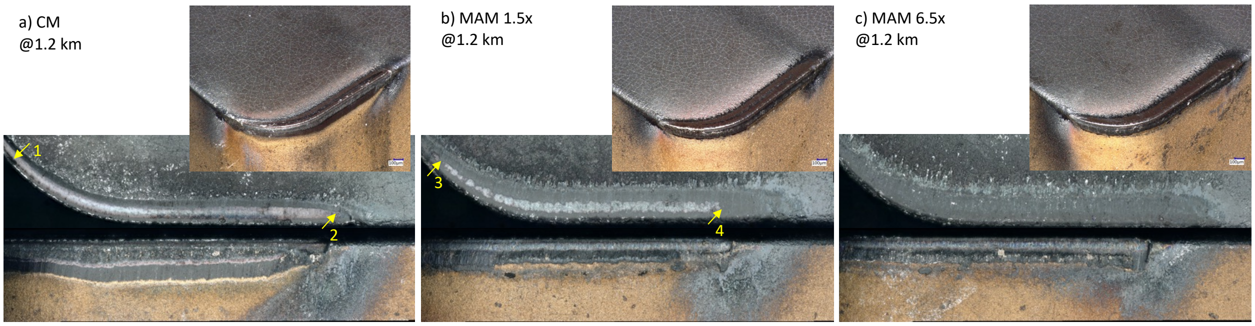

Figure 58: Tools after a single pass for the limit frequency test. Flank wear is reduced in MAM even at low ratio, but crater wear increases.

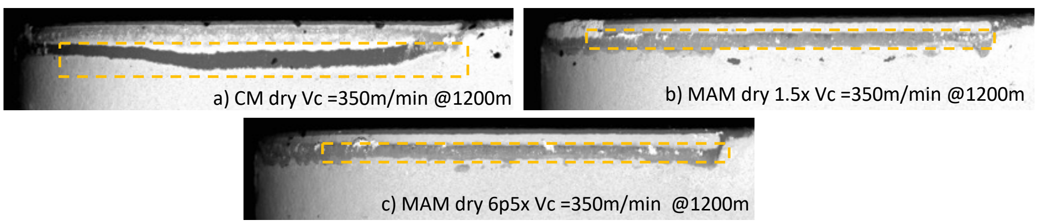

Figure 59: Backscatter images for the tools in Figure 58. SiO_2 layer forms in MAM reducing flank wear even at low ratio.

5.3.4 Tool temperature

The tool temperature history for all three MAM tests at all intervals is displayed in Figure 60, and the corresponding temperature for each interval at 150 seconds is plotted in Figure 61. For comparison purposes, the temperature curves for the two intervals of CM are displayed in the chart for each MAM test.

In general, the same trend is present in all the temperature curves, with an increase at a high rate in the first 30 seconds of cutting followed by a steady increase at a lower rate. As in chapter 2, the increase in temperature from one interval to the next one should correlate to the increase in wear. In CM, the temperature curve increases significantly from the first interval to the second, which can be explained by the severe wear and adhesion developed in the second interval. In all three MAM cases, the temperature rises gradually from one interval to the next one, but the temperature is always below or only slightly higher than the temperature of the second interval in CM. This is explained by the slow wear progression in MAM. For 3.5x the temperature starts well below the first interval of CM, but in the second interval it is very similar to the first interval of CM.

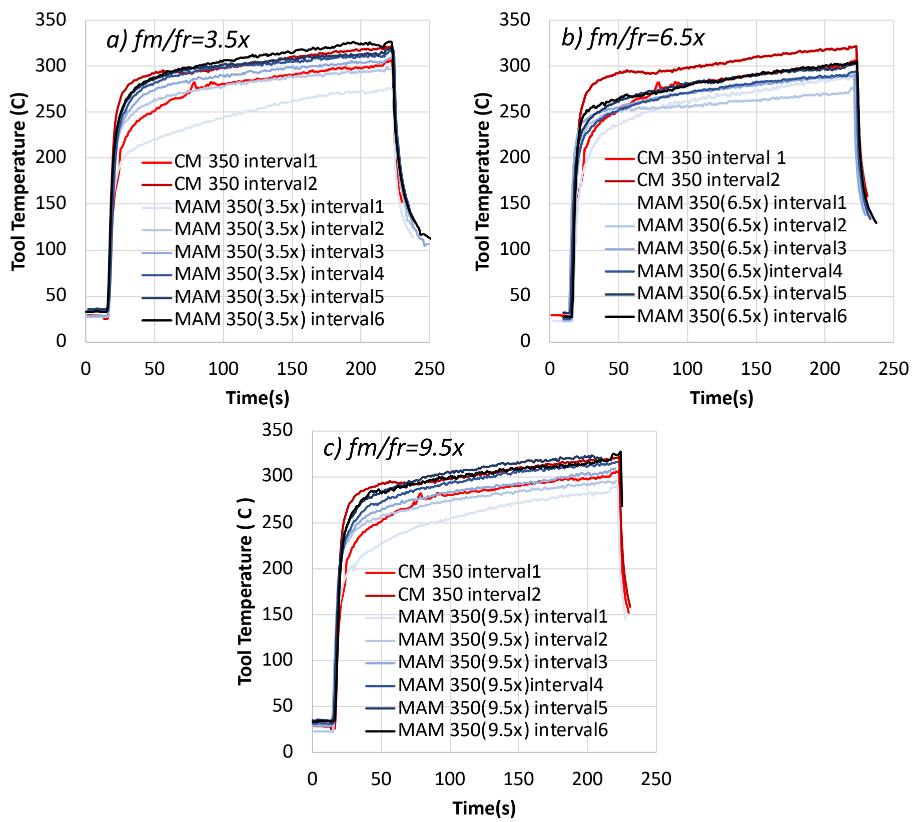

Figure 60: Tool temperature history compared to CM during each cutting interval for a) MAM 3.5x, b) MAM 6.5x and c) MAM 9.5x. The minimum temperature occurs at 6.5x.

The temperature continues to increase gradually until at the sixth interval it becomes slightly higher than the second interval of CM. For 9.5x the temperature increases in a manner almost identical to 3.5x, being slightly higher at the first and fifth intervals and slightly lower in all other intervals (Figure 61). However, for 6.5x the difference is more significant, with the first interval being slightly higher than 3.5x and 9.5x, but then decreasing significantly and staying well below the other two MAM cases from the second interval to the sixth interval Figure 61. In fact, even at the sixth interval, MAM 6.5x does not reach the temperature of CM at the second interval, so it seems the temperature reduction at 6.5x is closer to the optimal value than 3.5x and 9.5x.

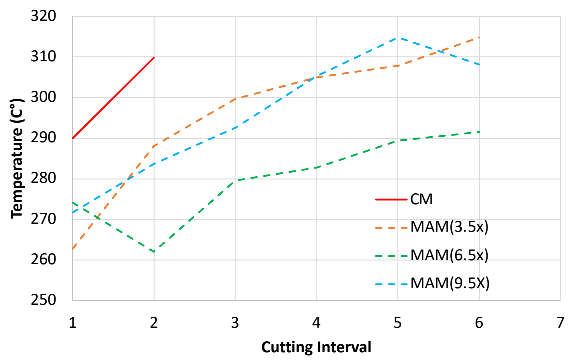

Figure 61: The temperature value at t=150 s in each temperature history curve in Figure 60. 6.5x ratio consistently exhibits the lowest temperature.

The previous results indicate that the rubbing effect might be more important than the number of disruptions per turn for the first interval. Therefore 6.5x and 9.5x exhibit a slightly higher temperature than 3.5x despite a higher number of disruptions. However, in subsequent intervals, 3.5x is always above 6.5x which signals the importance of the number of disruptions in the temperature reduction. This is confirmed by 3.5x having more crater area and damage than 6.5x and 9.5x. Although 9.5x should exhibit a lower rake temperature, the intense nose rubbing effect increases the heat coming from the nose, which explains why the temperature in 9.5 does not drop to the level of 6.5x and instead remains close to the level of 3.5x. This also explains why the nose wear in 9.5x is more severe than 3.5x and 6.5x. The results suggest that MAM 6.5x presents the optimum balance between nose and flank heat generation, which is confirmed by the balanced flank and nose wear and the overall lower tool temperature for almost all the intervals of the test.

5.4 Conclusions

In this study, the MAM turning setup developed in previous chapters was used to determine the effect of the modulation frequency ratio in the tool wear during external cylindrical turning of CGI. The tool wear, cutting forces and tool temperature are measured and characterized at the cutting speed of 350 m/min which is known to generate the fastest wear rate in conventional machining or CM. The findings are summarized as follows.

The frequency ratio does not significantly alter the flank wear, but it alters crater wear. Crater wear is reduced for higher frequency ratio, and a higher frequency ratio will therefore delay tool fracture for a longer distance than a lower frequency ratio. However, when the MAM frequency ratio achieves a certain threshold, other problems such as significant nose wear indicate that the highest frequency ratio is not necessarily the best option for overall improvement of the tool life (even when the flank wear is still improved). Of the three frequency ratio tests, 3.5x presents the least nose wear and the highest crater wear, 9.5x presents the least crater wear and the highest nose wear, and 6.5x presents the best balance between nose and crater wear being somewhat in between 3.5x and 9.5x and the lowest temperature in the tool. However, all tools present a similar amount of flank wear which is always significantly lower than for conventional machining.

Even at an extremely low frequency ratio such as 1.5x, MAM can reduce flank wear significantly when compared to CM, and this is due to the formation of a SiO_2 layer that entirely covers the flank wear land in the exposed coating of alumina. The morphology of the silicon layer changes slightly at the end of each cutting test due to the dominant wear mode for each frequency ratio, but the 1.5x results confirms that this layer started forming from the beginning of the test. The formation of the silicon layer independently from the more extensive crater wear in 1.5x compared to 6.5x proves that this layer can form independently of the ratio and therefore the layer and related flank wear improvement mechanism in MAM as described in Chapter 3 are independent from the crater wear and rake temperature, even when MAM reduces the rake temperature due to interrupted cutting. It is also important to note that nose and crater wear in MAM increase very slowly and over large distances, as compared to the fast aggressive wear behavior in CM.

The frequency ratio also influences the overall tool temperature, with a minimum tool temperature amongst the tested frequency ratios at 6.5x. The tool temperature is found to be dependent on the number of interruptions per turn which is controlled by frequency ratio, but also on the severity of the rubbing of the tool nose with the workpiece which increases with the modulation frequency. At a higher modulation ratio, the rubbing effect is large enough to generate another significant heat source other than the chip formation in the main cutting edge, cancelling the temperature improvement obtained from a more heavily interrupted cutting regime and increasing the overall tool temperature. However, for all the MAM frequencies tested the tool temperature remains below the temperature at CM that originates tool failure for most of the cutting test.

CONCLUSION

The evidence and discussions presented in this work proves that modulation-assisted machining or MAM is capable of significantly improving the tool life when cutting CGI with coated carbide tools. The mechanism by which the tool life is improved when compared to conventional machining (or CM) is described, as well as the method to adjust the MAM frequency to maximize tool life for a certain condition. The specific findings supporting these claims can be summarized for each chapter as follows.

As seen in Chapter 2, a new setup was developed and proven capable of performing MAM longitudinal turning experiments. It is found that the primary wear mode when turning CGI with coated carbide tool is flank wear for both CM and MAM turning. At low cutting speeds MAM does not significantly reduce the flank wear, but at high speeds the flank wear reduction is remarkable. This reduction is more evident when comparing the volume of material worn off the tool. MAM changes the way the tool wear originates. The wear in CM originates with breaching the coating at the center and then spreading rapidly outside from the edge, whereas for MAM the breach of the coating occurs in the nose and end of the cutting edge spreading towards the center. The breach of coating always precludes the adhesion of iron to the tool. MAM also delays the breach of coating and iron adhesion significantly compared to CM (increasing the cutting distance by an order of magnitude). The severe increase in the wear rate with the cutting speed commonly seen in CM turning, is reduced significantly in MAM turning explained by the unique wear mechanism in MAM. Therefore, MAM wear reduction is most significant at higher speeds. The increase in flank wear is correlated with an increase in the primary cutting force and the feed force, with the effect on the feed force being dominant. The severity of adhesion also plays a role in the force increase. For CM, the tool temperature increases significantly with the cutting speed, as well as with the cutting distance. However, the temperature in MAM turning is lower than for CM turning throughout the test, and for MAM the temperature increase in each interval is more gradual and correlated with the also gradual increase in forces and flank wear.

In Chapter 3 the tool wear evolution and forces in CM and MAM turning of CGI with coated carbides was examined to distinguish between mechanisms controlling wear in CM vs. MAM using the speed of 250 m/min, which is the lowest speed at which MAM shows a significant tool life increase as described in Chapter 2. In CM, the coating breach occurs very rapidly, accelerating the wear and iron adhesion. When cutting fluid is applied, the breach is briefly delayed but the rapid wear is not slowed down once the breach occurs. In contrast, MAM significantly reduces the flank wear in both dry and lubricated condition. The lubricant reduces the forces for both CM and MAM turning as compared to the dry condition. In dry MAM, the formation of a SiO_2 layer in the flank side and the preservation of the cutting edge are responsible for the tool life increase. The first mechanism reduces flank wear height and the second one reduces the rake damage and flank wear depth. This is due to the location on the tool where each mechanism occurs. When lubricant is applied during MAM, the SiO_2 layer cannot be formed, and the wear reduction is only due to the enhanced lubrication and edge preservation. Lubrication increases the flank wear height and adhesion area. Therefore, the formation of SiO_2 deposition is more effective for flank wear reduction than the application of lubricant.

Finally in Chapter 4, the effect of the modulation frequency ratio on the tool wear was studied in order to find the optimal speed for which the improvement of MAM is most significant. changing the ratio does not alter flank wear but can significantly alter the crater wear in a consistent but gradual manner. In general, crater wear is reduced as the ratio increases. However, when the ratio is excessively high, the tool nose wear is higher due to increased tool rubbing the workpiece at a higher frequency. On the other hand, even at an extremely low frequency ratio, the SiO_2 layer formed on the flank side in MAM from the beginning of the tests, and the SiO_2 layer shape is independent of the frequency ratio. Also, there is slightly more crater wear as the ratio decreases, which indicates that the beneficial flank wear reduction for MAM compared to CM can occur over a wide range of frequencies and does not influence the crater wear behavior. The tool temperature in MAM is always lower or similar to (but only at the end of the test) that of CM. For MAM, the tool temperature decreases with increased modulation ratio as more disruptions translate into a lower temperature. However, the increase in nose rubbing at higher frequencies generates more heat acting against the cooling effect of MAM and increasing temperature again. Therefore, an optimal ratio can be determined to be between the highest and lowest frequencies tested. In conclusion, an optimal MAM frequency ratio can be found when machining CGI with coated carbides, for which there is a better balance of nose and crater wear and therefore a more effective tool temperature reduction, and a more uniform wearing process.

In summary, this dissertation fills a gap in the knowledge of the machining science discovering that tool life of coated carbides when machining CGI can be improved with Modulation-Assisted Machining. The root cause of the improvement is described as two wear mechanisms that are drastically distinct from those found in conventional machining. Finally, it is proven that the tool life can be maximized in MAM when the frequency ratio is adjusted to account for the different wear modes that are dominant in the machining process. MAM can be therefore applied successfully as a novel technique to improve the machinability of CGI in continuous cutting processes, which should promote a wider adoption of CGI in the manufacturing of industrial products such as diesel engine blocks.

FUTURE WORK

This work focused on MAM turning of CGI with coated carbides, however an interesting topic of research would be development of tool materials optimized for CGI machining, such as CBNs with chemical compositions capable of forming protective alumina layers on the rake side as reported in [18]. MAM could increase the potential to form protective layers in these special types of tools therefore increasing tool life even more than in previous studies [73]. Another important remaining question is why the cutting and feed forces behave so distinctly when the MAM frequency ratio is changed. This question could be tackled with a Finite element model of the MAM cycles considering the variation in the effective chip thickness during the engagement and disengagement intervals. Additionally, the limit vibration amplitude required for wear improvement could be studied. For these experiments, a finite element model could help to understand why the forces in MAM behave in such a unique way. Finally, another interesting direction is the application of MAM in turning of other difficult to cut materials such as Ti64AlV as reported in [76]. In previous studies with uncoated carbides in Ti64, it has been found that MAM can reduce crater wear but without a significant reduction in flank wear. Given the evidence presented in this dissertation, perhaps the formation of protective layers would be possible by implementing different coating materials more suitable for MAM turning of Ti64 [99–101]. Also, the force and temperature could be analyzed and analytical models for the kinematics and heat transfer during MAM could be used to better understand how the tool life does not improve for some machining operations such as turning Ti64 with uncoated carbides in the way that coated carbides life is improved when machining CGI [102,103]. This way, the root cause of the problem could be addressed and a MAM condition which improves the tool life could be determined for different types of difficult to cut materials.

BIBLIOGRAPHY

[1] Black JT, Kohser RA. DeGarmo's materials and processes in manufacturing. John Wiley & Sons; 2017.

[2] Klocke F. Manufacturing Processes 1: Cutting. 2011.

[3] Dawson S. Compacted graphite iron: mechanical and physical properties for engine design. Vdi Berichte 1999;1472:85–106.

[4] Abele E, Sahm A, Schulz H. Wear mechanism when machining compacted graphite iron. CIRP Ann 2002;51:53–6.

[5] Mocellin F, Melleras E, Guesser WL, Boehs L. Study of the machinability of compacted graphite iron for drilling process. J Brazilian Soc Mech Sci Eng 2004;26:22–7.

[6] Dawson S. Compacted graphite iron-a material solution for modern engine design. SAE 2011 World Congr Exhib 2011:4271. https://doi.org/10.4271/2011-01-1083.

[7] Guesser WL, Duran PV, Krause W. Compacted Graphite Iron for Diesel Engine Cylinder Blocks. Congrès Le Diesel Aujourd'hui Demain 2004:1–11.

[8] Dawson S, Hollinger I, Robbins M, Daeth J, Reuter U, Schulz H. The effect of metallurgical variables on the machinability of compacted graphite iron. SAE Tech Pap 2001:4271. https://doi.org/10.4271/2001-01-0409.

[9] Dawson S, Hollinger I, Robbins M, Daeth J, Reuter U, Schulz H. The effect of metallurgical variables on the machinability of compacted graphite iron. SAE Trans 2001:334–52.

[10] Bömcke A. Ein Beitrag zur Ermittlung der Verschleißmechanismen beim Zerspanen mit hochharten polykristallinen Schneidstoffen 1989.

[11] Neises A. Einfluß von Aufbau und Eigenschaften hochharter nichtmetallischer Schneidstoffe auf Leistung und Verschleiß im Zerspanprozeß mit geometrisch definierter Schneide. VDI Verlag; 1995.

[12] Erinski D. Untersuchungen über den Einfluss des Werkstoffgefüges auf das Zerspanverhalten von al-Si-Gusslegierungen 1990.

[13] Kramer BM, Suh NP. Tool wear by solution: a quantitative understanding 1980.

[14] Stephenson DA, Agapiou JS. Metal cutting theory and practice. CRC press; 2018.

[15] Nguyen TK. Fundamental tool wear study in turning of Ti-6Al-4V alloy (Ti64) and nano-enhanced minimum quantity lubrication (MQL) milling. Michigan State University; 2015.

[16] Gastel M, Konetschny C, Reuter U, Fasel C, Schulz H, Riedel R, et al. Investigation of the wear mechanism of cubic boron nitride tools used for the machining of compacted graphite iron and grey cast iron. Int J Refract Met Hard Mater 2000;18:287–96.

[17] Pereira AA, Boehs L, Guesser WL. The influence of sulfur on the machinability of gray cast iron FC25. J Mater Process Technol 2006;179:165–71.

[18] Nguyen D, Tooptong S, Park KH, Kwon P. Formation mechanism of alumina layer in protecting cubic boron nitride inserts in turning cast irons. Int J Mach Tools Manuf 2020;153:103539. https://doi.org/10.1016/j.ijmachtools.2020.103539.

[19] Cahoon HP, CHRISTENSEN CJ. Sintering and Grain Growth of Alpha-Alumina. J Am Ceram Soc 1956;39:337–44.

[20] Gutnichenko O, Bushlya V, Zhou J, Ståhl JE. Tool wear and machining dynamics when turning high chromium white cast iron with pcBN tools. Wear 2017;390–391:253–69. https://doi.org/10.1016/j.wear.2017.08.005.

[21] Salmang H, Scholze H, Schulze D. Keramik teil 1: Allgemeine grundlagen und wichtige eigenschaften 1982.

[22] Hornbogen E. Werkstoffe: Aufbau und Eigenschaften von Keramik-, Metall-, Polymer-und Verbundwerkstoffen. Springer; 2006.

[23] Tooptong S, Park KH, Kwon P. A comparative investigation on flank wear when turning three cast irons. Tribol Int 2018;120:127–39. https://doi.org/10.1016/j.triboint.2017.12.025.

[24] Nayyar V, Grenmyr G, Kaminski J, Nyborg L. Machinability of compacted graphite iron (CGI) and flake graphite iron (FGI) with coated carbide. Int J Mach Mach Mater 2013;13:67–90.

[25] Berglund A, Nicolescu CM, Svensson H. The effect of interlamellar distance in pearlite on CGI machining 2009.

[26] Tasdelen B, Escursell M, Grenmyr G, Nyborg L. Machining of gray cast irons and compacted graphite iron. Swedish Prod. Symp., 2007, p. 1–6.

[27] Röhrig K. Gusseisen mit Vermiculargraphit–Herstellung, Eigenschaften, Anwendung. K+ G 1991;1.

[28] Sousa TA, De Paula MA, Konatu RT, Ribeiro M V., De Campos E, Souza JVC. Investigation of the performance of ceramic tools of alumina doped with magnesium oxide in the dry machining of compacted graphite iron. Mater Res Express 2019;6. https://doi.org/10.1088/2053-1591/aafd74.

[29] Masuda M, Sato T, Kori T, Chujo Y. Cutting performance and wear mechanism of alumina-based ceramic tools when machining austempered ductile iron. Wear 1994;174:147–53.

[30] Gabaldo S, Diniz AE, Andrade CLF, Guesser WL. Performance of carbide and ceramic tools in the milling of compact graphite iron-CGI. J Brazilian Soc Mech Sci Eng 2010;32:511–7.

[31] Diniz AE. Coppini NL E Marcondes FC Tecnologia da usinagem dos materiais. 6º edição Editora MM. São Paulo, 262f 2008.

[32] Da Silva MB, Naves VTG, De Melo JDB, De Andrade CLF, Guesser WL. Analysis of wear of cemented carbide cutting tools during milling operation of gray iron and compacted graphite iron. Wear 2011;271:2426–32. https://doi.org/10.1016/j.wear.2010.11.030.

[33] Sayit E, Aslantas K, Çiçek A. Tool wear mechanism in interrupted cutting conditions. Mater Manuf Process 2009;24:476–83. https://doi.org/10.1080/10426910802714423.

[34] Cakir MC, Bayram A, Isik Y, Salar B. The effects of austempering temperature and time onto the machinability of austempered ductile iron. Mater Sci Eng A 2005;407:147–53.

[35] Ezugwu EO, Wang ZM. Titanium alloys and their machinability - A review. J Mater Process Technol 1997;68:262–74. https://doi.org/10.1016/S0924-0136(96)00030-1.

[36] Zelinski P. Surpassing the speed limit in CGI. Mod Mach Shop 2003;76:102–3.

[37] Li K-M, Liang SY. Modeling of cutting temperature in near dry machining 2006.

[38] Stephenson DA, Ali A. Tool temperatures in interrupted metal cutting. J Manuf Sci Eng Trans ASME 1992;114:127–36. https://doi.org/10.1115/1.2899765.

[39] Karaguzel U, Budak E. Investigating effects of milling conditions on cutting temperatures through analytical and experimental methods. J Mater Process Technol 2018;262:532–40.

[40] Shaw MC, Cook NH, Finnie I. The Shear-Angle Relationship in Metal Cutting. Trans ASME 1953;75:273–88.

[41] Bagherzadeh A, Budak E. Investigation of machinability in turning of difficult-to-cut materials using a new cryogenic cooling approach. Tribol Int 2018;119:510–20.

[42] Tai BL, Stephenson DA, Furness RJ, Shih AJ. Minimum quantity lubrication (MQL) in automotive powertrain machining. Procedia CIRP 2014;14:523–8. https://doi.org/10.1016/j.procir.2014.03.044.

[43] Shin YC. Laser assisted machining: its potential and future. Int. Congr. Appl. Lasers Electro-Optics, vol. 2010, Laser Institute of America; 2010, p. 513–22.

[44] Nguyen Di, Lee PH, Guo Y, Park KH, Kwon P. Wear Performance Evaluation of Minimum Quantity Lubrication with Exfoliated Graphite Nanoplatelets in Turning Titanium Alloy. J Manuf Sci Eng Trans ASME 2019. https://doi.org/10.1115/1.4043899.

[45] Varghese KP, Balaji AK. Effects of tool material, tool topography and minimal quantity lubrication (MQL) on machining performance of compacted graphite iron (CGI). Int J Cast Met Res 2007;20:347–58. https://doi.org/10.1179/136404608X320698.

[46] Kuzu AT, Bijanzad A, Bakkal M. Experimental Investigations of Machinability in the Turning of Compacted Graphite Iron using Minimum Quantity Lubrication. Mach Sci Technol 2015;19:559–76. https://doi.org/10.1080/10910344.2015.1085313.

[47] Supekar SD, Clarens AF, Stephenson DA, Skerlos SJ. Performance of supercritical carbon dioxide sprays as coolants and lubricants in representative metalworking operations. J Mater Process Technol 2012;212:2652–8. https://doi.org/https://doi.org/10.1016/j.jmatprotec.2012.07.020.

[48] Clarens AF, Hayes KF, Skerlos SJ. Feasibility of metalworking fluids delivered in supercritical carbon dioxide. J Manuf Process 2006;8:47–53.

[49] Stephenson DA, Skerlos SJ, King AS, Supekar SD. Rough turning Inconel 750 with supercritical CO2-based minimum quantity lubrication. J Mater Process Technol 2014;214:673–80.

[50] Skvarenina S, Shin YC. Laser-assisted machining of compacted graphite iron. Int J Mach Tools Manuf 2006;46:7–17. https://doi.org/10.1016/j.ijmachtools.2005.04.013.

[51] Zhao F, Bernstein WZ, Naik G, Cheng GJ. Environmental assessment of laser assisted manufacturing: case studies on laser shock peening and laser assisted turning. J Clean Prod 2010;18:1311–9.

[52] Guo Y, Stalbaum T, Mann J, Yeung H, Chandrasekar S. Modulation-assisted high speed machining of compacted graphite iron (CGI). J Manuf Process 2013;15. https://doi.org/10.1016/j.jmapro.2013.06.001.

[53] Stephenson DA, Agapiou JS. Metal cutting theory and practice. CRC press; 2016.

[54] Kumabe J. Vibration cutting—basic principle and application. Japan: Jikkyo Shuppan Books 1979.

[55] Moscoso W, Olgun E, Compton WD, Chandrasekar S. Effect of Low-Frequency Modulation on Lubrication of Chip-Tool Interface in Machining. J Tribol 2005;127:238–44. https://doi.org/10.1115/1.1829720.

[56] Chhabra PN, Ackroyd B, Compton WD, Chandrasekar S. Low-frequency modulation-assisted drilling using linear drives. Proc Inst Mech Eng Part B J Eng Manuf 2002;216:321–30.

[57] Brehl DE and, Dow TA. Review of vibration-assisted machining. Precis Eng 2008;32:153–72.

[58] Neugebauer R, Stoll A. Ultrasonic application in drilling. J Mater Process Technol 2004;149:633–9.

[59] Paktinat H, Amini S. Experiments and finite element simulation of ultrasonic assisted drilling. J Manuf Sci Eng 2018;140.

[60] Zhang X, Liu K, Kumar AS, Rahman M. A study of the diamond tool wear suppression mechanism in vibration-assisted machining of steel. J Mater Process Technol 2014;214:496–506.

[61] Zhang X, Kumar AS, Rahman M, Nath C, Liu K. Experimental study on ultrasonic elliptical vibration cutting of hardened steel using PCD tools. J Mater Process Technol 2011;211:1701–9.

[62] Mann JB, Saldana C, Moscoso W, Compton WD, Chandrasekar S. Effects of controlled modulation on interface tribology and deformation in machining. Tribol Lett 2009;35:221–7.

[63] Guo Y, Mann JB. Control of chip formation and improved chip ejection in drilling with modulation-assisted machining. J Manuf Sci Eng Trans ASME 2020;142:1–7. https://doi.org/10.1115/1.4046829.

[64] Yeung H, Guo Y, Mann JB, Compton WD, Chandrasekar S. Effect of low-frequency modulation on deformation and material flow in cutting of metals. J Tribol 2016;138:1–9. https://doi.org/10.1115/1.4031140.

[65] Sharif S, Rahim EA. Performance of coated-and uncoated-carbide tools when drilling titanium alloy—Ti–6Al4V. J Mater Process Technol 2007;185:72–6.

[66] Zhang PF, Churi NJ, Pei ZJ, Treadwell C. Mechanical drilling processes for titanium alloys: a literature review. Mach Sci Technol 2008;12:417–44.

[67] Guo Y, Lee SE, Mann JB. Piezo-Actuated modulation-Assisted drilling system with integrated force Sensing. J Manuf Sci Eng Trans ASME 2017;139:1–7. https://doi.org/10.1115/1.4033929.

[68] Toews HG, Compton WD, Chandrasekar S. A Study of the Influence of Superimposed Low-Frequency Modulation on the Drilling Process. Precis Eng 1998;22:1–9. https://doi.org/https://doi.org/10.1016/S0141-6359(97)00085-8.

[69] Deyuan Z, Lijiang W. Investigation of chip in vibration drilling. Int J Mach Tools Manuf 1998;38:165–76.

[70] Okamura K, Sasahara H, Segawa T, Tsutsumi M. Low-frequency vibration drilling of titanium alloy. JSME Int J Ser C Mech Syst Mach Elem Manuf 2006;49:76–82.

[71] Guo Y, Mann JB. Control of chip formation and improved chip ejection in drilling with modulation-assisted machining. J Manuf Sci Eng Trans ASME 2020;142. https://doi.org/10.1115/1.4046829.

[72] Mann JB, Saldana CJ, Guo Y, Yeung H, Compton WD, Chandrasekar S. Effects of controlled modulation on surface textures in deep-hole drilling. SAE Tech Pap 2012;6:24–32. https://doi.org/10.4271/2012-01-1868.

[73] Guo Y, Mann JB, Yeung H, Chandrasekar S. Enhancing tool life in high-speed machining of compacted graphite iron (CGI) using controlled modulation. Tribol Lett 2012;47:103–11.

[74] Yeung H, Sundaram NK, Mann JB, Dale Compton W, Chandrasekar S. Energy dissipation in modulation assisted machining. Int J Mach Tools Manuf 2013;74:41–9. https://doi.org/10.1016/j.ijmachtools.2013.07.007.

[75] Mann JB, Guo Y, Saldana C, Compton WD, Chandrasekar S. Enhancing material removal processes using modulation-assisted machining. Tribol Int 2011;44:1225–35. https://doi.org/10.1016/j.triboint.2011.05.023.

[76] Sandoval J, Nguyen D, Kwon P, Guo Y. An experimental study of modulation-assisted turning of TI6AL4V. ASME 2019 14th Int Manuf Sci Eng Conf MSEC 2019 2019;2:1–5. https://doi.org/10.1115/MSEC2019-3013.

[77] Sandoval J, Ali A, Kwon P, Guo Y. Modulation-assisted machining of compacted graphite iron with coated carbide tool in dry condition. Manuf Lett 2022;33:452–60.

[78] Wong TK, Kwon P. Dissolution profile of tool material into chip lattice 2006.

[79] Park K-H, Kwon PY. Flank wear of multi-layer coated tool. Wear 2011;270:771–80.

[80] Olortegui-Yume JA, Kwon PY. Crater wear evolution in multilayer coated carbides during machining using confocal microscopy. J Manuf Process 2007;9:47–60.

[81] Sandoval J, Ali A, Kwon P, Stephenson D, Guo Y. Wear reduction mechanisms in modulated turning of compacted graphite iron with coated carbide tool. Tribol Int 2022:108062.

[82] Barrow G. Review of experimental and theoretical techniques for assessing cutting temperatures. CIRP, l 973, 22,(2), 203-2 Ll 1974.

[83] Agapiou JS, Stephenson DA. Analytical and experimental studies of drill temperatures 1994.

[84] Rall DL, Giedt WH. Heat transfer to, and temperature distribution in, a metal-cutting tool. Trans Am Soc Mech Eng 1956;78:1507–12.

[85] Hollander MB. Technical Report on a Thermocouple-technique Investigation of Temperature Distribution in the Workpiece During Metal Cutting. ASTE Research Fund; 1957.

[86] Shaw MC, Cook NH, Smith PA. Report on the Cooling Characteristics of Cutting Fluids. ASTME Res Rep No 19 1958.

[87] Reichenbach GS. Experimental measurement of metal-cutting temperature distributions. Trans Am Soc Mech Eng 1958;80:525–36.

[88] Lipman MP, Nevis BE, Kane GE. A remote sensor method for determining average tool-chip interface temperatures in metal cutting 1967.

[89] Wang KK, Wu S-M, Iwata K. Temperature responses and experimental errors for multitooth milling cutters 1968.

[90] Groover MP, Kane GE. A continuing study in the determination of temperatures in metal cutting using remote thermocouples 1971.

[91] Yen DW, Wright PK. A remote temperature sensing technique for estimating the cutting interface temperature distribution 1986.

[92] Chow JG, Wright PK. On-line estimation of tool/chip interface temperatures for a turning operation 1988.

[93] Beck J V, Blackwell B, Clair Jr CRS. Inverse heat conduction: Ill-posed problems. James Beck; 1985.

[94] Stephenson DA. An inverse method for investigating deformation zone temperatures in metal cutting 1991.

[95] Palmai Z. Cutting temperature in intermittent cutting. Period Polytech Mech Eng 1987;31:61–78.

[96] Salomon C. Verfahren zur bearbeitung von metallen oder bei einer bearbeitung durch schneidende werkzeuge sich ahnlich verhaltenden werkstoffen. Dtsch Pat 1931:931.

[97] King R. Handbook of high-speed machining technology. Springer Science & Business Media; 2013.

[98] Lezanski P, Shaw MC. Tool face temperatures in high speed milling 1990.

[99] Khawarizmi RM, Guo Y, Bieler TR, Kwon P. A Machinability Study of Coated Inserts for Turning Ti-6Al-4V. Int. Manuf. Sci. Eng. Conf., vol. 85819, American Society of Mechanical Engineers; 2022, p. V002T05A053.

[100] Khawarizmi RM. Tool Wear Study in Turning Ti-6Al-4V and Edge Trimming of Carbon Fiber Reinforced Plastics (CFRP) 2022.

[101] Park K-H, Kwon P, Kim D. Wear characteristic on BAM coated carbide tool in drilling of composite/titanium stack. Int J Precis Eng Manuf 2012;13:1073–6.

[102] Eren B, Sencer B. Mechanistic Cutting Force Model and Specific Cutting Energy Prediction for Modulation Assisted Machining. Procedia Manuf 2020;48:474–84. https://doi.org/10.1016/j.promfg.2020.05.071.

[103] Gao Y, Sun R, Leopold J. An analytical force model for modulation-assisted turning. J Manuf Process 2018;31:712–30. https://doi.org/10.1016/j.jmapro.2017.12.024.